Frequency and Voltage Control of Islanded Microgrids

by

Mehdi Parvizimosaed

A thesis
presented to the University of Waterloo
in fulfillment of the
thesis requirement for the degree of
Doctor of Philosophy
in
Electrical and Computer Engineering

Waterloo, Ontario, Canada, 2020

Examining Committee Membership

The following served on the Examining Committee for this thesis. The decision of the Examining Committee is by majority vote.

External Examiner: Vincent Wong
Professor, Dept. of Electrical and Computer Engineering,
University of British Columbia

Supervisor(s): Weihua Zhuang
Professor, Dept. of Electrical and Computer Engineering,
University of Waterloo

Internal Member: Claudio Canizares
Professor, Dept. of Electrical and Computer Engineering,
University of Waterloo

Internal Member: Kankar Bhattacharya
Professor, Dept. of Electrical and Computer Engineering,
University of Waterloo

Internal-External Member: Liqun Diao
Assistant Professor, Dept. of Statistics and Actuarial Science,
University of Waterloo

Author's Declaration

Abstract

Islanded microgrids (MGs), characterized by distributed generators, power consumers, and energy storage systems (ESSs), are designed to significantly enhance self-sustainability of future distribution networks and to provide energy for remote communities. In order to have a stable system, both primary and secondary frequency and voltage control of the MG are critical.

From a primary control perspective, it is essential to maintain frequency and voltage in acceptable ranges. Conventional controllers are designed to regulate system frequency and voltage solely based on droop control theory, and this is mainly provided by fast-response generation units such as ESSs. Therefore, an intelligent power sharing (IPS) control is necessary to maintain frequency and voltage within acceptable ranges, and to share power not only based on generation units' droop values, but also their operating power capabilities. A mathematical model of small-perturbation stability is presented along with performance analysis. Based on analysis and simulation results, the IPS controller offers advantages such as robust performance under load and renewable energy variations, a dynamic compromise between voltage regulation and accurate reactive power sharing among generators, and enhancement of voltage regulation by an adaptive virtual impedance.

From a secondary control perspective, scheduling of generation units based on conventional unit commitment (UC) remains fixed for the duration between two dispatch intervals; however, demand or renewable generation can continuously change. This stair-pattern scheduling of generation units creates large frequency and voltage excursions at the edge of each dispatch interval. Different from the existing UC mechanisms, a hybrid mid-level controller is proposed based on communications with a distributed primary controller. It determines optimal power of generation units between two dispatch intervals for the secondary controller while regulating frequency and voltage within desirable ranges. Through several tested scenarios on a CIGRE test system, numerical results show that the mid-level controller can regulate frequency and voltage of the islanded MG. It covers time intervals between those of primary and secondary controllers and avoids the stair-pattern generation scheduling in conventional UCs. Additionally, it reduces both operating cost of MG and degradation of fast-acting generation units' life-cycle.

Subsequently, impact of communication delay on islanded MGs is studied. The delay causes local controllers to use outdated power dispatches at the proposed mid-level controller. The outdated reference power deviates frequency and voltage from their nominal values in primary control. Existing primary and secondary controllers use a communication network assuming no time delay or considering a constant time delay. A mathematical model of constant and time-varying delay in islanded MGs is integrated into the proposed mid-level controller. This formulation addresses the impact of time delay on transient performance of these controllers. A delay-based controller is designed to mitigate frequency oscillation of islanded MGs in the presence of either small or large perturbations. Numerical results are performed on small and large perturbations to evaluate the impact of time delay on realistic 14-bus CIGRE test system.

Acknowledgments

I would like to express my deep appreciation to Prof. Weihua Zhuang for her exemplary supervision, great support throughout my Ph.D. studies. Despite the boundaries of communication, power and energy, I have learnt the professionalism and teaching throughout my life. Special thanks go to Prof. Xuemin Shen and the Broadband Communication Research (BBCR) group for their great collaborations over these years.

I would like to express my sincere gratitude to my committee members for their valuable comments on my work: Prof. Claudio Canizares and Prof. Kankar Bhattacharya from the Department of Electrical and Computer Engineering; Prof. Liqun Diao from the Department of Mathematics, University of Waterloo; Prof. Vincent Wong from the Department of Electrical and Computer Engineering, University of British Columbia.

I will be always indebted to Ms. Mary McPherson of the writing center who spent her, often personal, time helping me out. There is a lot I should learn from her.

I have consistently been on the receiving end of my dear friends' attention, especially during my Ph.D. studies. I am truly grateful to Farid, Zohreh, Ali Akbar, Omar, Hesham, Jobanmeet, and Ahmed.

The most deserved acknowledgments go to my parents, Fatoallah and Khadijeh, and my beloved sister, Zahra, and brother-in-law, Mostafa, and my brothers. It is because of your wholehearted support that I finished this thesis.

Dedication

Dedicated to my beloved parents, Fatoallah Parvizimosaed and Khadijeh Rezaie.

Table of Contents

List of Tables

List of Figures

Nomenclature

Chapter 3

D	Damping coefficient (p.u.)
G_f, G_v	Transfer functions for frequency and voltage control of SG
H	Inertia constant (s)
i	generation unit assets
$i_{o,dq}$	Inverter output current in $dq-$axis (A)
i_{Lf}	Current flowing in LCL filter (A)
I_x	Constant current coefficient
J	Inertia moment of SG
K_{pv}, K_{iv}	Inverter proportional and integral gains of voltage controller
K_{pi}, K_{ii}	Inverter proportional and integral gains of current controller
K_t, T_t	Turbine gain and time constant of SG (s)
K_g, T_g	Governor gain and time constant of SG (s)
K_s, T_s	Sensor gain and time constant of SG (s)
K_e, T_e	Exciter gain and time constant of SG (s)
K_A, T_A	Amplifier gain and time constant of SG (s)
Ld	Load superscript
L_f, C_f	Inverter output inductance and capacitor(H, F)
m_p	Frequency droop gain $((rad/s)/kW)$
n_G	Number of generation units
n_{Ld}	Number of loads
n_p	Voltage droop gain $(V/kVAr)$
P_0, Q_0	Reference active and reactive of the system $(kW, KVAr)$
p, q	Inverter instantaneous active and reactive power $(kW, KVAr)$
P_i	Output active power of generation unit i (kW)
P_x	Constant power coefficient
Q_i	Output reactive power of generation unit i $(kVAr)$
R^*	Inverter resistance with virtual impedance (Ω)
s	Laplace variable
$v_{o,dq}$	Output voltage in $dq-$axis (V)
v_{Lf}	Voltage drop in LCL filter (V)
V_n	Rated voltage of MG (V)

V_0	Reference voltage of MG (V)
V^*_{dq0}	Reference voltage of current controller (V)
X^*	Inverter reactance with virtual impedance (Ω)
Z_v	Inverter virtual impedance (Ω)
Z_x	Constant impedance coefficient
ω_0	Reference frequency of MG (rad/s)
ω_n	Rated frequency of MG (rad/s)
ω_c	Cut-off frequency of LCL filter (rad/s)
ΔP_G	Change in generation power of DG (kW)
ΔP_L	Change in net demand power of MG(kW)
ΔP_m	Change in driving mechanical power of SG (kW)
ΔP_e	Change in electrical power of SG (kW)
$\Delta\omega$	Frequency change (rad/s)
Λ_G	Set of generation units

Chapter 4

b	Bus asset
c	Current controller
f_{zv}	Virtual impedance sensitivity function
$i_{l,dq}$	Current flowing the coupling inductance in $dq-$axis (A)
INV	Inverter unit
j, g	ESS and generation unit assets
$K^f_{i,tr}$	Frequency-transient IPS coefficient of generation unit i
$K^v_{i,tr}$	Voltage-transient IPS coefficient of generation unit i
K_i	Frequency IPS gain of generation unit i
l	Line signal
lcl	LCL filter
Ln	Line superscript
n_{Ln}	Number of lines
n_{pi}	Voltage droop value of DG i ($V/kVAr$)
m_{pi}	Frequency droop value of DG i (Hz/kW)
M_G	Adjacency matrix of generation units to nodes
M_{Ld}	Adjacency matrix of loads to nodes
M_{Ln}	Adjacency matrix of MG network to nodes
o	Output signal superscript
p	Power controller
$\overline{P_i}/\underline{P_i}$	Maximum/minimum output active power of DG i (kW)

$\overline{Q_i}/\underline{Q_i}$	Maximum/minimum output reactive power of DG i ($kVAr$)
r_v	Resistance of virtual impedance (Ω)
R_N	Virtual resistor matrix in stability analysis (Ω)
SG	SG index
S_λ	Stability sensitivity index
S_m	Stability margin index
S_v	Slack variable of voltage integration (V)
t_{set}	Settling time (s)
u_x, u_y	Input vector of state-space model
v	Voltage controller
W_f	Weighted adjacency matrix of frequency control
W_v	Weighted adjacency matrix of voltage control
x	State variable
X_v	Inverter virtual reactance (H)
y_{ij}	Admittance of line between node i and j (Ω)
z_{ij}	Impedance of line between node i and j (Ω)
β_i	V-Q compromise IPS gain of generation unit i
κ_i	Voltage IPS gain generation unit i
ω_{ss}	Steady-state frequency of the system (rad/s)
ω_{com}	Common frame frequency of inverter (rad/s)
$\Delta R_v^{max,min}$	Maximum/minimum change in virtual resistance (Ω)
$\Delta X_v^{max,min}$	Maximum/minimum change in virtual reactance (Ω)
$\tau_{1,2}$	Time constants of VFCSG (s)
$\mathcal{G}$	Set of generation unit
$\mathcal{N}$	Set of bus
ϕ_{ij}	Phase of impedance z_{ij} (rad)
θ_i	Phase voltage of bus connected to generation unit i (rad)
υ, γ	Inverter state variable of current/voltage controller
Ψ_j	Stability margin of controller j

Chapter 5

a_i/b_i	Economic coefficients for i^{th} SG ($\$/kW^2s, \$/kWs$)
$a^m(t)$	Action variable at t^{th} sub-interval of time m
C_i^s/C_i^d	Start-up/shut-down costs for i^{th} SG (\$)
C_j	ESS capacity (kWs)
$e_{AN}(t)$	Error in action network
$e_{CN}(t)$	Error in critic network

$e_{MN}(t)$	Error in model network
m	Secondary control index
n_T	Number of mid-level control sub-intervals
n_M	Number of secondary control time slot
$P_L^m(t)$	Demand at $t^t h$ mid-level sub-interval of time m
$R_i^u/R^d/i$	Ramp-up/down power of i^{th} SG (kW/s)
$s^m(t)$	State variable at t^{th} sub-interval of time m
$\hat{s}^m(t)$	Estimated state variable at t^{th} sub-interval of time m
$S_j^m(t)$	State of charge of j^{th} battery at t^{th} sub-interval of time m
t	mid-level control index
$u_i^m(t)$	Binary variable to determine on/off of i^{th} generation unit
$u_{c,j}^m(t)/u_{d,j}^m(t)$	Binary variable for charging and discharging of j^{th} ESS
$y_i^m(t)/z_i^m(t)$	Start-up/shut-down binary variables for i^{th} SG
$\mathcal{J}_u$	Operational cost-to-go function
$\mathcal{J}_s$	Stability margin cost-to-go function
$\Delta\mathcal{V}^m$	Voltage utility function (V)
$\Delta\mathcal{F}^m$	Frequency utility function (rad/s)
$\Delta\mathcal{C}^m$	Cost utility function (\$)
$\Delta\mathcal{E}^m$	Energy utility function (kW)
γ	Learning factor in dynamic programming
$\eta_{c,j}, \eta_{d,j}$	Efficiency of charging and discharging of j^{th} battery
$\lambda^m(t)$	Derivation of cost-to-go function respect to state variable

Chapter 6

$A_0^{(MG)}$	Non-sensitive characteristics matrix of MG to delay
$A_d^{(MG)}$	Delay-based characteristics matrix of MG
A	Frequency deviation matrix in Lyapunov-Krasvoskii model
$d(t)$	Load change as an input of IO approach
H	Non-singular matrix to keep the stability of SSG
$g_{u,z}(.)$	Transform operators from one coordination to another one
$V(t)$	Energy function of Lyapunov-Krasvoskii
$W_{1,2}$	Controller coefficient matrix in Lyapunov-Krasvoskii model
$\Delta_\tau(s)$	Laplacian form of delay function
τ^m	Communication delay in mid-level controller (s)
$\underline{\tau}^m, \overline{\tau}^m$	Lower and upper bound of delay in mid-level controller (s)
$\tau_{\lambda_m}^m$	Time delay margin (s)

List of Acronyms

AC	alternative current
ACD	adaptive critic design
ADHDP	adaptive dual heuristic dynamic programming
AVR	automatic voltage regulator
CDF	cost-driven function
DC	direct current
DHP	dual heuristic programming
DG	distributed generation
DTDC	distributed transient droop controller
DVFC	dynamic voltage and frequency controller
EDF	energy-driven function
EMS	energy management
ESS	energy storage system
IO	input-output
IPS	intelligent power sharing
LC	local controller
LMI	linear matrix inequality
LPF	low pass filter

LTI linear time-invariant

MG microgrid

MGCC main grid central controller

MNR modified Newton-Raphson

NN neural network

PCC point of common coupling

PI proportional and integral

PF participation factor

PSS power system stabilizer

SG synchronous generator

SI stability index

SOC state of charge

SSG scaled small gain

SP shifting process

UC unit commitment

VFCSG voltage based frequency controller of synchronous generator

WT wind turbine

Chapter 1

Introduction

1.1 Microgrids

Due to an urgent need to develop more efficient, reliable, and cleaner power grids, energy sectors are currently moving towards the introduction of smart grids. A microgrid (MG) is a low-voltage distribution network which consists of a variety of distributed generation (DG) units, energy storage systems (ESSs), and controllable/uncontrollable loads. The concept of MGs has received considerable attention owing to their potential to operate independently and to isolate themselves from the main grid in the case of a disturbance. Depending on the situation, a typical MG can operate in two modes:

1. Interconnected mode where MG is linked to the main grid through distribution substation and power point coupling (PCC).
2. Islanded (autonomous) mode where it is isolated from the main grid [1].

Following the standards of Consortium for Electric Reliability Technology Solutions (CERTS) [2], energy operators in interconnected MGs are in charge of managing system operations through power dispatching and voltage setting to each local controller (LC) to perform following responsibilities:

- balancing supply and demand;
- achieving acceptable power quality;
- regulating voltage and frequency;

- communicating among MG components.

Any deviation of active power at a specific area of MG is reflected by a change in frequency, which is a common factor throughout MG. The same convention is applied to reactive power sharing among units and voltage changes. In summary, frequency and voltage regulation is achieved by active and reactive power sharing among units, respectively. While an MG operates in a grid-connected mode, its power shortfall or excess is exchanged by upstream grid. Therefore, MG is controlled similarly to conventional power systems. For islanded mode, MG control means balancing supply and demand power to maintain the frequency and voltage within acceptable ranges. According to IEEE 1547 [3], the guideline for interconnection of generation units [2], disconnection of MG from upstream grid can be occurred either a) intentionally (such as for scheduled maintenance or degradation of power quality) or b) unintentionally (such as in disturbances or unscheduled events) [4]. Note that the frequency and voltage control in an islanded MG is more severe than in grid-connected operation mode, especially whenever more than one energy source is operated to supply certain electrical loads. In addition, increment of intermittent renewable generation and uncertainty levels can cause more and more short-term unpredictable power variations. Care should be taken that electricity demand may be partly unpredictable, which adds another dimension of complexity to control of islanded MGs. The focus of this thesis is on frequency and voltage control in islanded MGs.

1.1.1 Distributed Primary Frequency and Voltage Control

Primary control, known as internal control, is the first frequency and voltage level, and features by droop characteristics. This control level responds to MG dynamics and tracks reference frequency and voltage values [5]. In an islanded MG, any difference between active and reactive power supplied by generation units and loads causes a fast deviation of frequency (e.g., 1 Hz/s [6]) and voltage. This occurs because MG inertia in islanded mode is considerably lower compared to that of grid-connected MGs. In fact, conventional frequency and voltage mechanisms are not fast enough to control sudden variations of renewable energy resources and loads [7]. In conventional methods, the controller is designed to regulate system frequency and voltage only based on droop control theory. Consequently, system frequency and voltage regulation are mostly provided by fast-response generation units such as ESSs. Therefore, an intelligent power sharing control is essential to maintain frequency and voltage within acceptable ranges, and to share power as well as their droop values. Furthermore, accurate reactive power sharing causes deviations over voltage due to unequal voltage drop in impedance connected to AC link. It is necessary to make a trade-off between voltage regulation and accurate power sharing among units.

1.1.2 Hybrid Secondary Frequency and Voltage Control

Secondary control, known as central control or energy management system, ensures mitigating steady-state frequency and voltage deviations by determining set points for the primary controller. Note that it operates in a slower time frame than that of the primary control [8]. This secondary control is centrally controlled by a main grid central controller (MGCC) installed at the top-level of hierarchical control system. The MGCC restores frequency and voltage to their nominal values by managing power sharing among generation units and controllable loads. In conventional mechanisms, the secondary controller uses a supplementary loop, known as automatic generation control, to mitigate the steady-state frequency deviation. Additionally, unit commitment (UC) is performed at the secondary control to ensure economic operation of MG. The scheduling of generation units in islanded MGs, based on conventional UC, remains fixed for the duration between two dispatch intervals; however, the demand or renewable generation can continuously change. Stair-pattern scheduling of generation units creates large frequency and voltage excursions at the edge of each dispatch interval. Furthermore, fixed scheduling is not efficient for either operation cost or MG and life-cycle of fast-acting generation units, without addressing output renewable power variability and demand perturbations [9, 10]. In theory, it is commonly assumed that local frequency, voltage, and net demand during each dispatch interval are equal to the corresponding steady-state conditions; thus, timescale separation happens between fast synchronization-enforcing primary and slower secondary controllers. In general, this timescale separation affects power-sharing properties and dynamical regulation of MG frequency and voltage in the secondary control, specifically during rapid load and renewable energy perturbations [11].

1.1.3 Frequency and Voltage Control with Communication Delay

Due to small-scale architecture of islanded MGs, control commands in primary and secondary control levels are rather sporadic and short, requiring the desired bandwidth but high reliability with minimum time latency. The primary control level is traditionally designed in a distributed architecture, where each LC uses available measurements of other

local controllers via a communication network. The secondary control is closely tied to the primary control, sending reference set points to each LC. Therefore, a communication network is necessary for basic operation of MG control. In conventional primary and secondary controls, communication delay is considered negligible between LC-to-LC and MGCC-to-LC [12, 13]. However, generation units contributing to frequency and voltage control receive the status of other units with a certain delay. This communication delay can cause instability in the control system, especially in small-size MGs [14].
In addition, the communication delay causes LCs to use outdated power dispatches at the secondary control level. Consequently, this outdated reference power deviates frequency and voltage from their nominal values in the primary control level.

1.2 Literature Review

The MG as described is a complicated system consisting of DGs, ESSs, and loads, and operates in 1) grid-connected and 2) islanded modes [8]. Concept of islanded MG has received attention owing to its advantages compared to conventional power systems. Islanded MGs allow remote communities to have access to pollution-free energy. They give impetus to the utilization of renewable energy sources such as PVs and wind turbines; hence, they reduce the adverse impacts of climate change. In the event of disturbances in the power grid, an islanded MG is the best alternative. Additionally, increasing need for clean energy and cheaper solar and wind energy resources leads to a growth in feed-in-tariffs and carbon-emission tax programs [6]. Due to economic problems and technical issues in electric power grids, macro-beneficiaries are driving energy sectors towards the application of islanded MGs [15].

1.2.1 Frequency and Voltage Control

Control of islanded MGs is complicated multi-objective management that deals with various time scales, technical constraints, and physical levels [16]. The main domains of MG management are composed of dynamic frequency and voltage control of MG and short-long term scheduling. To properly handle these issues, a standard solution for efficient MG management as a frequency and voltage control mechanism illustrated in Figure 1.1 has been widely accepted [17]. Functionally, an islanded MG can operate by using following control levels:

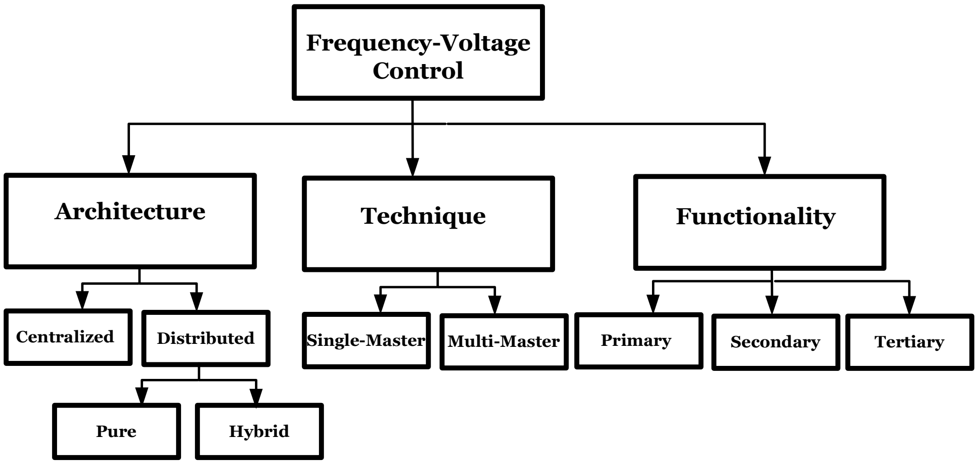

Figure 1.1: Classification of frequency and voltage control.

1. *Primary control*: This control level is responsible for stabilizing system frequency and voltage during intentional or unintentional events. It adjusts system frequency and voltage to their reference values by dispatching active and reactive power among DGs. Following a disturbance event, islanded MGs suffer from frequency and voltage alleviation due to power mismatch between supply and demand [4, 18]; hence, a frequency and voltage control is essential to be provided.
2. *Secondary control*: This controller is aimed to compensate for any frequency and voltage deviations from their reference values that are caused at the primary level. In addition, this control level adds intelligence to MG operation. It attempts to optimize the operating cost of MG with consideration of other merit interests such as life-cycle of ESSs [4, 19].
3. *Tertiary control*: It ensures optimal operation of MG in a time horizon of day or month. This long-term scheduling is accomplished by prediction of renewable energy sources and load variations for the next hours or days [16].

Bandwidths of control levels are in a slower time frame for the higher control level compared to primary one. The frequency and voltage control at the primary level has typically a response time within 1 ms$\sim$30 s, the secondary and tertiary control can be in time steps ranging from seconds to days [16].

From the energy manager perspective, MG controllers are classified into two types based on their applications; a) MGCC and b) LCs associated with generation and load units [1, 16].

- The MGCC installed at a low-voltage distribution network receives the information such as operating conditions of components, and manages MG operation by setting optimal dispatches for controllable generation and load units by sending command signals to LCs [1].
- The LCs at the primary control ensure controllable generation and load units to regulate the system frequency and voltage to reference values received from the MGCC [20].

Two control techniques are used to manage set point references, and how to restore the frequency and voltage of islanded MGs; a) single-master operation and b) multi-master operation.

- *Single-master operation*: In this control mode, a single generation unit aims to restore the system frequency as well as voltage of PCC. In this scheme, the master unit determines a frequency reference set point, and the rest of units operating as slave components. This control technique can be applied to small-scale MGs with only one generation unit, to deal with active and reactive power mismatch in presence of perturbations. The control system of single-master operation is simple to implement and needs no external communication link between units. However, due to dependency on a single generation unit, this operation scheme is not practical for large-scale MGs with high penetration of renewable energy resources or load variations [21].
- *Multi-master operation*: It allows multiple generation units to contribute to the frequency and voltage control. This control technique requires a reliable communication among generation and load units to ensure proper operation. Due to intercommunication requirements, components of MG control system should be physically close to each other. In addition, this technique does not account for the status of generation and load units at each operating point, thus affecting their contribution to frequency and voltage control [6].

From the architecture perspective, frequency and voltage controllers in an islanded MG can be classified into either centralized or distributed or both control schemes. Various parameters such as complexity, time delay in communication links, decision-making time, and expandability of the control system can be used to identify which architecture should be deployed. These parameters determine the level of distribution management, characterized by the allocation of some parts or the whole control process to the LCs.

- *Centralized control*: In a small MG with a few generation units, a central controller can make decisions using online calculations of the optimal operation and with databases continuously updated by information collected from different LCs [22].
- *Distributed control*: Moving towards distributed architecture, the control system uses advantages such as the controllers' expandability and less complexity in decision-making process, especially in an MG with many LCs. To have a more flexible operation and to avoid system failure due to a single main controller, a distributed architecture can be applied to the MG control. However, implementation of distributed control needs a more-complex communication infrastructure among LCs. Distributed control architecture is usually more suitable in the following MG cases:
    1. Large MGs where components are far away from each other, making data acquisition process difficult [23];
    2. Different types of components that have various design goals, making a unified decision more challenging [24];
    3. Flexible configurations, in which the control process can be changed by adding or removing units [16].

Table 1.1 summarizes advantages and limitations of both centralized and distributed architectures [16, 25, 26].

1.2.2 Primary Frequency and Voltage Control

The primary controller regulates the system frequency and voltage with dispatching active and reactive power among controllable generation and load units. This is because the manifestation of frequency and voltage control is similar to active and reactive power sharing in the primary control level. The power sharing approach in islanded MGs is more

Table 1.1: Comparison of centralized and distributed control architectures [16, 25, 26]

Architecture	Advantages	Disadvantages
Centralized model	• Multi-objective functions can be defined in the MGCC; • Implementation of architecture is relatively straight-forward; • Malfunctions can be easily detected; • Operating points gathered from LCs are easily available.	• Decision making requires a powerful central processor; • The decision-making process is slow; • Single-point system failure is possible; • Single controller complicates control system flexibility and expandability.
Distributed model	• Optimal operation set points for LCs can be rapidly computed; • It is not affected by single-point system failure; • It is flexible and expandable.	• Complex communication infrastructure is required within LCs; • Its numerous LCs make debugging difficult; • Poor LC coordination design leads to time delays.

challenging than that of grid-connected mode because of low inertia feature of MGs and capacity limitations of controllable units. Due to dynamics of renewable resources and load variations, an imbalance between supply and demand causes frequency and voltage deviations [27]. The power mismatch can be balanced by power sharing, which mainly affects a) MG stability margins, b) frequency and voltage restoration, c) operating power capability of controllable units [25], and d) optimal operation of MGs [28]. Existing power sharing approaches involve either a) droop power sharing control or b) isochronous power sharing control. In droop power sharing, DGs and ESSs mimic the behaviour of SGs in conventional power systems, and share the power mismatch in proportion to their droop values. Most recent studies have examined approaches such as conventional power and frequency (P-f) [29], transient control [30], load-angle [31], and resonance-based droop controllers [32]. All these methods are built on top of conventional droop control mechanisms. They damp oscillatory modes of power sharing controllers and reduce steady-state frequency and voltage errors. However, with increasing span of islanded MG operation, it is imperative to regulate frequency and voltage of MG not only stably, but also optimally [33]. These approaches result in MG instability when droop values of generation units are increased to share power mismatch among DGs and ESSs. In special cases, increasing operating power of generation units is not possible anymore when they reach their rated power. Hence, the choice of droop coefficients has a significant impact on frequency and voltage limit as well as power sharing accuracy [34]. In contrast to the limitations of droop control, isochronous power sharing methods provide zero steady-state frequency and voltage errors. They share active and reactive power among generation units according to their rated power. Although isochronous power sharing approaches address the challenge of MG instability, they suffer from slow power sharing control, causing improper frequency and voltage regulation [35]. To overcome these problems, dynamic droop controller adaptively changes droop gain to handle the increase in frequency deviation. Due to high penetration of SGs in islanded MGs, which have relatively large inertia constant, dynamic droop controllers can not maintain stability [36]. Some studies deal with these issues by introducing secondary loop and diffusive averaging variables that promote fast and smooth frequency regulation. Diffusive averaging algorithms integrate proportional and integral variables into conventional droop models. These algorithms utilize the distributed communication infrastructure in the primary control level to regulate frequency precisely [11]. However, they cannot share power uniformly among generation units despite of maintaining MG stability. In addition, a supplementary loop has been introduced to regulate the MG frequency by adding the virtual inertia to MGs. However, this method is restricted by the time response and rating power of generators and turbines [37]. Further challenges arise from compromise between voltage regulation and reactive power sharing. In low voltage MGs, line inductance value is considerably small with cable resistive behaviour and normally has low X/R ratio [38]. Decoupling between the active and reactive power is performed by the compensation of line impedance connected to generation units [39]. The virtual impedance loop as a potential solution performs in MGs with mismatched inductive or resistive feeder impedance to enhance power sharing accuracy. The focus is on the mismatch in output impedances of closed-loop controlled inverters. This compensation performs properly for a single generator connected to the PCC bus but does not work if there are multiple generation units. To address this issue, various approaches have been introduced such as inductive virtual impedance [40], virtual impedance adapted to power sensitivity factor [41], and virtual impedance calculated by injection of a small AC voltage signal to the PCC bus [42]. These approaches result in accurate power sharing if knowledge of the feeder impedances is available for different operating load changes. However, load changes during or between the compensation periods lead to poor power sharing among generation units [43].

1.2.3 Optimal Operation and Secondary Control

The rise of renewable generation penetrating in islanded MGs has imposed new challenges on frequency and voltage control in the secondary control level. For any changes in load or renewable generation, the primary controller stabilises the system control and improves MG's resiliency [44]. Then, UC, a working algorithm of the secondary controller, determines optimal generation schedule for the primary control level. These UC problems are mainly formulated to achieve cost and ESS efficiency through frequency and voltage regulations [45].

The scheduling of generation units in islanded MGs, based on conventional UCs, remains fixed for the duration between two dispatch intervals. However, the demand or renewable generation can continuously change. Stair-pattern scheduling of generation units creates large frequency and voltage excursions at the edge of each dispatch interval. Furthermore, the fixed scheduling is not efficient for both operation cost and life-cycle of fast-acting generation units, without addressing output renewable power variability and demand perturbations [9, 10]. In theory, it is commonly assumed that local frequency, voltage, and net demand during each dispatch interval are equal to corresponding steady-state conditions. Therefore, a timescale separation happens between fast synchronization-enforcing primary and slower secondary controllers. In general, this timescale separation affects power sharing properties and dynamical regulation of frequency and voltage in the secondary control, specifically during rapid load or renewable energy perturbations [11].

Conventional UC models include operational constraints pertaining to DGs and ESSs, such as ramp-up/down, minimum up/down time, and state of charge (SOC) of ESS. However, most of them account for the impact of frequency and voltage regulation with consideration of fixed and non-optimum generation dispatches between two time intervals [46]. Practically, due to renewable energy and load intermittency, frequency and voltage continuously deviate from their nominal values, while the output of controllable DGs and ESSs is assumed to be fixed for the duration between two dispatch intervals [47]. To address this problem, the UC model is reformulated to incorporate reserve-related constraints [48], load-frequency sensitive indices [49], and averaged energy-block constraints between two dispatch intervals [9]. These methods aim to reduce the impact of frequency and voltage control on generation output and to mitigate supply and demand imbalance. However, considering reserve requirements in terms of hourly energy blocks may not be practicable. Even though this problem can be addressed by using an averaging method for sub-hourly energy blocks to reduce operation cost, energy profiles must be modelled by an averaging piece-wise linear function, which does not achieve accurate supply and demand balance. In optimization problem formulation, a conventional UC mainly relies on offline techniques such as mixed-integer linear program [9], evolutionary algorithms [50], and model predictive control [51]. Although these approaches have advantages of simplicity in implementing the optimization model, they suffer from long decision-making time in a large-scale MG. Due to intrinsic characteristics of offline approaches, they cannot handle an optimization model with dynamic technical constraints such as the frequency and voltage control. Furthermore, reference set points of generation units can deviate from their desired values due to prediction errors associated with load or renewable energy resources [52, 53].

Recently, various online approaches have been proposed for the UC, such as neural networks [54], reinforcement learning [55], and adaptive critic design [56]. These approaches have advantages of short decision-making time, adaptation to MG conditions, and the optimization of objective function based on observations as well as predictions [16]. In existing studies, UCs update the reference power of generation units in each dispatch interval. Change of reference power shifts droop curves up or down to restore frequency and voltage. This shifting process should be done in a specific time margin after running a primary controller, which depends on the size and type of generation units, length and type of electrical network, and characteristics of loads.

1.2.4 Time Delay Impact on Controller Performance

Motivated by advantages of the hybrid model [17], this study mainly focuses on the MGCC generating reference power signals to each individual LC, and LCs sharing operating power signals together. This power sharing approach is performed in the secondary control level through low-rate communication links such as wireless networks. There exist delay sources in the MG operation, i.e., DG actuator (LC-to-DG) and communication links. Electricity transmission latency is negligible compared to other sources of delay. In power converter generation, delay is less than one pulse width modulation cycle which is 185 μs; however, the SG delay is much longer, usually measured in milliseconds. Communication delay comprises of LC-to-DG (latency up to 1.5 s), end-to-end application including LC-to-LC and LC-to-MGCC (data serial transmission, packetization, data traffic routing, and propagation delays with latency range of 4 ms-1.5 s, and the physical layer with latency range of 2-10 ms for IEEE 802.11/802.16) [12, 13]. Note that the time duration of transient stability is less than 100 ms, small-signal stability is less than 1 s and voltage stability between 1-5 s [57]. These time delays cause generation units to use outdated dispatch information for power sharing, and disable the frequency and voltage controllers from outputting the optimal power sharing among generation units. During this period, the sub-optimal output of the LCs degrades the system dynamic performance and even causes MG instability in the worst case. Consequently, it cannot be simply ignored [14]. The main objective is to optimize MG assets with accurate real and reactive power sharing while maintaining frequency and voltage in presence of communication latency.

There are two categories of stability analysis in the network induced delay control in islanded MGs, i.e., small and large-signal stability models. In the small-perturbation analysis, dominant eigenvalues calculated from the state-space model of MGs determine time delay margin. Note that time delay margin is a key metric of control system using the communication network [58]. To overcome the latency impact on islanded MGs, potential solutions have been proposed such as change in communication topology [57], gain scheduling frequency control [59], and distributed averaging approaches on MGCC and LCs [60]. Practically, any change in communication topology requires hardware solutions and is not simply applicable; hence, it is beyond the scope of this work. Within a scheduling approach, a series of trial studies lead to finding the relationships between delay margins and secondary frequency control gains. This approach compensates for the communication delay impact on MG performance by changing secondary control gains [59]. However, an offline gain scheduler cannot regulate frequency during the time delay when MG operating points change continuously. To maintain frequency and voltage regulation during the time delay, distributed averaging approaches are applied to the secondary controllers. These approaches reduce the impact of time delay in reference power values by averaging power measured by the data acquisition system on each LC [60]. Deployment of averaging methods based on broadcast gossip achieves a tight coupling between communication and control functionality in LCs [61]. On the other hand, diffusive averaging approaches cause MG instability under using realistic data communication links with feature of time-varying and non-constant.

Small-signal analysis is performed based on linearizing the nonlinear MG state variables around an operating point. However, the main drawback of small-signal analysis is that validity of stability domain is limited to accuracy of linearization around an operating point. Large-perturbation stability analyses such as Lyapunov-Krasovskii [62] and Kharitonov [63] theorems provide solutions to find the robust controller gains during the time delay.

Efforts have been made to combine the secondary control design and communication network as an integrated entity [57]. A linear guadratic regulator algorithm models the matrix of communication network which includes the parameters of closed-loop frequency control. Although this method regulates frequency and voltage precisely, it needs global positioning system signals to synchronize LCs for data exchanges among generation units [64].

Same as small-signal analysis, the compensation of communication delay by secondary controller gains can increase MG stability and improve the MG transient performance in frequency and voltage regulation. Generally, this approach relies on slow-acting DGs such as SGs [59]. Any change in frequency and voltage controller of slow-acting DGs may result in instability when fast-acting generation units exist in the MG [60]. Note that the communication delay in these studies is considered constant. Practically, communication delays in LC-to-LC or LC-to-MGCC are time-varying due to the inter-processing time on LC and the link length. To overcome these limitations, other studies aim to control the time delay with algorithms such as sliding mode control [65], model-predictive control [66], and delay-dependent control [14]. Although these solutions are effective and simple, they work based on proportional and integral gains in the secondary control level. The system can be unstable in the primary control level, which needs more investigation to find a solution.

1.2.5 Overview of MG Stability

Stable operation in islanded MGs refers to the ability of MG to regain a state of operating equilibrium after being subjected to a physical disturbance [67]. The nature of MG stability is considerably different from those of a conventional power system because of smaller size of MG. Therefore, MG stability can be categorized based on a) size of disturbance, b) physical phenomenon of instability, c) time-span during instability, and d) methodology of stability analysis. Strong coupling between system variables of MG makes it difficult to categorize frequency and voltage stability based on measurements of MG variables. Therefore, stability in MGs is classified into two main categories, i.e., a) control system stability, and b) power supply and balance stability, as shown in Table 1.2.

Power supply and balance stability refers to the ability to maintain power balance and effectively share the demand among generation units, so that steady-state values satisfy operational constraints such as acceptable ranges of frequency and voltage. This type of stability issue is associated with poor power sharing among generation units, loss of units, and violation of DGs limits. Control system stability issue may arise due to improper tuning of one or more pieces of equipment controllers. Poorly tuned controllers in electric machines and inverters are the main reason of this type of instability.

Based on the aforementioned discussion, poor power sharing among units can cause frequency and voltage instability. Frequency stability refers to the ability that the MG can maintain the steady-state frequency within an acceptable range in presence of various generation and load conditions. The convention of frequency stability can apply to voltage by considering voltage instead of frequency [68]. In subject to a disturbance, more than one type of instability may be triggered. Hence, studies are carried out to understand all types of instabilities in islanded MGs in presence of small and large disturbances. As indicated in Table 1.2, frequency and voltage stability studies are conducted to two main categories of short-term and long-term stability, depending on the duration of control process and dynamic responses of DGs. Strong coupling between voltage and frequency in MGs makes it difficult to regulate frequency and voltage. The main focus of this thesis is on short-term frequency stability, where there is not sufficient inertia of generation units required to damp the frequency change after being subjected to small or large disturbances.

Note that short-term frequency stability is the ability of an islanded MG to maintain power supply and demand equilibrium, and to reach an acceptable steady-state operating condition when subjected to disturbances such as components or line faults. Disturbances occurring in time span of a few seconds may cause MG blackout or synchronization loss in SGs. Small-signal analysis is one of the linear analysis tools to investigate short-term frequency stability, where the MG model influences analysis accuracy and calculation speed. Small-signal analysis is performed based on linearizing nonlinear variables of MG around an operating point. However, the main drawback of small-signal stability analysis is that validity of stability domain is limited to accuracy of linearization around that operating point. Furthermore, small-signal analysis is only valid around operating points with no indication of how far away from those points the linearization guarantees validation of results.

On the other hand, ESSs and SGs in an islanded MG are intrinsically nonlinear, proven by the differential-algebraic dynamic equations. Hence, large-signal analysis is necessary for stability study without linearization to tackle this issue. The complexity of large-signal analysis depends on the size of model, objective functions, and simplified assumptions. Domain of validity and effectiveness of large-signal stability analysis is much larger than that of small-signal linear analysis. In summary, a large-signal stable MG results in small-

Table 1.2: Classification of MG stability [68]

Category	**Control system**	**Power supply and balance**
Sub-category	Electric machine and inverter	Frequency and voltage
Phenomenon	Short and long-term	Short and long-term
Root cause	• Poor controller tuning; • PLL bandwidth; • LCL filter design; • Harmonic instability.	• DGs power limits; • Poor power sharing; • Load voltage sensitivities; • Inadequate power supply.
Characteristics	• Undamped oscillations; • High-frequency oscillations; • Low steady-state voltages; • Aperiodic increase or decrease in voltage or frequency.	• Low steady-state voltage or frequency; • Large power and frequency swings; • High DC-lin voltage ripples.

signal stability but the opposite is not necessarily true. Lyapunov-based techniques are commonly used in nonlinear stability to analyze short-term frequency stability. However, due to relatively large size of islanded MGs, nonlinear Lyapunov-based stability analysis is quite complex and intuitively infeasible as compared to small-signal studies [6, 69].

1.3 Objectives

The aforementioned drawbacks in conventional frequency and voltage mechanisms motivate us to set following objectives for the thesis:

1. Developing an intelligent power sharing (IPS) controller that allows for dispatching active and reactive power among generation units and maintains frequency and voltage regulation with following features:
    - Accurate active and reactive power sharing of generation units based on their droop values and operating power capabilities, which improves the life-cycle of fast-acting generation units;

   - Proper performance under rapid load or renewable energy variations while maintaining MG frequency and voltage stability;
   - A dynamic compromise between voltage regulation and accurate reactive power sharing among generation units;
   - An adaptive virtual impedance to mitigate the impact of coupling between active and reactive power on voltage regulation.

2. Developing a hybrid mid-level controller that communicates with a diffusive distributed primary controller to share the output power of dispatchable units, and determines optimal output power of units between two dispatch intervals for the secondary controller while maintaining frequency and voltage stability. Specifically, main objectives of the second problem are summarized as follows:
   - A mathematical formulation for a mid-level controller, which is integrated with a distributed controller in the primary level and a UC framework in the secondary level;
   - A fast-response controller to minimize frequency and voltage deviations while maintaining MG stability. This controller aims to achieve economic operation and battery life-cycle efficiency.

3. Developing a mathematical model of constant and time-varying delay in islanded MGs which is integrated into the proposed controller. Objectives of third problem are listed as follows:
   - An impact analysis of small and large disturbances on the proposed frequency and voltage controller. Performance evaluation of the proposed controller is to be applied on two models of constant and time-varying delays;
   - A delay-based controller to mitigate frequency oscillation of MG in presence of small and large disturbances.

Several scenarios are tested on CIGRE benchmark test system, and the results demonstrate solid performance of the proposed frequency and voltage controller.

1.4 Outline of the Thesis

In this chapter, we discuss the frequency and voltage control in islanded MGs. Control of islanded MGs is studied in three different aspects of a) functionality, b) technique and c) architecture. A review of the MG architectures, control techniques, stability models, and control levels is presented in this chapter. Frequency and voltage control challenges are mainly categorized to a) primary frequency and voltage control, b) optimal operation and secondary control, and c) the impact of time delay on both primary and secondary control. Existing primary frequency and voltage controllers aim to damp oscillatory modes of power sharing controllers and reduce steady-state frequency and voltage errors. However, with an increase in the span of islanded MG operation, it is imperative to regulate frequency and voltage of the MG not only stably but also based on generation units' droop control gains and their operating power capabilities. On the other hand, scheduling of generation units in existing secondary controllers remains fixed for duration between two dispatch intervals; however, the demand or renewable generation can continuously change. The stair-pattern scheduling of generation units creates large frequency and voltage excursions at the edge of each dispatch interval. Furthermore, the fixed scheduling is not efficient for both operation cost and ESS life-cycle, without addressing output renewable power variability and demand perturbations. Hence, a controller is needed to share the output power of dispatchable generation units, and to determine optimal output power of generation units between two dispatch intervals for the secondary controller while maintaining frequency and voltage stability. Finally, the existing primary and secondary controller uses the communication network with ignoring time delay or considering the constant time delay. For the time-varying delay, there are almost no comprehensive small and large signal models. The existing solutions have calculated time-delay margin as a potential constraint or proposed a constant gain scheduling only on the secondary controller. There is a need for an adaptive delay-based controller to be suitable for both small and large-signal models.

This thesis is organized as follows. The system model under consideration is given in Chapter 2. Chapter 3 presents a distributed frequency and voltage control model in the primary control. Chapter 4 proposes a dynamic frequency and voltage controller at the secondary control level. The time delay in the proposed controller is considered in Chapter 5. Finally, conclusions and future work on this Ph.D research are given in Chapter 6.

Chapter 2

Islanded Microgrid Model

Consider an islanded MG over a distribution network consisting of a cluster of generation units $i := \{1, 2, ..., n_G\}$, and loads $Ld := \{l_1, l_2, ..., l_{n_{Ld}}\}$, connected together within an AC link. Figure 2.1 shows that LCs of generation units are in charge of controlling the frequency and voltage as well as ensuring a stable operation. According to contribution of load and generation units in frequency and voltage control, they are categorized to controllable and non-controllable units.

In an islanded MG, different generation units are in charge of controlling frequency and voltage. Any change in generation input of power, ΔP_G, or net electrical power demand, ΔP_L, results in a frequency change, $\Delta\omega$, which is modeled as a transfer function, $F(s)$, for the control system.

In the islanded MG, there are several master and slave controllers with different time constants to maintain the MG frequency and voltage within allowable limits (during disturbances or load changes). These controllers also ensure reliable and economical operation. As mentioned in Chapter 1, an MGCC gathers different signals from all LCs through communication network and performs a signal processing task to make desirable decisions.

In the frequency control mode, controllable generation and load units change their generation and consumption power using the droop theory. As shown in Figure 2.2, LCs are designed to allow the steady-state frequency to drop as the load increases or generation of non-controllable units decreases. Slope of droop control illustrates the characteristics of speed regulation or droop m_p. Generally, droop value for generation units is defined as follows:

$$m_p = \frac{\omega_n - \omega_0}{\Delta P_G} \times 100, \tag{2.1}$$

where ω_n and ω_0 are rated and steady-state frequency, respectively. As can be seen in Figure 2.2, controllable loads, with index of cl, change their demands in order to contribute to the

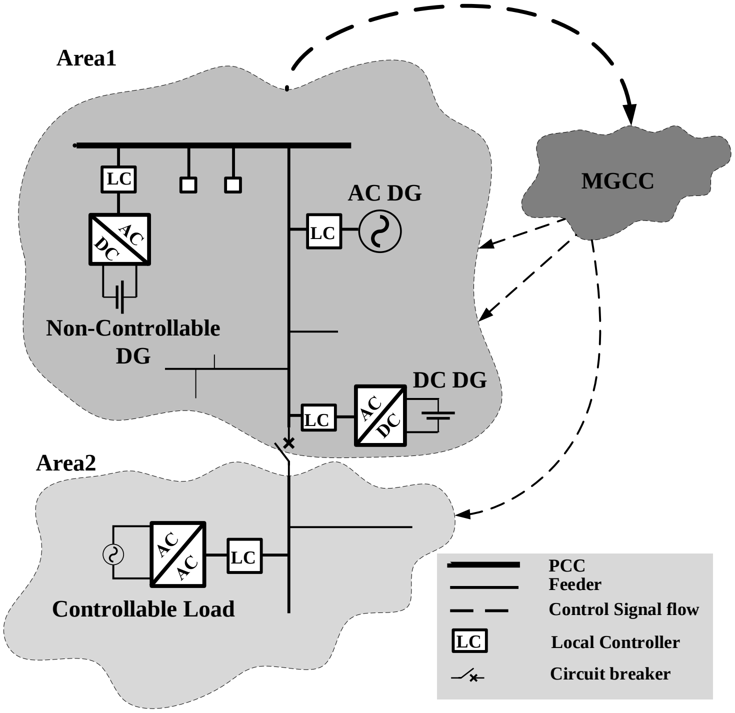

Figure 2.1: General architecture of an islanded MG.

frequency control. Figure 2.2 shows that reducing power of controllable loads has similar impact of increasing generation power in units.

In the voltage control mode, the reactive power sharing among different generation units is achieved through the control of output voltage magnitude, as shown in Figure 2.2. The voltage droop control is as follows:

$$n_p = \frac{V_n - V_0}{\Delta Q_G} \times 100, \tag{2.2}$$

where V_n and V_0 are rated and steady-state voltage magnitude of the AC link, respectively. Operating points of active and reactive power are represented by P_{dg0} and Q_{dg0}, respectively. The reference power for controllable load is P_{cl0}. Note that droop values for inverter-based generators are achieved from active and reactive power change corresponding to maximum and minimum frequency and voltage.

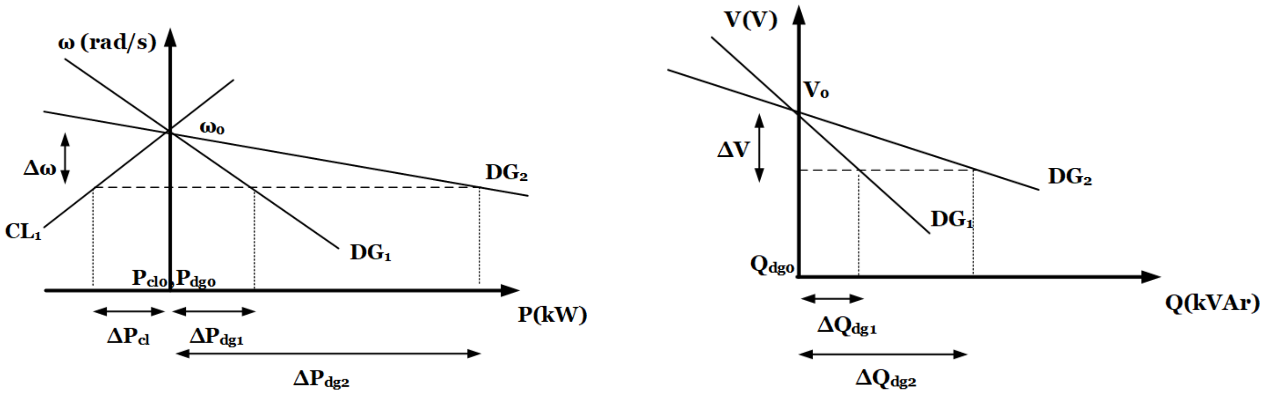

Figure 2.2: Frequency (left) and voltage (right) regulation in droop mode for two DGs and controllable load.

2.1 Inverter based-Generators

Most generation units such as ESSs, photo voltaic panels, and fuel cells in an islanded MG operate as DC generators connected to the AC link via DC/AC inverters. Figure 2.3 shows the stage of three-phase three-leg inverter supplied by a DC link ending with an LCL filter connected to the AC link. An LCL filter is designed to remove the switching harmonics produced by the inverter. Voltage and current at the AC link are measured to control the inverter generated power. Generally, this control system consists of two cascaded control loops; a) joint power and voltage control and b) current control. The design of this structure can be understood further by investigating the operation of inverter connected to the LCL filter. There are two energy storage elements (L and C), which make a second-order transfer function for the voltage control. In order to guarantee a stable operation of the MG under all conditions, interactions between capacitor and inductance should be decoupled by definition of two control loops [70]. For simplicity of control diagram, an average model of inverter with no effect of switching components is considered.

a) Power and voltage control loop: This loop achieves the required power sharing functionality through output voltage magnitude and frequency of the inverter and droop control setting. The control loop consists of different block diagrams such as a power calculator, V/f reference generator, and voltage controller.

In the first part, current and voltage values are measured from the output of LCL filter and then transferred to Park's dq-coordinates. This mapping operation removes current

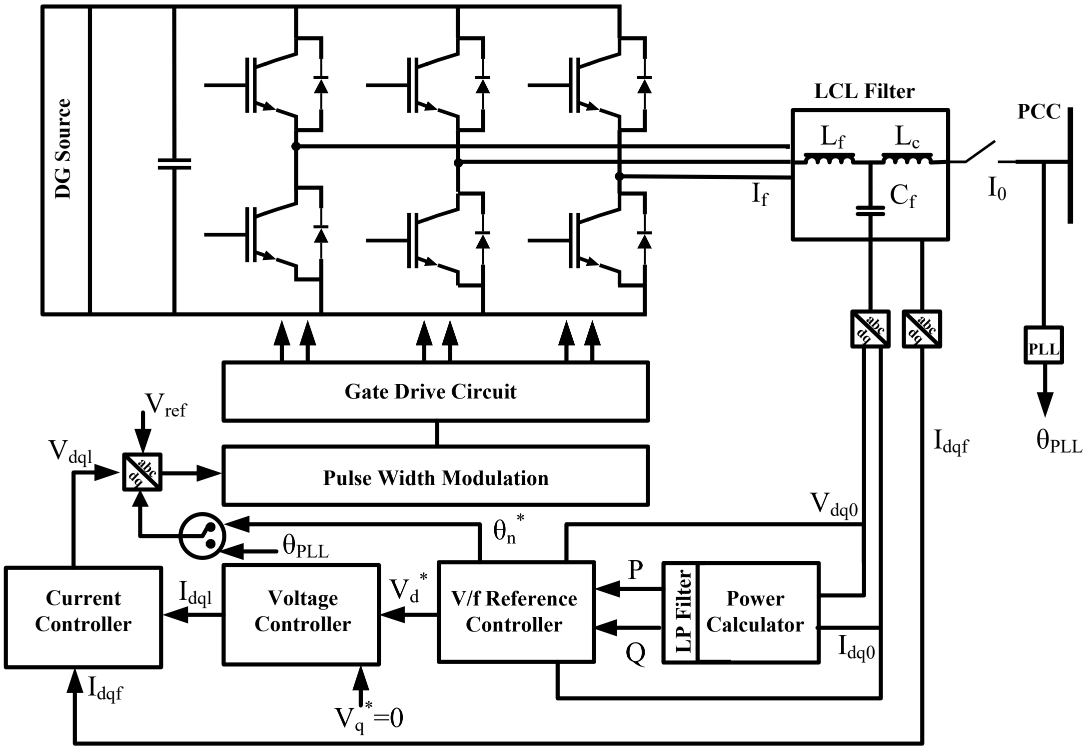

Figure 2.3: Control diagram of an inverter-based unit in the islanded MG [70].

and voltage angles from the active and reactive power calculation. The power calculator block computes active and reactive power according to the following equations:

$$p = v_{d0}i_{d0} + v_{q0}i_{q0}, \tag{2.3a}$$

$$q = v_{d0}i_{q0} - v_{q0}i_{d0}, \tag{2.3b}$$

where v_0 and i_0 are output voltage and current converted to dq-coordinates, respectively. As shown in Figure 2.4, an LPF with a cut-off frequency ω_c is used to filter the ripple components when calculating P and Q. Furthermore, LPF stabilizes the droop controller

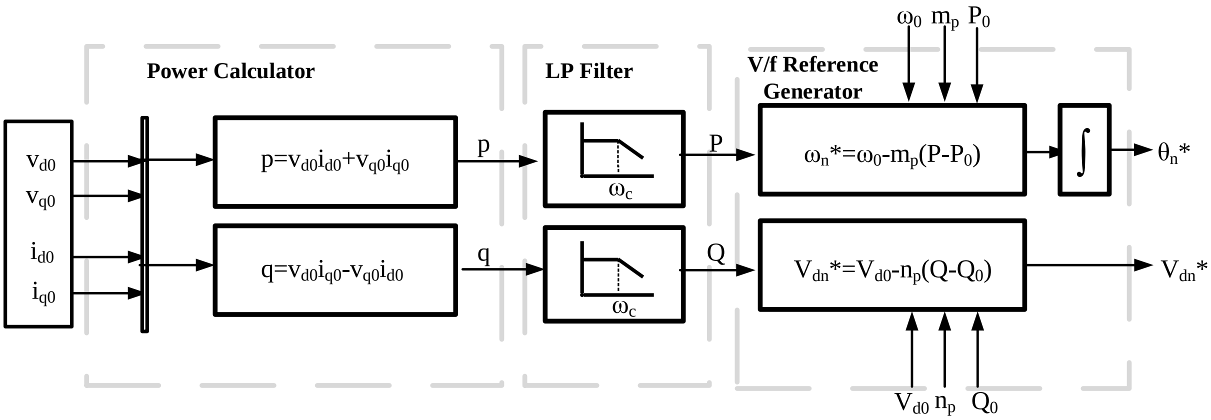

Figure 2.4: Power control loop in an inverter-based unit [71].

in the proposed model.

$$P = \frac{\omega_c}{s+\omega_c} \times p, \tag{2.4a}$$

$$Q = \frac{\omega_c}{s+\omega_c} \times q. \tag{2.4b}$$

A V/f reference generator regulates the system frequency and voltage by two droop control loops formulated as follows:

$$\omega_n = \omega_0 - m_p \cdot (P - P_0), \tag{2.5a}$$

$$\theta_n = \int \omega_n dt, \tag{2.5b}$$

$$V_{dn} = V_{d0} - n_p \cdot (Q - Q_0), \tag{2.5c}$$

$$V_{qn} = 0, \tag{2.5d}$$

where P_0 and Q_0 are the full-load active and reactive power, respectively; V_{d0} is the full-load voltage of PCC, and m_p and n_p are the slope of frequency and voltage droop control, respectively. The q-component of voltage is set to zero because of its independency to reactive power control [71].

The voltage controller generates reference current for the next control block. Output current of voltage controller can be controlled within an acceptable steady-state error and a desired transient behavior. This block receives reference voltage from the V/f reference generator, and determines reference current according to the PI block diagram as follows:

$$I_{dn} = I_{d0} + K_{pv}(V_{dn} - V_{d0}) + K_{iv}\int (V_{dn} - V_{d0}) \cdot dt + \omega_n C_f V_{q0}, \tag{2.6a}$$

$$I_{qn} = I_{q0} + K_{pv}(V_{qn} - V_{q0}) + K_{iv}\int (V_{qn} - V_{q0}) \cdot dt + \omega_n C_f V_{d0}, \tag{2.6b}$$

where I_{dn} and I_{qn} are reference current in dq-coordinates that is passed to the current block controller; K_{pv} and K_{iv} are proportional and integral gains of the voltage controller used to damp the transient behavior of inverter. The $q-$ and $d-$forms of voltage are used for I_{dn} and I_{qn} by filter capacitor C_f [20].

b) Current control loop: To design the current control loop, voltage drop v_{Lf} across the filter inductor is calculated by

$$v_{Lf} = v_i - v_0 = L_f \frac{di_{Lf}}{dt}. \tag{2.7}$$

The corresponding transfer function is first order, and can be controlled with a proportional controller to achieve the required closed-loop control. However, due to switching dead-times, some considerable non-linearities appear in the current waveform. This unformed current waveform affects the final voltage waveform; hence, an integral term is added to remove the unbalance waveform and steady-state errors. Note that the proposed controller leads to phase shifts on feedback signals. In order to avoid this problem, the analysis is done in dq-coordinates, and dynamics of current controller can be given by

$$V_{d0}^* = K_{pi}(I_{dn} - I_{d0}) + K_{ii}\int (I_{dn} - I_{d0}) \cdot dt - \omega_n L_f I_{q0}, \tag{2.8a}$$

$$V_{q0}^* = K_{pi}(I_{qn} - I_{q0}) + K_{ii}\int (I_{qn} - I_{q0}) \cdot dt + \omega_n L_f I_{d0}, \tag{2.8b}$$

where V_{d0}^* and V_{q0}^* are the reference voltage of inverter switches, and K_{pi} and K_{ii} are the proportional and integral gains of current controller, respectively. In order to generate reference voltage of inverter switches, the dq-coordinates voltage is transformed into abc-coordinates. The voltage phase is achieved from difference between the AC link phase and the reference angle calculated in power and voltage loop control.

The power and voltage loop control should be designed with a bandwidth 3-5 times slower than current control loop in order to ensure stable operation [20]. The reference current is an essential input for switching drive circuit; hence, bandwidth of current controller should cover voltage and power control's bandwidth. Note that current loop bandwidth is usually bounded by the inverter switching frequency, and that of power and voltage control loop is determined by a low-pass filter cut-off frequency. To do so, the cut-off frequency in LCL filter is designed to be below the switching frequency [6].

2.1.1 Virtual Impedance

The feeder impedance causes a voltage drop across the line connected to generation units. Hence, this voltage drop deviates output voltage from its nominal value. So as to ensure proper voltage regulation and stability, the virtual impedance is installed on the unit terminal [41]. Virtual impedance damps MG oscillations and decouples active and reactive power sharing with no power losses and efficiency degradation. This technique determines virtual impedance by analyzing voltage drop across the feeders. The voltage drop across the feeder impedance ($Z_i = R_i + jX_i$) can be approximated as follows

$$\Delta V_i \approx \frac{X_i Q_i + R_i P_i}{V_0}, \qquad i \in \Lambda_G \tag{2.9}$$

where P_i and Q_i are active and reactive power, measured at the terminal of generation units in kW and $kVAr$, respectively. The virtual impedance, Z_v, is added to voltage control loop to compensate for voltage drop, and to generate an equal voltage drop in all inverters connected to the AC link. Figure 2.5 shows virtual impedance added to the voltage and current controller [72]. The new impedance of the i^{th} inverter can be derived as follows:

$$R_i^* = R_i + \mathrm{Re}\{Z_v\}, \tag{2.10a}$$

$$X_i^* = X_i + \mathrm{Im}\{Z_v\}, \qquad i \in \Lambda_G. \tag{2.10b}$$

2.2 Synchronous Generators

In the islanded MG, SGs such as micro-turbines and diesel generators play vital roles in frequency and voltage regulation. In this section, we discuss frequency and voltage controllers of SGs that are connected directly to the MG. The SG consists of different parts such as governor, turbine, and AC machine, as shown in Figure 2.6.

Frequency in SG changes due difference between driving mechanical power ΔP_m and elec-

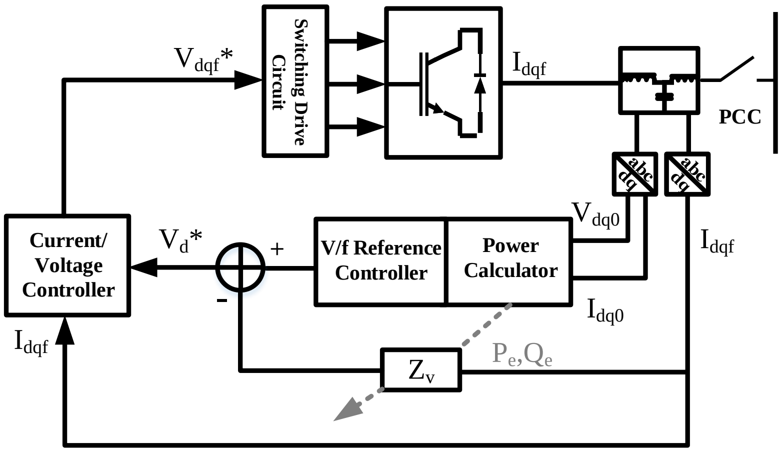

Figure 2.5: Inverter controller design with virtual impedance consideration.

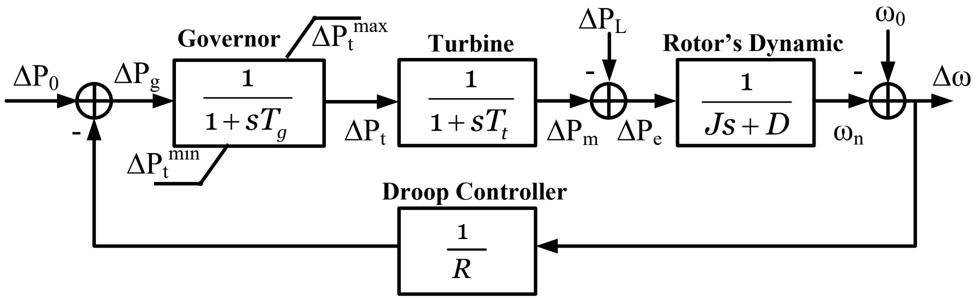

Figure 2.6: Frequency control block diagram of SG with ΔP_L as an input.

trical power developed by generator ΔP_e according to swing theory $Jd(\Delta\omega/\Delta t)/dt = \Delta P_m - \Delta P_e$. This simple model of SG is presented by a linear relationship between frequency deviation and output power change. Note that we use linear model for each component of frequency controller as depicted in Figure 2.6. In this model, ΔP_e is sensitive to changes in system frequency because of inductive behavior of loads. Hence, output power model, considering frequency impact on generator, can be represented as $\Delta P_e = \Delta P_m - \Delta P_L + D\Delta\omega$, where D is coefficient used to show the amount of change in the load over frequency change $(kW)/Hz$, and ΔP_L is a load change.
The purpose of turbine is to provide mechanical power ΔP_m for SG. Turbines perform based on changes in valve position of steam with time constant T_t and input power of ΔP_t. To adjust turbine valve position, governor receives a generation signal, ΔP_g, and

generates valve command with a specific time delay T_g. The signal sending to turbine is limited to lower and upper bound $(\Delta P_t^{min}, \Delta P_t^{max})$. The command received from governor is calculated from deviation over system frequency in droop control model, R, and change in reference power ΔP_0 [70, 6].

$$\Delta P_m = \frac{1}{1 + sT_t}\Delta P_t, \tag{2.11a}$$

$$\Delta P_t = \frac{1}{1 + sT_g}\Delta P_g, \tag{2.11b}$$

$$\Delta P_g = \Delta P_0 - \frac{1}{R}\Delta\omega. \tag{2.11c}$$

The transfer function of SG frequency control is given by

$$G_1(s) = \frac{1}{R(1 + sT_g)(1 + sT_t)}, \tag{2.12a}$$

$$G_2(s) = \frac{1}{Js + D}, \tag{2.12b}$$

$$G_f(s) = \frac{-\Delta P_L(s)}{\Delta\omega(s)} = \frac{G_1(s)}{1 + G_1(s)G_2(s)}. \tag{2.12c}$$

During small perturbations, an automatic voltage regulator (AVR) in SGs regulates output voltage and controls reactive power by controlling generator field excitation. The signal of exciter is limited to lower and upper bounds $(\Delta V_g^{min}, \Delta V_g^{max})$ to avoid voltage instability in generator. Linear models of amplifier, exciter, generator, and sensor comprise the block diagram of AVR. These models are presented as a first-order transfer function. The total transfer function of the AVR can be written as:

$$\begin{aligned} G_v(s) &= \frac{\Delta V_t(s)}{\Delta V_0(s)} \\ &= \frac{K_A K_E K_G (1 + sT_S)}{(1 + sT_A)(1 + sT_E)(1 + sT_G)(1 + sT_S) + K_A K_E K_G K_S}. \end{aligned} \tag{2.13}$$

Terminal voltage is controlled by changing the SG reference voltage as depicted in Figure 2.7 [73].

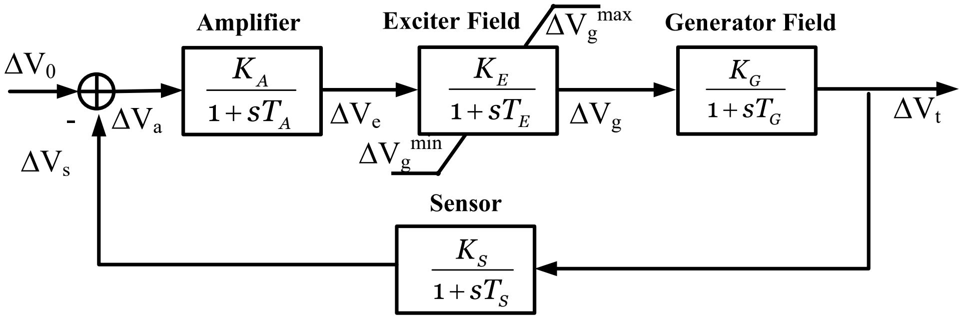

Figure 2.7: AVR block diagram of the SG [73].

2.3 Voltage Dependent Load

Static characteristics of a load can be classified into ZIP models, namely constant impedance (Z-model, quadratic dependency to voltage), constant current (I-model, linear dependency to voltage), and constant power (P-model, independence to voltage) [74]. This ZIP model is formulated as

$$P_L = P_{L0}(\frac{V_L}{V_{L0}})^{k_p}, \tag{2.14a}$$

$$Q_L = Q_{L0}(\frac{V_L}{V_{L0}})^{k_q}, \tag{2.14b}$$

$$k_x \approx \frac{2 \times Z_x + 1 \times I_x + 0 \times P_x}{Z_x + I_x + P_x}, \qquad x \in \{p, q\} \tag{2.14c}$$

where P_x, Z_x and I_x are constant power, impedance, and current coefficients for active and reactive power, $x \in \{p, q\}$, to determine load sensitivity coefficient, k_x [6]. In addition, P_L and Q_L are active and reactive power after voltage deviation V_L; and P_{L0} and Q_{L0} are active and reactive power under nominal voltage (V_{L0}), respectively. Note that there is no ideal constant current or impedance, we use a load voltage-dependent model presented in [31]. In case of voltage-dependent load, loads are modelled 60% constant impedance, 30% constant current, and 10% constant power loads, i.e., $k_p = k_q = 1.5$. Therefore, loads operate at their nominal voltage prior to any voltage change ΔV_L, and load change $\Delta P_L + j\Delta Q_L = ((1 + \Delta V_L)^{1.5} - 1)\,(P_{L0} + jQ_{L0})$.

2.4 Summary

In this chapter, the model of an islanded MG with main components is discussed. Three main components are considered: 1) inverter-based generation unit, 2) SG, and 3) voltage dependent load. Frequency and voltage control diagrams of inverter-based generation unit and SG with corresponding equations are presented. In the case of inverter-based units, a virtual impedance is added to the voltage control diagram to regulate the output voltage of inverter-based units.

Chapter 3

Distributed Frequency and Voltage Controller Design

This chapter compares the performance of a new distributed frequency and voltage control method in an islanded MG with the conventional droop control methods. Note that frequency and voltage control in the islanded MG corresponds to active and reactive power sharing among generation units. Hence, this distributed frequency and voltage control method is designed as an IPS approach. The IPS controller allows for dispatching active and reactive power among generation units based on their droop control gains and operating power capabilities. Furthermore, the IPS controller improves frequency and voltage regulation compared to conventional droop-based control approach. To describe the power sharing problem, two DGs in an islanded MG dispatch active and reactive power under 1) conventional droop control and 2) IPS control approaches.

In the conventional droop-based control, a generator with a higher droop control value contributes less to compensating load perturbations in the islanded MG. To regulate the frequency and voltage to nominal values, the secondary controller shifts droop curves. In conventional approach, this frequency regulation is performed by PID implemented in a supplementary control loop. Care should be taken to tune the droop controller so as to avoid making the DGs generate power close to their full-load rating. As an illustration, Figure 3.1 shows the uniform active and reactive power sharing used to regulate system frequency and voltage with two DGs. Under conventional power sharing paradigm, active power of DG_2 reaches the maximum value ($\overline{P}_{DG_2}$) which is unrealistic. In addition, application of uniform voltage-regulating ensures that both DG voltage magnitudes are restored to a common steady-state voltage (V_0^1). However, different reactive power injections and line impedance effects cause bus voltages to deviate from the common value. It is concluded

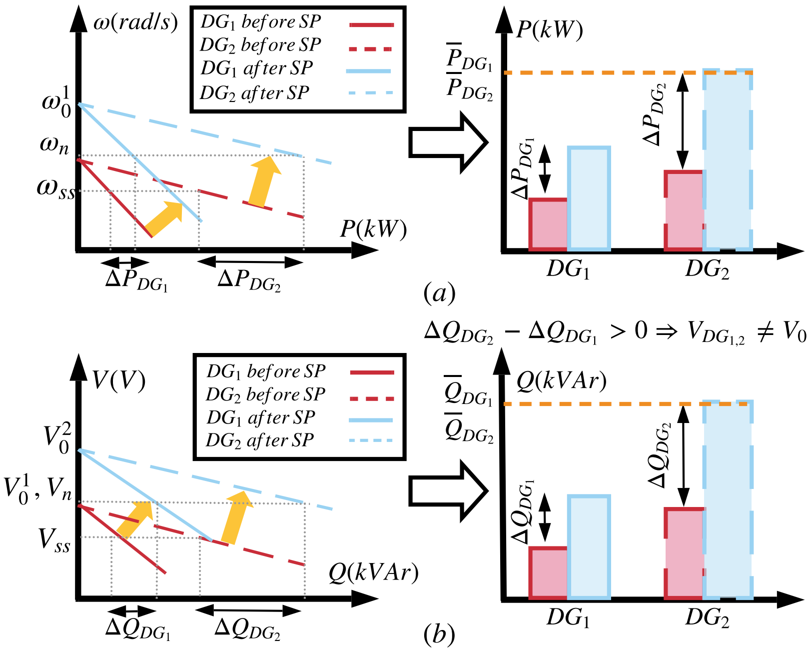

(a)

(b)

Figure 3.1: Conventional secondary controller for (a) active (b) reactive power sharing before and after shifting process (SP).

that an ideal power sharing controller should allow for a tuneable compromise between frequency and voltage regulation and DG operating power capability. It should also keep voltage between upper and lower limits, while maintaining accurate reactive power sharing.

3.1 Proposed Frequency and Voltage Controller

The IPS controller relies on the distributed communication network to propagate unit parameter information, including operating and rated power and droop controller gain. This controller leads to desired frequency and voltage regulation, accurate active power sharing, and tuneable trade-off between voltage regulation and reactive power sharing. The distributed architecture aims to reduce the steady-state frequency and voltage errors with introduction of control signals. The communication structure among DGs is described by a weighted frequency adjacency matrix, $[W_f]$, in the order of $n_G \times n_G$ with elements $a_{ij} = a_{ji}$. For instance, if two frequency-controllable units, i and j, are connected, the arrays of the adjacency matrix are $a_{ij} = -\hat{a}_{ij} = -1$. Same convention is applied to the voltage adjacency matrix, $[W_v]$, where LCs in charge of reactive power sharing communicate together to maintain voltage regulation. The voltage adjacency matrix may differ from the frequency one due to characteristics of generation units in power sharing. Figure 3.2 illustrates the adjacency matrix of frequency when four DGs are connected together via a communication network. The IPS controller relies on control signals to unevenly shift frequency and voltage droop curves to achieve better power sharing among generation units. This uneven shifting process (SP) requires that neighboring units exchange information to operate in the secondary control. Observe in Figure 3.3 that uneven shifting approach shares the desired active and reactive power among generation units to maintain frequency and voltage regulation and operating power capability of generation units.

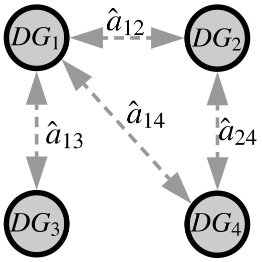

$$a_{ii} = \sum_{j\in\Lambda_G} \hat{a}_{ij}$$

$$a_{ij} = -\hat{a}_{ij}$$

$$W_f = \begin{pmatrix} 3 & -1 & -1 & -1 \\ -1 & 2 & 0 & -1 \\ -1 & 0 & 1 & 0 \\ -1 & -1 & 0 & 2 \end{pmatrix}$$

Figure 3.2: Frequency adjacency matrix and corresponding graph for four DGs.

3.1.1 IPS Control for Frequency Regulation

The control signal achieved from a frequency change, $\Delta\omega$, aims to reduce steady-state error and shifts droop curve. As illustrated in Figure 3.4, $[K]$ is a diagonal matrix illustrating the fraction of contribution in frequency control based on generation power capability and droop values ($m_{pi} > 0$), given by

$$k_{ii} = \frac{(\overline{P}_i - P_{e,i})/m_{pi}}{\sum_{j\in\Lambda_G}(\overline{P}_j - P_{e,j})/m_{pj}}, \qquad i \in \Lambda_G. \tag{3.1}$$

The LCs communicate with each other by frequency adjacency matrix,$[W_f]$, to improve MG stability by having the same control signal, $(K^f_{tr} sI + [W_f])^{-1}\Delta\omega(s)$, for all committed

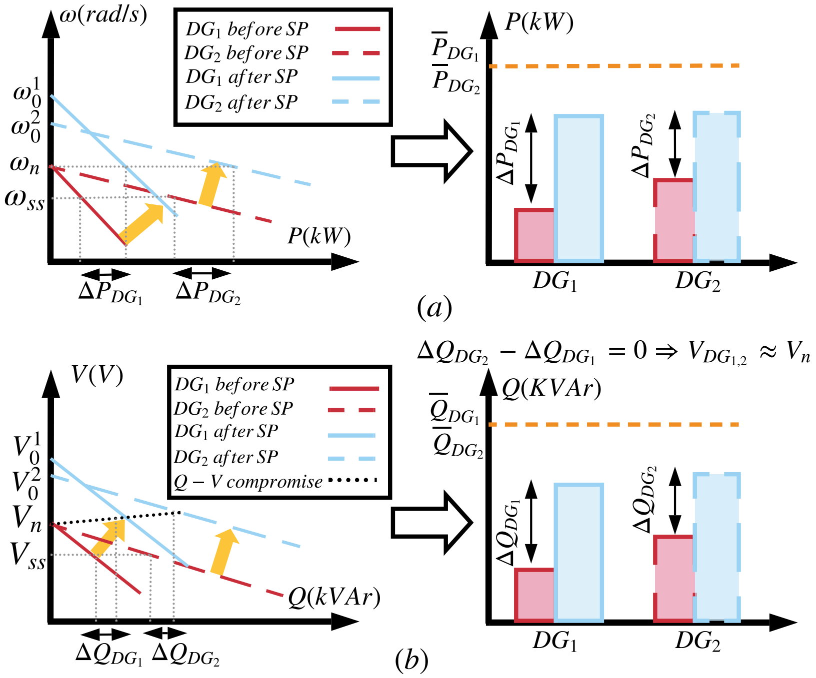

Figure 3.3: Uneven SP for (a) active (b) reactive power sharing.

generation units. This correction is aimed to shift all droop control curves by a coefficient based on $\omega_n - \omega_{ss}$ to achieve the desired active power sharing. Operating active power is calculated according to average model (2.3a) and subtracted from reference active power, P_0. In addition, a frequency-transient matrix, $[K_{tr}^f]$, is added to the control variable in order to adjust the speed of frequency restoration. For instance, a smaller K_{tr}^f corresponds to a slower transient frequency response. Updating the IPS frequency controller gain achieves active power sharing among the generation units, with consideration of frequency regulation speed ($1/m_{pi}$) and generation operating power capability ($\overline{P}_i - P_{e,i}$).

3.1.2 IPS Control for Voltage Regulation

The IPS controller achieves a trade-off between reactive power sharing and voltage regulation. As illustrated in Figure 3.5, the LCs communicate with each other by voltage adjacency matrix, $[W_v]$. Each unit generates reactive power in proportion to its rated reactive power in a matrix format ($[\overline{Q}]^{-1}$). It regulates the voltage based on a control signal

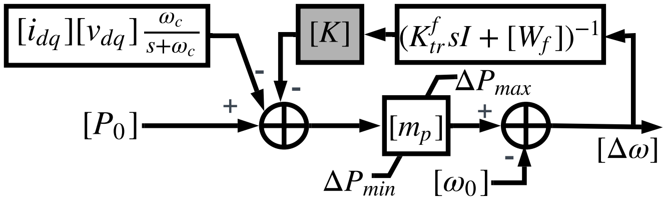

Figure 3.4: Diagram of frequency controller in the IPS control with limits on active power change ($\Delta P_{min}, \Delta P_{max}$).

consisting of voltage error ($V_{di} - V_{d0}$) and reactive power sharing of generation units. To make a trade-off between output voltage and reactive power sharing, the voltage-regulating controller uses the signal of $(Q_i/\overline{Q}_i - Q_j/\overline{Q}_j)$, and a Q-V compromise coefficient matrix $[\beta]$. Operating reactive power,Q_i, is calculated according to average model (2.3b) and subtracted from reference active power, Q_0. Similar to frequency consensus, a diagonal matrix, $[\kappa]$, is represented as the fraction of generation units' contribution in the voltage regulation based on operating reactive power capability and voltage droop value, $n_{pi} > 0$, given by

$$\kappa_{ii} = \frac{(\overline{Q}_i - Q_{e,i})/n_{pi}}{\sum_{j\in\Lambda_G}(\overline{Q}_j - Q_{e,j})/n_{pj}}, \qquad i \in \Lambda_G. \tag{3.2}$$

To adjust the speed of voltage response in system control, a voltage-transient coefficient is added to the IPS model. In addition, voltage regulation and reactive power sharing are compromised by a V-Q gain to achieve a common bus voltage and semi-equal reactive power sharing. This tuning sets up a leader-follower relationship among generation units, where equal voltages at DGs cause undesired reactive power distribution. As depicted in Fig. 3.3 (b), the V-Q compromise gain allows voltage to deviate from the nominal value to share semi-equal reactive power values (semi-equal signals for x_i mean $x_i \approx x_j, i \neq j$). Note that $\beta = 0$ means there is no voltage regulation, and $\beta = 1$ shows a highly voltage-regulating controller. Table 3.1 summarizes qualitative effect of IPS coefficients.

3.1.3 Power Flow Constraints

To solve the power flow of any system, the first step is to identify the types of buses present in that system. In a multi-source islanded microgrid, the assumption of any DG to

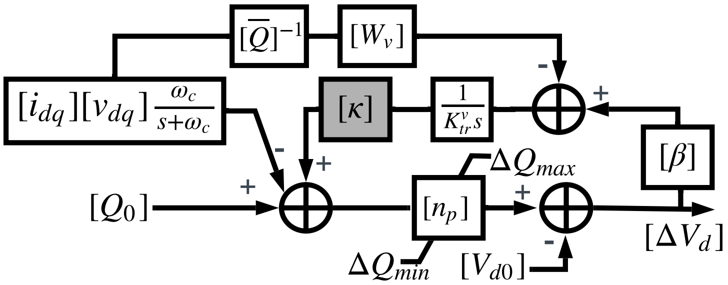

Figure 3.5: The schematic of voltage-regulating IPS control bounded by reactive power changes $(\Delta Q_{min}, \Delta Q_{max})$.

Table 3.1: Sensitivity analysis in changing IPS coefficients

Gain	**Analytical effect upon increase**
k_i	Increases active power sharing at $\mathrm{DG_i}$
κ_i	Increases reactive power sharing at $\mathrm{DG_i}$
K_{tr}^{f}	Accelerates frequency regulation for DGs
K_{tr}^{v}	Accelerates voltage regulation for DGs
β_i	Improves voltage regulation at $\mathrm{DG_i}$

act as a slack bus is inoperative as there is no single DG capable of maintaining the system frequency and its local bus voltage constant In this study, we re-classify the bus types for islanded MGs as follows:

1. PQ bus: The active and reactive powers of the bust are dependent upon the voltage magnitude:

$$P_i + jQ_i = P_{i,0}(\frac{V_i}{V_{i,0}})^{k_p} + Q_{i,0}(\frac{V_i}{V_{i,0}})^{k_q}, \qquad i \in \Lambda_L. \tag{3.3}$$

2. PV bus: The generated active and reactive powers $(P_i + jQ_i, i \in \Lambda_G)$ are calculated from Figures (3.4) and (3.5).

For N_g number of PV buses in the system, the sum of active and reactive powers $(P_{sys} + jQ_{sys})$ can be represented as

$$P_{sys} + jQ_{sys} = \sum_{i \in \Lambda_G} (P_i + jQ_i). \tag{3.4}$$

Define impedances $z_{ij} = |z_{ij}|\angle{-\phi_{ij}}$ for angles $\phi_{ij} \in [-\pi/2, \pi/2]$ for all $\{ij\} \in \mathcal{B}$, admittance matrix Y with elements $y_{ij} = y_{ji} = -1/z_{ij}$ for $i \neq j$, and $y_{ii} = \sum_{j \in \Lambda_G} 1/z_{ij}$. Each bus is associated with an electrical injection $S_i = P_i + jQ_i$, and voltage phasor $V_i \angle \theta_i$ with $V_i > 0$. The calculated active and reactive nodal power injections are given by [75]:

$$P_{c,i} + jQ_{c,i} = \sum_{j \in \Lambda} Y_{ij} V_i V_j e^{(\phi_{ij} - \theta_i - \theta_j)}, \qquad i \in \Lambda = \Lambda_G \cup \Lambda_L. \tag{3.5}$$

These calculated powers are compared with scheduled power obtained from (3.3) and Figures (3.4) and (3.5) to get mismatch matrix (Δ), given by

$$\Delta = [P^T - P_c^T, Q^T - Q_c^T]^T, \tag{3.6}$$

where $P + jQ$ is matrix of scheduled power. $P_c + jQ_c$ is matrix of calculated power. Equation (3.5) are then differentiated with respect to the voltage angle and magnitude to achieve the Jacobian matrix. Once the Jacobian matrix, J, is obtained, the voltage angle and magnitude for all buses for the (i + 1) iteration can be calculated as $x^{i+1} = x^i + J^{-1}.\Delta$, where $x = [\theta^T, V^T]^T$. In order to solve for the voltage angle and magnitude of a droop bus at the (i+1) iteration, the active and reactive powers of the droop buses need to be calculated (to be added to the mismatch matrix).

$P_{tot} + jQ_{tot}$ is the sum of the total power demand and power loss $P_{loss} + jQ_{loss}$, given by

$$\begin{aligned} P_{tot} + jQ_{tot} = {} & \sum_{i \in \Lambda_L} (P_i + jQ_i) + P_{loss} + jQ_{loss}, \\ & \sum_{i \in \Lambda_L} (P_i + jQ_i) + \frac{1}{2} \sum_{i \in \Lambda} \sum_{j \in \Lambda} \big(Y_{ij} (V_k^* V_j + V_k V_j^*) \big), \quad \Lambda = \Lambda_G \cup \Lambda_L. \end{aligned} \tag{3.7}$$

The modified mismatch matrix ($\Delta^* = [\Delta, P_{sys} - P_{tot}]$) is comprised from mismatch matrix, $Delta$, and the difference between P_{sys} and P_{tot}. The objective is to make the modified mismatch matrix equal to zero. The theory behind MNR involves consideration of a mismatched power matrix and corresponding Jacobian matrix in an iteration process. This algorithm is fully explained in [75]. It should be noted that conventional Newton Raphson method has certain drawbacks such as lack of slack bus, sparse admittance matrix in the case of inverter-based MG, and inconsistency of voltage and frequency due to droop characteristics. Hence, the IPS approach uses modified Newton-Raphson (MNR), taking account the droop characteristics of generation units.

3.1.4 Adaptive Virtual Impedance

To better illustrate the virtual impedance model, we denote V_i^* as output voltage of generator, δV_i^* as voltage drop due to virtual impedance, δV_i as voltage drop due to $\Delta R_i + j\Delta X_i$, and V_{PCC} as PCC voltage. Note that with a properly designed voltage controller, the voltages at output LCL filter of the DG match reference voltage $V_i^* + \delta V_i^*$ at steady-state value. Based on Figure 3.6 and (2.9), we have

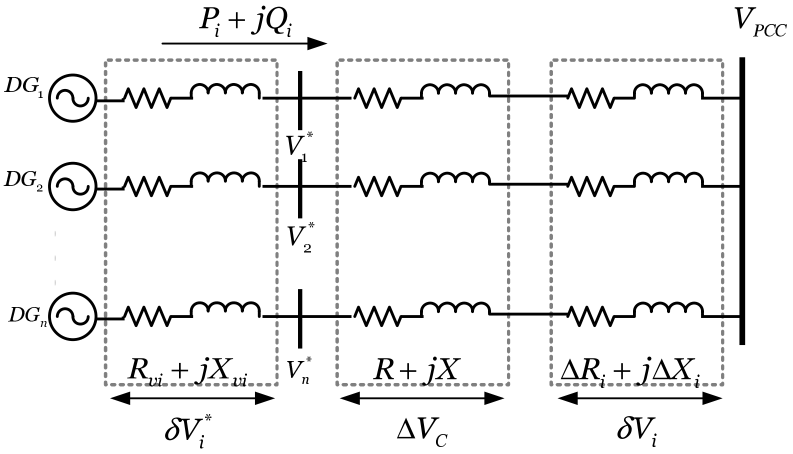

Figure 3.6: Detailed network model for virtual impedance analysis.

$$\Delta V_i \approx \Delta V_c + \delta V_i, \tag{3.8a}$$

$$\Delta V_c = \frac{X_i Q_i + R_i P_i}{V_0}, \tag{3.8b}$$

$$\delta V_i = \frac{\Delta X_i Q_i + \Delta R_i P_i}{V_0}, \qquad i \in \Lambda_G \tag{3.8c}$$

where ΔV_c is the constant voltage drop for all generation units in (3.8b). The effect of voltage drop mismatch due to ΔX_i and ΔR_i on reactive power sharing represented in (3.8c) can be compensated by virtual impedance ($Z_{vi} = R_{vi} + jX_{vi}$) which modifies the reference voltage V_i^*. The reference voltage shown in Figure 3.6 is given by

$$V_i^* = V_{PCC} + \Delta V_c, \tag{3.9a}$$

$$\delta V_i^* + \delta V_i = 0, \qquad i \in \Lambda_G. \tag{3.9b}$$

Using a simple approximation equation (3.9a), the virtual impedance calculation is simplified to

$$-\frac{X_{v,i}Q_i + R_{v,i}P_i}{V_0} \approx \frac{\Delta X_i Q_i + \Delta R_i P_i}{V_0}, \tag{3.10a}$$

$$R_{v,i} = f_{sv,i} R_i \tag{3.10b}$$

$$X_{v,i} = f_{sv,i} X_i, \tag{3.10c}$$

$$f_{sv,i} \approx -\frac{\Delta X_i + \Delta R_i (P_i/Q_i)}{X_i + R_i (P_i/Q_i)}, \qquad i \in \Lambda_G \tag{3.10d}$$

where the virtual impedance sensitivity variable, $f_{sv,i}$, converts inputs of deviation over calculated virtual resistance and inductance to smooth virtual impedance. In addition, this variable can be adjusted by a sensitivity analysis of bus voltage with respect to deviations of virtual impedance [41]. As illustrated in Figure 3.7, the proposed virtual impedance compensates for voltage drop across the feeder impedance with active and reactive reference power P and Q of generator. Virtual resistance and reactance are implemented in dq-coordinates where Δv_d and Δv_q represent voltage drop across the feeder impedance in both coordinates. Resistance and inductance changes are limited by the constraints $[\Delta R_v^{min}, \Delta R_v^{max}]$ and $[\Delta X_v^{min}, \Delta X_v^{max}]$, respectively. Existing virtual impedances are designed to compensate the mismatch in output impedances in the closed-loop controlled DG units. The drawback of virtual impedance techniques is that they require knowledge of feeder impedances which is often not readily available. In this study, a sensitivity variable is utilized to tune the virtual impedances in order to compensate for the mismatch in voltage drops across feeders. This variable is achieved for each DG unit individually. The proposed virtual impedance is straightforward to implement and does not require knowledge of the network. Furthermore, this proposed virtual impedance is insensitive to time delays in the communication channels which are utilized in the distributed scheme. Note that accurate reactive power sharing causes voltage deviation in load perturbations; hence, frequent changes of virtual impedance are necessary when voltage is deviated from the nominal value.

3.1.5 Voltage based Frequency Controller of SG

Due to use of voltage dependent loads and non-linearity in the perturbation behaviours, the AVR and frequency droop control of SGs presented in Chapter 2 are combined to sta-

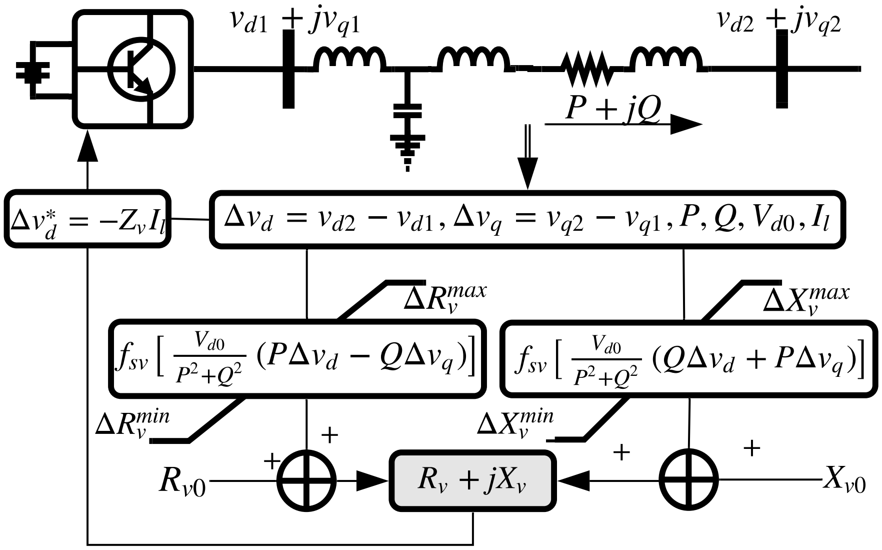

Figure 3.7: Adaptive virtual impendance in the IPS scheme.

bilize SG. Figure 3.8 depicts the voltage based frequency control of SG in an islanded MG. Input signal to voltage based frequency controller of SG (VFCSG) is the active load variation ΔP_L. This load variation causes system frequency deviations from the nominal value. Frequency error signal achieved from the droop control loop is passed through proportional and integral (PI) module with respective gains of K_P and K_I to reduce the steady-state voltage error. Then, a lead-lag block with time constants τ_1 and τ_2 compensates for input and output of voltage control loops. This frequency-voltage controller introduces a gain, $K_{\delta i}$, which damps the oscillation generated by the frequency control loop, and determines the relation between system's operating frequency and voltage. Observe that this VFCSG acts in a structure similar to that of a power system stabilizer (PSS); however, the fundamental differences exist in performance of VFCSG and PSS. Although PSS performs to mitigate low frequency oscillations in the range of 1-2 Hz which are common in large power systems with inter-transmission tie lines, the VFCSG is designed to reduce effects of large frequency changes. PSS uses derivatives of rotor frequency of SG, whereas the VFCSG acts on proportional-integral of frequency change to play a vital role as a virtual reserve that covers the active power mismatch and avoids MG instabilities. Similar to the controller of an inverter-based generator, the VFCSG uses diffusive averaging terms to mitigate the steady-state error in frequency regulation. Note that voltage-based controller and IPS gains stabilize SGs in load perturbations, while inverter-based generators use only IPS gains for generator stability. This approach is the same as voltage-based frequency controller (VFC) presented in [31].

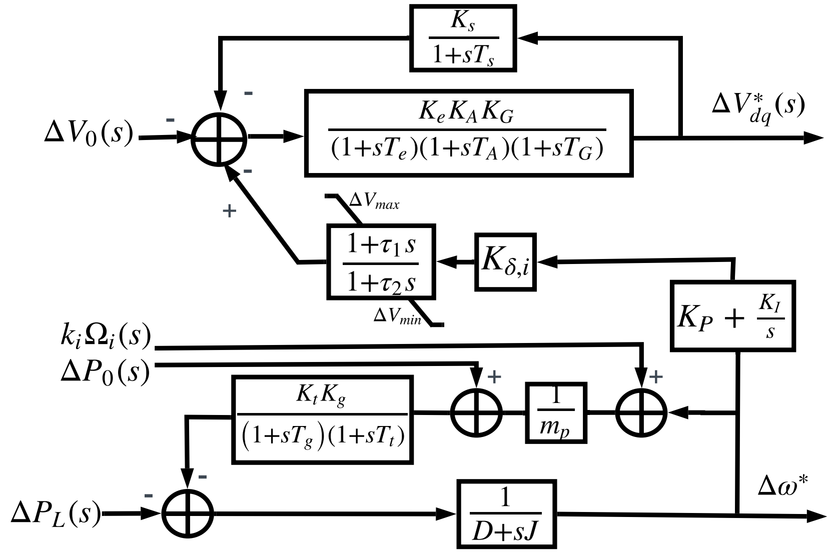

Figure 3.8: VFCSG model for the i^{th} SG [31, 34].

3.2 Small-Perturbation Stability

A small-perturbation model is carried out using eigenvalue analysis by linearizing the islanded MG. Although this approach is only valid around operating points, it presents the necessity condition for MG stability. To analyze the eigenvalue study, a small-signal model of a whole MG is obtained at a specific operation point. MG state-space model is divided into three state-space sub-modules: the generator, network, and load. From Figure 3.9, individual inverter and SG models are established for the IPS control approach, and then combined to create the comprehensive generator state-space model. Finally, the combination of generator, network, and load state-space models obtains an MG state-space matrix. General representations of state-space models for inverter-based DG, SG, network,

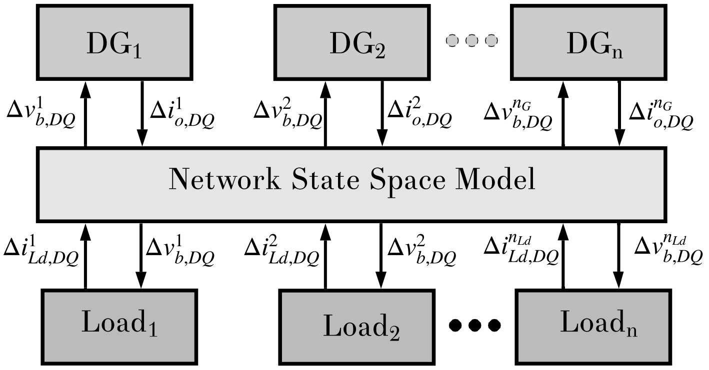

Figure 3.9: Block diagram of complete small-signal state-space model of MG.

and load sub-modules are written as follows:

$$\begin{aligned} \Delta\dot{x} &= A^{(g)}\Delta x + B^{(g)}\Delta u_x \\ \Delta y &= C^{(g)}\Delta x + C_y^{(g)}\Delta u_y, \qquad g \in \{INV, SG, Ld, Ln\} \end{aligned} \tag{3.11}$$

where $[\Delta y]$ is the output vector, and $[\Delta x]$ is the state vector of mentioned sub-modules.

3.2.1 State-Space Model of Individual Voltage Source Inverter

Voltage source inverter consists of power, voltage, and current controllers, an LCL filter, and a coupling inductance [76]. Voltage and current notations on d and q axis are defined as follow:

$$x_{s,dq} = [x_{s,d} \quad x_{s,q}]^T, \quad x \in \{v, i\}, \quad s \in \{o, l\}. \tag{3.12}$$

To connect an inverter to the MG, output variables $x_{s,qd}$ need to be converted to the common reference coordinates (DQ). Axis set (DQ) is the common reference frame rotating at frequency ω_{com}, whereas (dq_i) and (dq_j) are the reference frames of the i^{th} and j^{th} inverters at ω_i and ω_j, respectively [58]. Reverse transformation $(DQ \to dq)$ of x_s and inverter angle δ are given by

$$x_{s,dq} = T_{dq}^{-1} x_{s,DQ} + T_{\delta^{-1}}\delta,$$

$$T_{dq}^{-1} = \begin{bmatrix} cos(\delta_i) & sin(\delta_i) \\ -sin(\delta_i) & cos(\delta_i) \end{bmatrix},$$

$$T_{\delta^{-1}} = \begin{bmatrix} -x_{s,D}sin(\delta_i) + x_{s,Q}cos(\delta_i) \\ -x_{s,D}cos(\delta_i) - x_{s,Q}sin(\delta_i) \end{bmatrix}. \tag{3.13a}$$

Based on inverter model presented in Chapter 2, state-space model of an individual inverter can be written as

$$\begin{bmatrix} \Delta\dot{\theta} \\ \Delta\dot{P} \\ \Delta\dot{Q} \\ \Delta\dot{S}_v \end{bmatrix} = A^{(p)} \begin{bmatrix} \Delta\theta \\ \Delta P \\ \Delta Q \\ \Delta S_v \end{bmatrix} + B^{(p)} \begin{bmatrix} \Delta i_{l,dq} \\ \Delta v_{o,dq} \\ \Delta i_{o,dq} \end{bmatrix} + B^{(p)}_{\omega_{com}} \Delta\omega_{com} \tag{3.14a}$$

$$\begin{bmatrix} \Delta\omega \\ \Delta v^*_{o,dq} \end{bmatrix} = \begin{bmatrix} C^{(p)}_{\delta} \\ C^{(p)}_{PQ} \end{bmatrix} \begin{bmatrix} \Delta\theta \\ \Delta P \\ \Delta Q \\ \Delta S_v \end{bmatrix}, \tag{3.14b}$$

$$A^{(p)} = \begin{bmatrix} K & -m_p & 0 & 0 \\ 0 & -\omega_c & 0 & 0 \\ 0 & 0 & -\omega_c & 0 \\ 0 & 0 & 0 & 0 \end{bmatrix}, \tag{3.14c}$$

$$C^{(p)}_{PQ} = \begin{bmatrix} 0 & 0 & -n_q & -\kappa\beta \\ 0 & 0 & 0 & 0 \end{bmatrix}, \tag{3.14d}$$

$$B^{(p)} = \begin{bmatrix} 0 & 0 & 0 & 0 & 0 & 0 \\ 0 & 0 & \omega_c I_{o,d} & -\omega_c I_{o,q} & \omega_c V_{o,d} & \omega_c V_{o,q} \\ 0 & 0 & \omega_c I_{o,q} & -\omega_c I_{o,d} & \omega_c V_{o,q} & \omega_c V_{o,d} \\ 0 & 0 & 1 & 0 & 0 & 0 \end{bmatrix}, \tag{3.14e}$$

$$C^{(p)}_{\delta} = \begin{bmatrix} 0 & -m_p & 0 & 0 \end{bmatrix}, \tag{3.14f}$$

$$B^{(p)}_{\omega_{com}} = \begin{bmatrix} -1 & 0 & 0 & 0 \end{bmatrix}^T, \tag{3.14g}$$

where S_v is used to handle an integral over voltage magnitude. We denote a difference between an individual inverter reference and common reference frame, $\Delta\omega_{com}$, by

$$\Delta\theta_{com} = \int (\Delta\omega - \Delta\omega_{com})dt. \tag{3.15}$$

Generally, a PID control is used for both voltage and current controllers to change the line current magnitude flowing the coupling inductance. This current change affects the reference voltage of an inverter $v_{i,dq}$ by utilizing slack variables γ_{dq} and v_{dq} calculated by the integral over reference signals from power and voltage controllers. The virtual impedance $r_v + jX_v$ is added to the current controller to regulate output voltage. Under the virtual impedance paradigm, algebraic equations for the current controller are given by

$$v_{i,d}^{new} = -r_v i_{l,d} + X_v i_{l,q} + v_{i,d}^{old}, \tag{3.16a}$$
$$v_{i,q}^{new} = -r_v i_{l,q} - X_v i_{l,d} + v_{i,q}^{old}. \tag{3.16b}$$

State-space models for the voltage and current controllers and LCL filter are given in Appendix A [76]. A complete model of an individual inverter can be achieved by combining the state-space model of the power controller, voltage and current controllers, and LCL filter (See Appendix A). In total, there are 14 state variables, 3 inputs, and 2 outputs in each inverter model [58]:

$$\Delta\dot{x}^{(INV)} = A^{(INV)}\Delta x^{(INV)} + B^{(INV)}\Delta v_{b,DQ}^{(INV)} + B_{\omega_{com}}^{(INV)}\Delta\omega_{com} \tag{3.17a}$$

$$\begin{bmatrix} \Delta\omega^{(INV)} \\ \Delta i_{o,DQ}^{(INV)} \end{bmatrix} = \begin{bmatrix} C_{\omega}^{(INV)} \\ C_{i_{o,DQ}}^{(INV)} \end{bmatrix} \Delta x^{(INV)}, \tag{3.17b}$$

where the state variables are defined as follows:

$$\begin{aligned} \Delta x^{(INV)} = [&\Delta\delta^{(INV)}\ \Delta P^{(INV)}\ \Delta Q^{(INV)}\ \Delta S_v^{(INV)} \\ &\Delta v_{dq}^{(INV)}\ \Delta\gamma_{dq}^{(INV)}\ \Delta i_{l,dq}^{(INV)}\ \Delta v_{o,dq}^{(INV)}\ \Delta i_{o,dq}^{(INV)}]^T. \end{aligned} \tag{3.18}$$

3.2.2 State-Space Model of Individual SG

The SG model consists of stator and rotor windings, exciter, governor, turbine, and AVR, which have been modelled in Chapter 2. A full explanation of the SG model is presented in Appendix A [77, 78].

3.2.3 State-Space Model of Lines and Loads

The islanded MG has the different types of loads categorized as passive and active. Passive loads are classified as resistive loads (R-type), impedance loads (RL-type), and constant power loads (PQ-type). Active loads are defined only as inverter-interfaced load, and modelled similar to the inverter-based generator. The voltage dependent load presented in Chapter 2 is modeled in this section. The small-signal model of lines Ln and passive loads Ld is given by

$$\Delta\dot{i}_{x,DQ} = A^{(x)}\Delta i_{x,DQ} + B^{(x)}_{v_{b,DQ}}\Delta v_{b,DQ} + B^{(x)}_{\omega}\Delta\omega, \qquad x \in \{Ld, Ln\} \tag{3.19}$$

where $v_{b,DQ}$ and $i_{x,DQ}$ are output voltage and current flowing from lines and into loads, respectively. All matrices are given in Appendix A [58, 76].

3.2.4 Complete Model of the Islanded MG

Line and load models are presented in Appendix A. A comprehensive model of the islanded MG can be obtained by combining state-space models of generators, network, and loads through mapping matrices. These matrices connect output currents of generators or loads to nodes. Assume that the bus in islanded MG is a node; then, generators and load exchange current through that node. To model output voltage, a virtual resistor is assumed between each node and ground. This resistor is sufficiently large to have minimum influence on MG stability [76]. Hence, output voltage of the islanded MG with n_G generators connected together via n_{Ln} lines to meet requirement of n_{Ld} loads is given by

$$\Delta v_{b,DQ} = R_N\big(M_{INV}\Delta i_{o,DQ} + M_{SG}\Delta i_{o,DQ} - M_{Ld}\Delta i_{Ld,DQ} + M_{Ln}\Delta i_{Ln,DQ}\big). \tag{3.20}$$

Complete state-space model of the islanded MG is given by

$$\begin{bmatrix} \Delta\dot{x}^{(G)} \\ \Delta\dot{i}_{Ln,DQ} \\ \Delta\dot{i}_{Ld,DQ} \end{bmatrix} = A^{(MG)} \begin{bmatrix} \Delta x^{(G)} \\ \Delta i_{Ln,DQ} \\ \Delta i_{Ld,DQ} \end{bmatrix} \tag{3.21a}$$

$$\Delta x^{(G)} = \begin{bmatrix} \Delta x^{(INV)} \\ \Delta x^{(SG)} \end{bmatrix}, \tag{3.21b}$$

where $A^{(MG)}$ is given in (3.22a).

$$A^{(MG)} = \begin{bmatrix} A^{(G)} + B^{(G)} R_N M_G C^{(G)} & B^{(G)} R_N M_{Ln} & B^{(G)} R_N M_{Ld} \\ B^{(Ln)}_{v_{b,DQ}} R_N M_G C^{(G)} + B^{(Ln)}_{\omega} C^{(G)}_{\omega} & A^{(Ln)} + B^{(Ln)}_{v_{b,DQ}} R_N M_{Ln} & B^{(Ln)}_{v_{b,DQ}} R_N M_{Ld} \\ B^{(Ld)}_{v_{b,DQ}} R_N M_G C^{(G)} + B^{(Ld)}_{\omega} C^{(G)}_{\omega} & B^{(Ld)}_{v_{b,DQ}} R_N M_{Ln} & A^{(Ld)} + B^{(Ld)}_{v_{b,DQ}} R_N M_{Ld} \end{bmatrix} \tag{3.22a}$$

$$X^{(G)} = \begin{bmatrix} X^{(INV)} \\ X^{(SG)} \end{bmatrix}, \qquad X \in \{A, B, C, C_\omega\}$$

$$R_N = \begin{cases} r_N, & i = j \\ 0, & i \neq j \end{cases}, \tag{3.22b}$$

$$M_G(i,j) = \begin{cases} +1, & G_j \rightarrow \text{node}_i \\ 0, & \text{o.w.} \end{cases}, \tag{3.22c}$$

$$M_{Ld}(i,j) = \begin{cases} -1, & Ld_j \rightarrow \text{node}_i \\ 0, & \text{o.w.} \end{cases}, \tag{3.22d}$$

$$M_{Ln}(i,j) = \begin{cases} -1, & i_{Ln_{(j,i)}} < 0, Ln_j \rightarrow \text{node}_i \\ +1, & i_{Ln_{(j,i)}} > 0, Ln_j \rightarrow \text{node}_i \\ 0, & \text{o.w.} \end{cases} \tag{3.22e}$$

MG stability is reflected by the eigenvalues of matrix, $A^{(MG)}$, which are determined by a characteristic equation $\Delta(\lambda)$:

$$\Delta(\lambda(k,\kappa)) = \lambda I_0 - A^{(MG)}, \tag{3.23a}$$

$$\det \Delta(\lambda(k,\kappa)) = 0. \tag{3.23b}$$

Eigenvalues are often referred to as modes, and reveal different frequency components in the islanded MG. Given $\Delta x^{(G)}$, descriptor system is stable if all roots in (3.23a) are in the open left-hand plane. Figure 3.10 summarizes the IPS approach used to share active and reactive power while maintaining frequency and voltage regulation. The IPS approach guarantees MG stability with changing of the frequency and voltage controller gains. Care should be taken to tune these controller gains so as to ensure that overall MG stability margin exceeds the minimum threshold $\underline{S_m}$. Otherwise, the IPS approach sheds some loads when these gains are not effective. The stability index, S_m, represents the stability margin loss and improvement due to any change in effective parameters or loading operating point. Ψ_0 and Ψ_j are defined as the stability margin in base and load condition when the j^{th} controller gain is changed, given by

$$\Psi = \arg\max_{\lambda} \mathbb{R}(\lambda(k, \kappa, n_p, m_p)), \tag{3.24a}$$

$$S_m = \frac{\Psi_j}{\Psi_0} \times 100\,\%. \tag{3.24b}$$

In general, the IPS parameters are much dependent on the stability margin threshold. The relation between changes in IPS parameters and MG stability determines the number of iterations. Note that a sensitivity analysis determines dominant eigenvalue corresponded to controllers of each generation unit. Therefore, frequency instability happens when one dominant eigenvalue corresponded to a generation unit moves to right-side of root locus coordination.

3.3 Numerical Results

To validate the effectiveness of the proposed IPS controller for an islanded MG, a modified CIGRE benchmark for a medium voltage network is implemented in MATLAB/SIMULINK. A general schematic of the CIGRE test case is shown in Figure 3.11 [31]. This European medium-voltage benchmark features the total installed DG capacity of 3.5 MVA. The total load in the system is 2 MVA which consists of 60% constant impedance, 30% constant current, and 10% constant power loads, i.e., $k_p = k_q = 1.5$. The MG includes three diesel-based SGs connected to buses #1 and #3, one wind turbine (WT) in bus #11, and one ESS in bus #6. The total rating power of SGs in bus #1 is 1200 kVA, and an SG in bus #3 has the maximum nominal power of 1000 kVA.

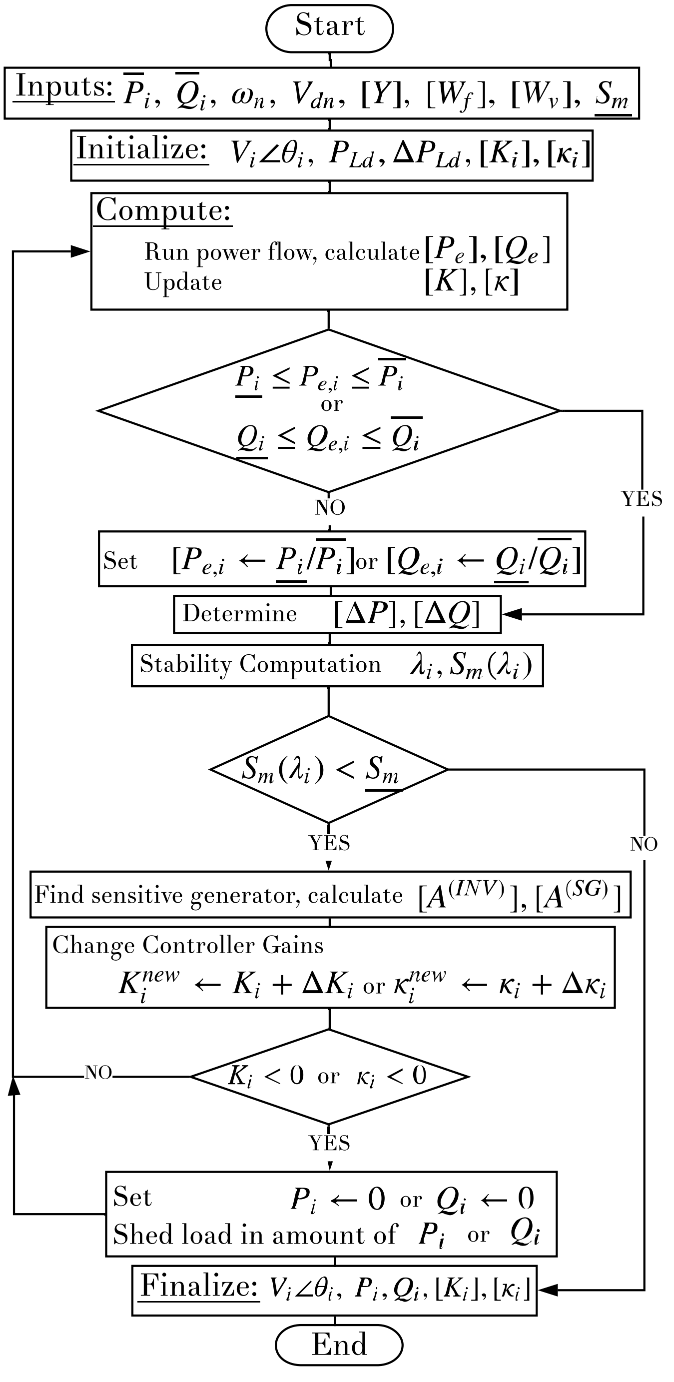

Figure 3.10: Flowchart of the proposed IPS scheme.

The WT is a three blade HW43 with rated power of 600 kW and SG model type. The rated wind speed of WT is 14.5 m/s [79]. The ESS in bus #6 has a maximum power rating of 825 kW and a capacity of 6000 kWh. It is connected to the AC link through a bidirectional voltage source inverter. Acceptable minimum SOC of ESS is 600 kWh. In this test case, we consider one ESS and three diesel-based SGs to highlight the effect of IPS model on output power of a single ESS. Note that consideration of one ESS emphasizes the impact of IPS on power sharing when the ESS is close to its rated power. However, the proposed IPS discussed in this chapter does not depend on the number of ESSs; thus, it is expected that this control technique would demonstrate similar performance in more realistic test systems. The multi-master control technique is applied on MG operation due to contribution of all controllable units in power sharing approach. Feeders are connected together via 14 coupled π sections. The MG is assumed to be a resistance dominated network. A detailed description of the test system and parameters is provided in Appendix B [9]. The communication network topology is fully-connected for both frequency and voltage control. Therefore, the communication weight between LCs i and j is chosen as $a_{ij} = 1$ and $b_{ij} = 1$ in W_f and W_v, respectively.

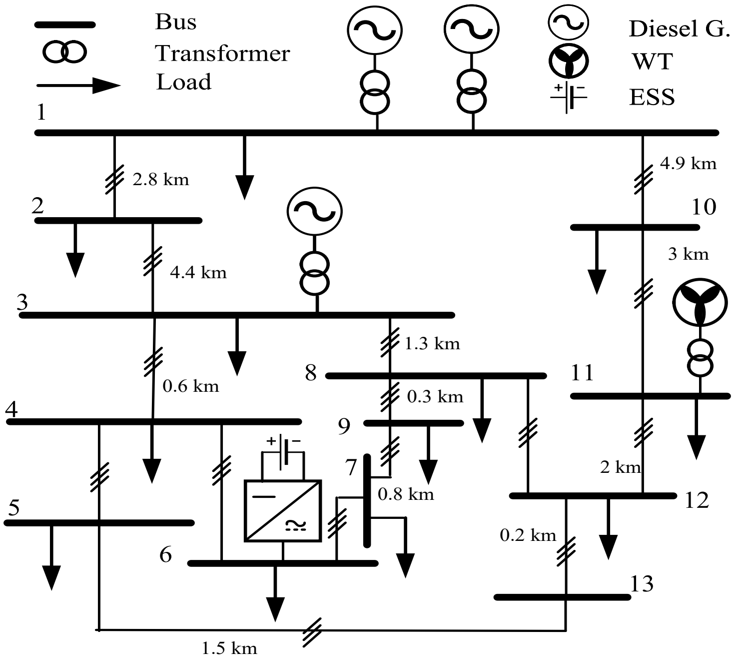

Figure 3.11: 14-bus modified CIGRE benchmark of islanded MG [31].

For the initial values of VFCSG, we test different values for time-constants τ_1 and τ_2; the best performance is obtained from trial and error method at 0.015 s and 0.75 s, respectively. Trial and error test on VFCSG gain indicates that, by increasing K_δ, the MG damping metric increases until it reaches a certain point where any further increment of K_δ deteriorates the overall MG damping. Observe that $K_\delta = 1.5$ results in the best stability margin and MG damping; thus, we choose this value as the VFCSG gain for time-domain simulation studies. This section is organized into four studies, starting with characterization of the IPS control performance, and examining the IPS control robustness under wind fluctuations, disconnection of generation units, and plug and play functionality.

3.3.1 Critical Eigenvalues versus IPS Controller Parameters

Dominant eigenvalues are analyzed to evaluate the IPS impact on the MG's small-perturbation stability. These eigenvalues are determined from the procedure outlined in (3.22a)-(3.23a). Trajectory of dominant eigenvalues in the IPS approach is compared with that in the conventional frequency droop controller (Base) under various controller gains. Note that the conventional droop controller is designed according to the direct relationship between frequency and active power or voltage and reactive power. It is chosen as base approach because of its superiority in stable power sharing over other approaches such as angle-based algorithm. We assume that the initial MG parameters are obtained from steady-state operating conditions in MATLAB/SIMULINK.

A stability sensitivity index is defined to evaluate MG stability in response to frequency and voltage controller gains $[K, \kappa, m_p, n_p]$. Generally, this is a manifestation of IPS robustness, in which the dominant eigenvalue λ changes according to the j^{th} controller gain x_j by $\partial\lambda/\partial x_j$. From Table 3.2, it can be seen that the dominant eigenvalue is more sensitive to frequency and voltage control parameters in the base approach when compared to IPS gains. Increasing either feedback gains m_p or n_p to share active or reactive power results in an increasingly dominant eigenvalue change. Observe that the IPS controller is capable of providing same power sharing with 50% improvement in the stability sensitivity index. Figure 3.12 compares the impact of the controller gains in the IPS approach, K, κ, with base model, m_p, n_p, on the MG transient performance. To do this, loads on all buses are changed at intervals around steady-state equilibrium. In the base approach, droop gains are changed to maintain uniform power sharing among generation units. Note that generation units with lower droop gains contribute more in the load changes. As depicted in

Figure 3.12, the dominant eigenvalues are strongly associated with frequency control dynamics, while overall damping of MG is dependent on eigenvalues of the voltage controller. From Figure 3.12, it can be seen that as m_p decreases, dominant eigenvalue reaches a point whereas for further increase in gain, the MG cannot remain in stable region. Decreasing m_p of a single generator by less than half of initial droop gain (m_{p0}), dominant modes in the system are forced to the right side of root-locus coordination. By the same convention, continuing the change of voltage droop gain (n_p), dominant eigenvalues move to the right side of root-locus coordination, leading to MG instability.

As observed in Figure 3.12, the corresponding IPS controller gains for frequency (K) and voltage (κ) are changed to achieve power sharing similar to the base approach. Increasing K and κ has effects nearly identical to decreasing m_p and n_p on power sharing among generation units, respectively. Traces of eigenvalues prove the robustness of IPS controller gains in response to load changes. Note that the IPS controller preserves MG stability even though the droop gain change causes instability when performing in the same operational mode.

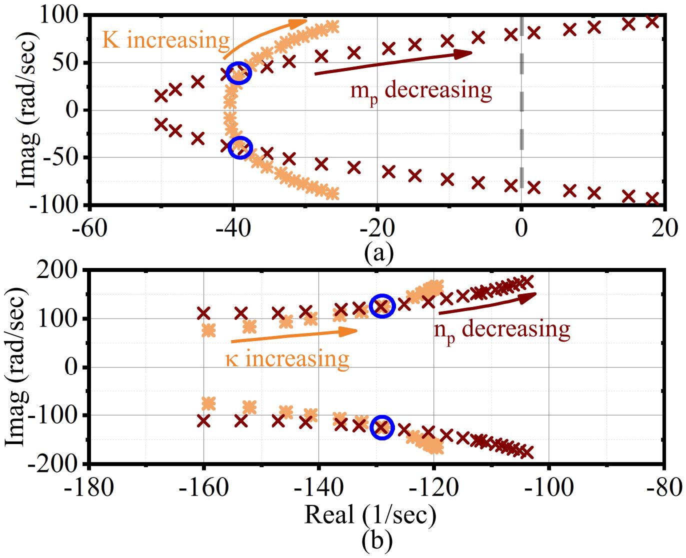

Figure 3.12: Traces of eigenvalues as a function of base controller and corresponding IPS gains for (a) active power: $0.5m_{p0} \leq m_p \leq 2m_{p0}$, $0.8K_0 \leq K \leq 1.6K_0$; (b) reactive power: $0.5n_{p0} \leq n_p \leq 32n_{p0}$, $0.75\kappa_0 \leq \kappa \leq 2.5\kappa_0$. Blue circle indicates the steady-state operation.

In the base approach, S_m changes from 112% at $2m_{p0}$ to -85% (negative sign due to being in an unstable region) at $0.5m_{p0}$. To have the same power sharing behaviour, the proposed IPS changes S_m from 104% at $0.8K_0$ to 80% at $1.6K_0$, thus demonstrating more robustness in frequency regulation than the base controller.

To better evaluate effectiveness of the IPS on voltage regulation, κ is changed from 0.75 to 2.5, while n_p changes from 32 to 0.5 times of nominal value n_{p0}. Note that a small droop gain is essential to improve transient response of generation units and share power among them. This small droop gain reduces stability margin with growth of load, and increases reactive power sharing error to nominal values. As under the frequency control, the base model varies S_m from 125% in value of $32n_{p0}$ to 106% for $0.5n_{p0}$, whereas the IPS forces S_m from 124% at $0.75\kappa_0$ to 113% at $2.5\kappa_0$.

Table 3.2: Dominant eigenvalue sensitivity

	Frequency	Voltage
Base	$\partial\lambda/\partial m_p : 4.6$	$\partial\lambda/\partial n_p : 2.4$
IPS	$\partial\lambda/\partial k : 2.1$	$\partial\lambda/\partial\kappa : 1.6$

3.3.2 IPS Performance in Renewable Power Fluctuations (Scenario 1)

Effectiveness of the IPS during renewable energy fluctuations is evaluated by comparing the MG response to wind power variations in three different techniques:

- Base model: It is called the conventional droop controller. In the frequency controller, it uses a linear relationship between frequency and active power. Same convention is applied on voltage droop controller (i.e., linear relationship between voltage and reactive power).
- VFC model: This technique uses a voltage-based frequency controller as discussed in Subsection 3.1.5. This controller is fully explained in [31].
- IPS model

The WT power fluctuates between 15% and 65% of 800 kVA [9]. Figure 3.13 shows the MG frequency dynamics for three cases. First, considering frequency dynamics in Figure

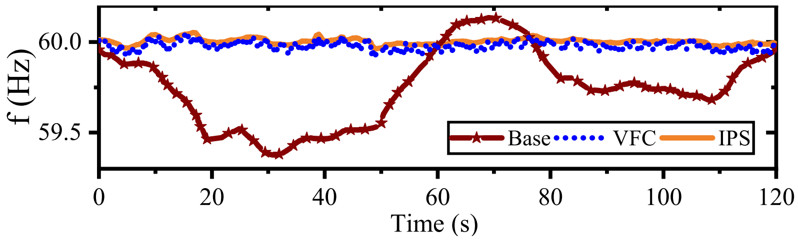

Figure 3.13: Frequency response for base, VFC, and IPS models in variation of WT power.

3.13, frequency deviation experienced under the IPS approach is quickly eliminated by distributed controller gains. This approach causes frequency regulation to be maintained throughout wind fluctuation with minimal transients. Note that IPS approach uses the advantage of VFC as presented in Subsection 3.1.5; hence, frequency response of IPS model is similar to that of the VFC model.

It is noted that the ESS has a significant effect in compensating for wind variation, and that active power output of diesel-based SGs undergoes no significant changes. Figures 3.14 and 3.15 depict voltage profile of two buses in three approaches. Observe that voltage variations in the base controller are preserved within operating voltage range of 0.98-1.02 p.u., different from those under the IPS and VFC approaches with ±0.05 p.u. voltage error. It is noteworthy to mention that IPS utilizes the virtual impedances and distributed variables (Ω_i, e_i) to enhance voltage profiles comparing to those of VFC model. To elaborate on impact of Q-V compromise factor on voltage regulation, a sensitivity analysis is performed on β in Table 3.3. Increasing the feedback gain β results in increasingly voltage regulation on bus #3, and decreases reactive power sharing of diesel-based SG #3.

The ESS connected to bus #6 operates in unity power factor under the voltage source

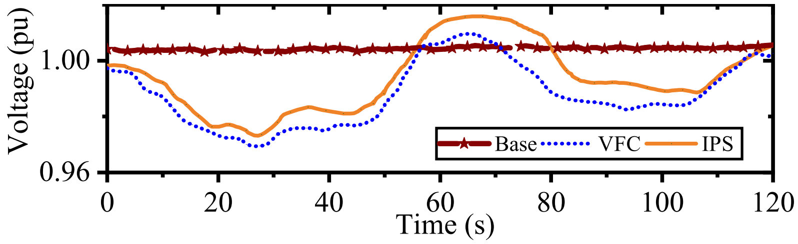

Figure 3.14: Voltage profile of bus# 1 in cases of base, VFC, and IPS controllers in variation of WT power.

control paradigm; the discharging and charging ramp-rate is 30 MW/Hz, which is an

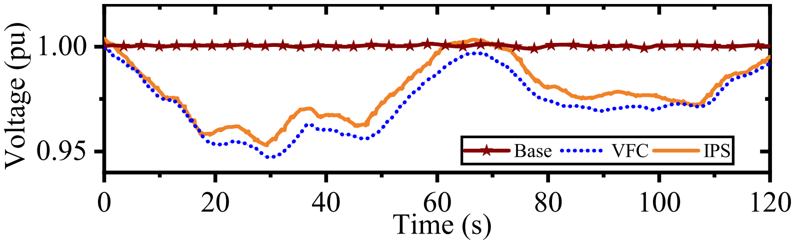

Figure 3.15: Voltage profile of bus# 3 in cases of base, VFC, and IPS controllers in variation of WT power.

Table 3.3: Reactive power sharing and voltage regulation on bus #3

	$\beta = 0$	$\beta = 0.5$	$\beta = 1$
Voltage (p.u.)	0.95	0.96	0.98
Reactive Power (kVAr)	430	417	395

approximately zero power-frequency droop. To better evaluate the IPS controller, a frequency and voltage droop for the ESS is considered. Figure 3.16 demonstrates that the diesel-based SGs make no contribution in the base approach, but have a significant commitment to generate active power in the IPS controller. It can be seen that VFC utilizes the diesel-based SGs less than IPS model due to lack of power sharing control.

Observe in Figure 3.17 that the ESS generates up to 800 kW of the active power and

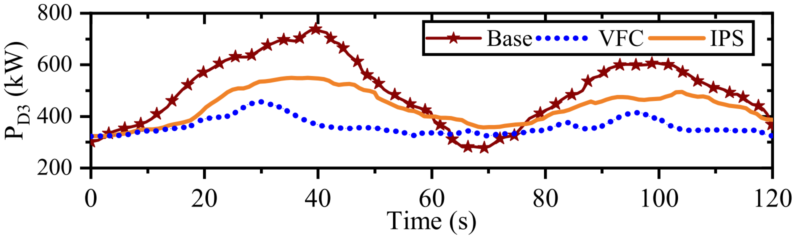

Figure 3.16: Active power output of diesel-based SG #3 due to wind power fluctuation.

40 kWh of total energy. When wind power continues fluctuating for an hour, sufficient ESS is needed to respond to the MG requirement. However, ESS implementation can be expensive, at normal prices, typically $5-12k per kWh [31]. Active power sharing is precisely shared among diesel-based SGs and battery throughout entire time-simulation. This power sharing behaviour is identical in all other studies, and hence reactive power shar-

ing plots are omitted due to space considerations. Note that ESS generates more power in case of VFC comparing to IPS model because there is no control on accurate power sharing.

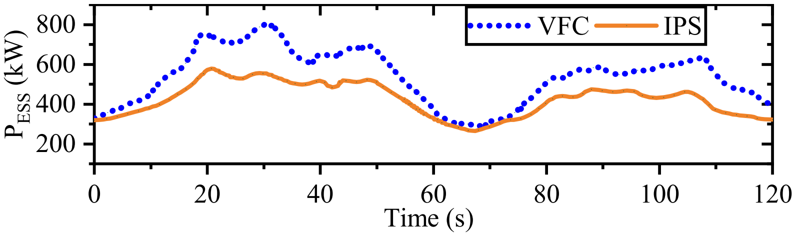

Figure 3.17: Active power output of ESS due to wind power fluctuation.

Additionally, the small frequency droop gain forces the ESS to dispatch significantly during the wind power fluctuations, whereas diesel-based SGs still have operating power capabilities to be dispatched. Figure 3.18 and 3.19 show operating power capability of diesel-based SG #3 and the ESS in three cases. In the VFC model, ESS reaches its rated power in $t =$[18 33]s, and there is no available power for future dispatch.

From Figure 3.18, the diesel-based SG #3 in VFC approach has no contribution in active power sharing at $t =$40s, whereas the MG utilizes the ESS power significantly. Observe that IPS is capable of enhancing active power contribution of diesel-based SG #3 from 22% to 30%, and decreasing it in ESS from 48% to 37%. The rest of power contribution belongs to diesel-based SG #1. Without loss of generality, the IPS controller dispatches active power among units to keep operating power capability for all generation units uniformly. Voltage control performance of the base model is highly dependent on voltage droop gain (n_p). Impact of n_p on the voltage is shown in Figure 3.20. As n_p decreases, voltage variations are shifted up to reach the nominal value. In addition, it can be concluded that adaptive virtual

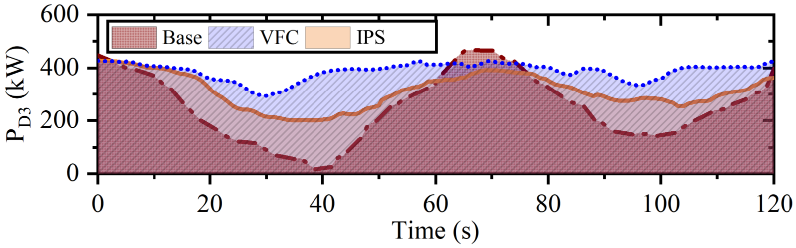

Figure 3.18: Operating power capability of diesel-based SG in wind power fluctuation.

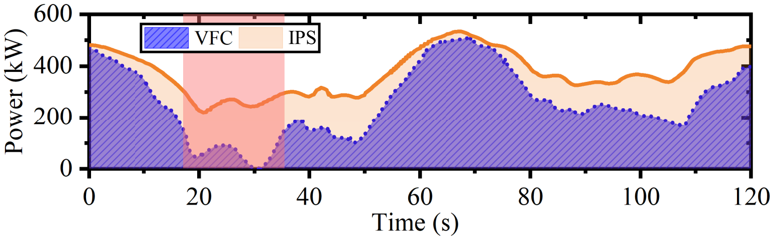

Figure 3.19: Operating power capability of ESS in wind power fluctuation.

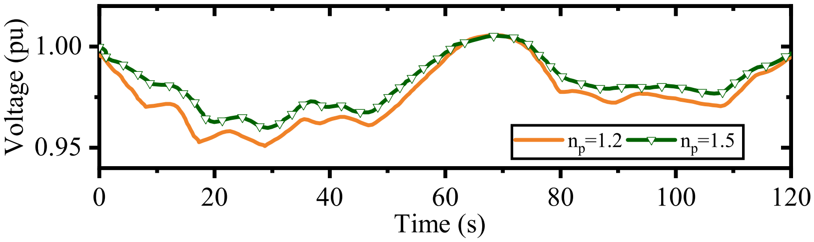

Figure 3.20: Voltage response of the system with different n_p in bus #3.

impedance improves voltage deviation of bus #6; thus, voltage regulation is maintained throughout wind power changes with minimal transients. As virtual impedance gain (f_{sv}) increases, voltage variations are shifted up to reach the nominal value. This increment of virtual impedance gain is effective on voltage regulation until reaching to a certain threshold ($f_{sv} = 0.25$). Any further increment in virtual impedance gain reduces the impedance connected to AC link; hence, it can cause MG instability. Output voltages on buses are regulated to their nominal values according to the integral-term in the IPS scheme and the implementation of virtual impedance. However, reactive power sharing has an error Q_{err} ($= (Q_i - Q_{i0})/Q_{i0}$) around 4.2% and -3.1% for diesel-based SGs #1 and #3, respectively. Table 3.4 lists power sharing among the ESS and diesel-based SGs under inhomogeneous IPS controller gains. Control parameters except the IPS parameters, are same as in Scenario 1. Note that these controller gains result in a varying transient frequency response, whereas MG stability is unchanged. Due to reactive characteristics of demand, load power changes from 462 kW to 443 kW. As illustrated in Table 3.4, increasing the IPS controller gain for diesel-based SG #1 changes the active power of that DG from 68 kW to 101 kW, while the ESS decreases its power contribution from 244 kW to 198 kW.

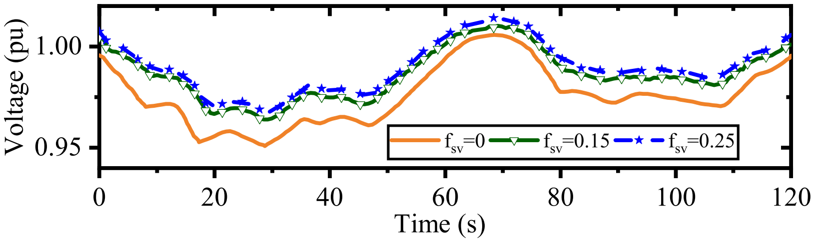

Figure 3.21: Effectiveness of adaptive virtual impedance implementation on output voltage.

Table 3.4: Impact of IPS controller gains on power sharing and frequency variation

IPS Gains	**Load (kW)**	**Frequency (Hz)**	**Power (kW)[PF]%**
K_{D1}, K_{D3}, K_{ESS}	ΔP_L	Δf	ΔP_{D1}, ΔP_{D3}, ΔP_{ESS}
1, 1, 1	462	0.00004	68, 150, 244 [14, 32, 54]%
1.01, 1, 0.99	458	0.00007	74, 149, 235 [16, 32, 52]%
1.02, 1, 0.98	456	0.00002	88, 147, 221 [19, 32, 49]%
1.03, 1, 0.97	452	0.0012	93, 146, 213 [21, 32, 47]%
1.1, 1, 0.9	443	0.002	101, 144, 198 [23, 33, 44]%

However, once ESS's PF in active power sharing reaches 44% from 54%, the IPS controller is not capable of regulating the MG frequency close to zero steady-state error.

The qualitative impacts of IPS controller gain on MG transient performance and steady-state equilibrium are summarized in Table 3.5. The IPS controller offers several advantages as well as accurate power sharing and frequency and voltage regulation. Two transient coefficients of the IPS controller reduce settling time of frequency and voltage regulation up to 20%. Observe that as these transient coefficients increase, the settling times reach certain points that for further increase in them, the settling times are unchanged. Note that voltage response of the MG with Q-V compromise factor is significantly improved with a steady-state voltage of around 0.98 p.u., whereas the reactive power sharing is not accurate.

3.3.3 IPS Performance in Disconnection of DGs (Scenario 2)

To better evaluate performance of the IPS during large disturbances, diesel-based SG #1 is disconnected at t =1 s. Prior to this disconnection, the MG is assumed to be in steady-state condition. For simplicity of analysis, instantaneous active power output of the

Table 3.5: Performance analysis in changing IPS controller gains for SG #3

Gains	**From**	**To**	**Analytical effect upon change**
K_3	$0.8K_0$	$1.6K_0$	Increases active power sharing, S_m: 104%→ 80%
κ_3	$0.75\kappa_0$	$2.5\kappa_0$	Increase reactive power sharing, S_m: 124%→ 113%
K_{tr}^{f}	0.5	1	Frequency regulation: t_{set}: 2.45 s→ 2 s
K_{tr}^{v}	0.5	1	Voltage regulation: t_{set}: 2.1 s→ 1.85 s
β_3	0.5	1	V_3: 0.97 p.u.→ 0.98 p.u., Q_{err}: 1.8%→2.4%

* The arrow (→) denotes gain change from initial value to final value.

wind turbine is considered to be constant during the disconnection. Figure 3.22 depicts frequency response for three different approaches, i.e., base, VFC, and IPS models. For the base model, frequency drops below 59.7 Hz after disconnection of DG, which is beyond the allowable frequency limit. Application of VFC improves steady-state frequency by around 59.9 Hz, whereas frequency remains within acceptable limits; therefore the MG does not need the load curtailment. The IPS controller restores frequency to nominal value with a slightly higher settling time as compared with the base model. Figure 3.23 illustrates corresponding active power of diesel-based SG #3 after the disturbance at t =1 s. The fast-acting characteristics of ESS do not allow the diesel-based SG to operate during disturbance in the base model; hence, ESS does not exceed the maximum rating power 800 kW and 2 kWh energy in exchange of loads. From Figure 3.24, it is observed that diesel-based SG #3 in VFC model has no significant change since ESS compensates for the disconnection of SG #1. The IPS controller releases operating power capability of ESS only 3 seconds after a disturbance; thus this controller forces diesel-based SG #3 to

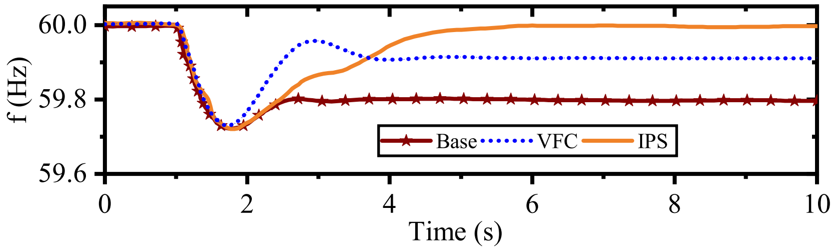

Figure 3.22: Frequency response of MG during disconnection of diesel-based SG #1.

generate about 440 kW more than that of VFC model. Figure 3.23 presents reactive power generated by diesel-based SG #3. Due to voltage drop on buses, reactive power generation of diesel-based SG #3 is decreased to 200 kVAr in the base approach. However, the IPS controller preserves voltage magnitudes within ± 0.05 p.u. voltage error.

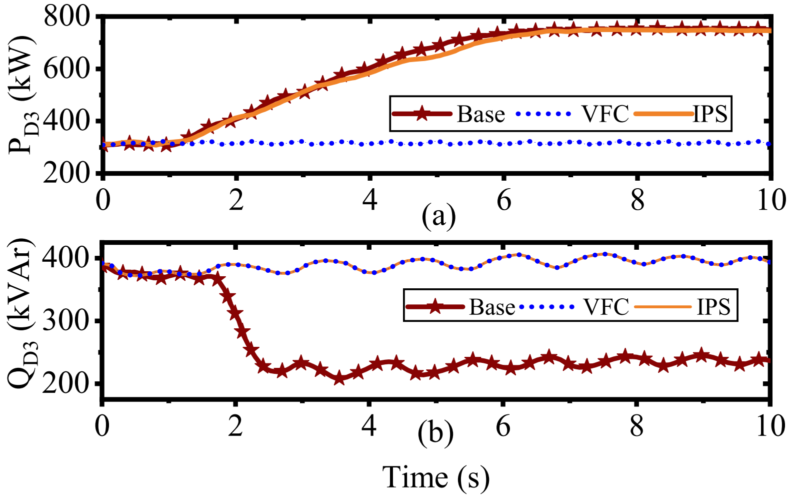

Figure 3.23: Active and reactive output power of diesel-based SG #3 in Scenario 2.

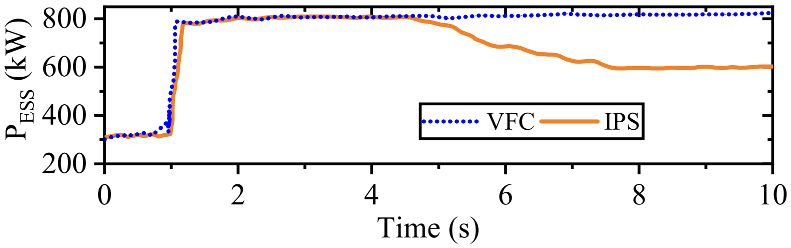

Figure 3.24: Active output power of ESS in Scenario 2.

3.3.4 Plug and Play Functionality of IPS Controller (Scenario 3)

The plug and play functionality is tested by disconnecting diesel-based SG #1 at $t =$ 20 s, and reconnecting at $t = 40$ s. A synchronization action is used in the downtime to synchronize SG #1 with the remaining islanded MG before re-connection. Control parameters are same as Scenario 1. Two frequency and voltage indexes are defined to

Table 3.6: IPS performance under plug and play operation of SG #1

	Base	VFC	IPS
Frequency (Hz)	59.79	59.98	59.99
Voltage (p.u)	0.99	0.97	0.98
ESS Utilization (kWh)	-	4.19	3.12

evaluate the IPS performance during this process. Table 3.6 shows that the IPS controller reduces frequency deviation, $\max\{|\Delta\omega(t)|\}$, during the plug and play functionality. In addition, it is concluded that the impact of this process on voltage deviation on bus #1, $\max\{|\Delta V_1(t)|\}$, is negligible for the base approach compared to the VFC and IPS models. The ESS utilization is reported on Table 3.6. Observe that using IPS controller, the ESS utilization decreases by 30%, and results in saving active energy of around 1.07 kWh for each plug and play functionality. Without loss of generality, the IPS controller maintains accurate power sharing as well as frequency and voltage regulation despite connection and disconnection of SG #1.

3.4 Summary

In this chapter, an IPS approach is proposed for islanded MGs. Based on the realistic analysis and the simulation results shown in this chapter, the IPS controller results in frequency and voltage regulation, while sharing power proportionally to generation units' operating power capabilities and their droop control values. The IPS controller gains can be tuned to achieve either voltage regulation, reactive power sharing, or a compromise between them. A mathematical model of small-perturbation stability is presented along with a performance analysis. By properly tuning changes in IPS parameters, it is demonstrated that the IPS controller provides zero steady-state errors in MG frequency, unlike conventional control models. This controller reduces the dependency on ESSs by distributing operating power capabilities of generation units over a wide time-horizon. Furthermore, the IPS controller decreases the impact of large disturbances on the MG, such as the disconnection of DGs and plug and play functionality. The IPS controller shows robust frequency and voltage control performance under small perturbations with minimal transients. A voltage based frequency controller for SG was also developed to maintain generator stability while reducing the impact of voltage-dependent loads on SG voltage.

Chapter 4

Dynamic Voltage and Frequency Controller

For any changes in load or renewable generation, n_{LC} LCs of dispatchable units are responsible for regulating frequency and voltage at the primary level. Then, unit commitment (UC), a working algorithm in MGCC, ensures a stable and optimal operation at the secondary control level. The UC problems are mainly formulated to achieve cost and ESS efficiency through frequency and voltage regulations. Generally, in conventional UC, scheduling of generation units remains fixed for the duration between two dispatch intervals; however, demand or renewable generation can continuously change. As shown in Figure 4.1, stair-pattern scheduling of generation units creates large frequency and voltage excursions at the edge of each dispatch interval. Furthermore, fixed scheduling is not efficient for either operation cost or ESS life-cycle, without addressing output renewable power variability and demand perturbations [9, 10]. In theory, it is commonly assumed that local frequency, voltage, and net demand during each dispatch interval are equal to the corresponding steady-state conditions; thus, a timescale separation happens between fast synchronization-enforcing primary and slower secondary controllers. In general, this timescale separation affects the power sharing properties and dynamic regulation of the MG frequency and voltage in the secondary control, specifically during rapid load and renewable energy perturbations [11].

The mid-level controller deals with impairments due to timescale difference between the fast synchronization-enforcing primary controller and slower secondary controller by optimizing IPS controller parameters. Figure 4.1 depicts the stair-pattern provision of mid-level and secondary controllers with dispatch time intervals T and M indexed by t and m, respectively. The uncovered actual net demand $P_L^m(t)$ in the mid-level control stair-pattern

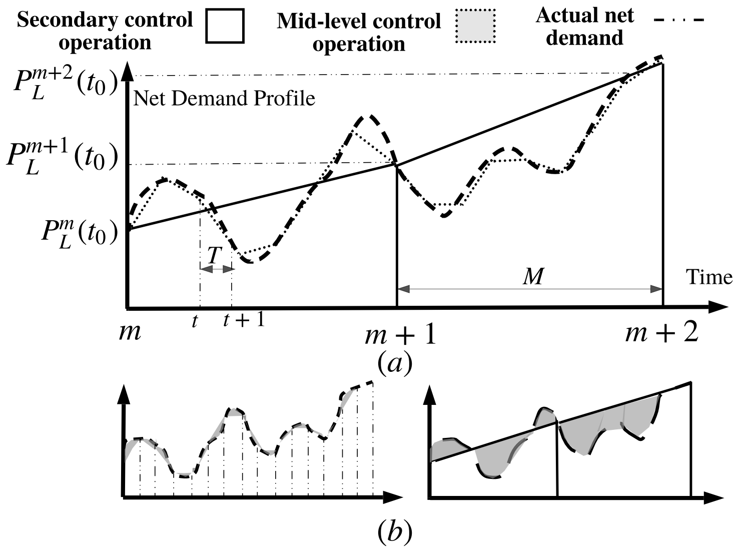

Figure 4.1: (a) Stair-pattern provision of net demand profile. (b) Net demand coverage of mid-level and secondary controllers.

is much less than that of the secondary controller, which demonstrates the importance of mid-level control operation. Note that power dispatch provision generated by both controllers follows a pattern which is not exactly stair-wise, because of smooth power fluctuation between two time intervals. In each time interval M, the secondary controller updates reference active and reactive power $P_i^m(t_0)/Q_i^m(t_0)$ by minimizing operating cost and ESS life-cycle degradation. In conventional UC, these reference power levels shift up or down the droop control curve at the primary level, resulting in new frequency and voltage droops. For a larger islanded MG with higher penetration of renewable units, more changes in active and reactive reference power may result in system frequency and voltage deviating from their acceptable ranges of operation. The mid-level controller divides each dispatch horizon M into n_T dispatch sub-intervals of duration T, and tunes droop control parameters to optimize MG operation. Finally, the primary controller regulates frequency and voltage by exchanging data on rated and operating active and reactive power levels $P_i^m(t)/Q_i^m(t)$ among neighboring controllable units in each dispatch sub-interval [17].

4.1 Mid-Level Frequency and Voltage Controller

As shown in Figure 4.1, net demand profile does not jump from $P_L^m(t)$ to $P_L^{m+1}(t)$ at m^{th} dispatch time interval, but gradually changes from $P_L^m(t)$ until it reaches $P_L^{m+1}(t)$ over the time duration M. Observe that the net demand changes must be addressed by real-time generation power based on realistic measurements at time sub-intervals of T. Dynamic programming is a powerful tool in solving optimization problems, particularly for complex non-linear MG operations. However, it is often computationally difficult to run feed-forward and backward numerical processes to solve an optimization problem specifically in the case of multi-objective MG control [56]. To circumvent this problem, a family of adaptive critic design is proposed by Werbos [80] as a new control technique that can approximate the optimal control signals. Adaptive dual heuristic dynamic programming (ADHDP) is developed to approximate the cost-to-go function, which consists of a model, action, and two critic neural networks (NNs). The basis model of ADHDP is achieved from [81], but design of ADHDP for multiple renewable resources in islanded MG has not yet reported. As shown in Figure 4.2, a two-critic ADHDP architecture is proposed to keep MG stability margin ($\psi^m(t)$) within an allowable range, and minimize operating cost and ESS life-cycle degradation ($U^m(t)$) with the measurements of available MG states ($s^m(t)$), the approximated system states ($\hat{s}^m(t)$), and action control variables ($a^m(t)$) at time t of duration T. The action vector consists of four action variable sets: coefficients ($k_i^m(t), \kappa_i^m(t)$) of the diffusive averaging droop controller, virtual impedances ($Z_{v,i}^m(t)$), and VFCSG gains ($K_{\delta,i}^m(t)$) [11] of the i^{th} generator. Seven MG states as network outputs, namely active and reactive power of generation and load units ($\Delta P_i^m(t), \Delta Q_i^m(t), \Delta P_{cl}^m(t), \Delta Q_{cl}^m(t)$), frequency and voltage deviation ($\Delta\omega_i^m(t), \Delta V_i^m(t)$), and SOC of storage ($S_j^m(t)$), are denoted by

$$a^m(t) = \left\{k_i^m(t), \kappa_i^m(t), Z_{v,i}^m(t), K_{\delta,i}^m(t)\right\}, \tag{4.1a}$$

$$s^m(t) = \left\{\Delta\omega_i^m(t), \Delta P_i^m(t), \Delta Q_i^m(t), \Delta P_{cl}^m(t), \Delta Q_{cl}^m(t), \Delta V_i^m(t), S_j^m(t)\right\},$$
$$\forall i \in \Lambda_G, j \in \mathcal{E}, t \in \{1, 2, .., n_T\}, m \in \{1, 2, .., n_M\}. \tag{4.1b}$$

The mathematical representation of the ADHDP model, including action variables, the MG actual and approximated states, errors of model ($e_{MN}^m(t)$), action ($e_{AN}^m(t)$), and critic ($e_{CN}^m(t)$) networks, is presented in Figure 4.3. Description of inputs and outputs for ADHDP model is presented in Table 4.1. The detail of algorithm is described as dynamic

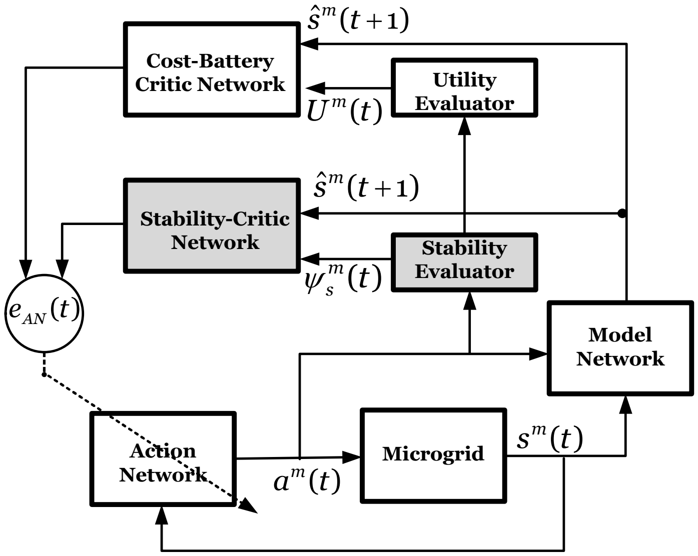

Figure 4.2: General layout for the ADHDP with two critic networks.

voltage and frequency controller (DVFC) in following subsections.

4.1.1 Model Network Design

An islanded MG is subject to perturbations such as load variations, leading to different operating conditions of generation units in current and future dispatch intervals. The model network mimics MG behaviours subject to current state and control actions, and predicts system's future states for cost and ESS efficient generation scheduling. The prediction engine can only be accurate if the difference $e^m_{MN}(t)$ between the one-step delay of model network output ($\hat{s}^m(t)$) and MG output ($s^m(t)$) is minimized. Therefore, the update rule for model network's parameters is achieved from minimizing of:

$$e^m_{MN}(t) = |\hat{s}^m(t) - s^m(t)|. \tag{4.2}$$

The network model prepares for the next step of estimated states, $\hat{s}^m(t+1)$, and derivatives of the estimated state at $(t+1)^{th}$ sub-interval with respect to action and actual state variables at t^{th} sub-interval, which is applied for training of critic networks. The model network consists of three layers: 1) an input layer with action vector ($a^m(t)$) and state vector ($s^m(t)$), 2) a hidden layer with 20 neurons, and 3) an output vector with next step

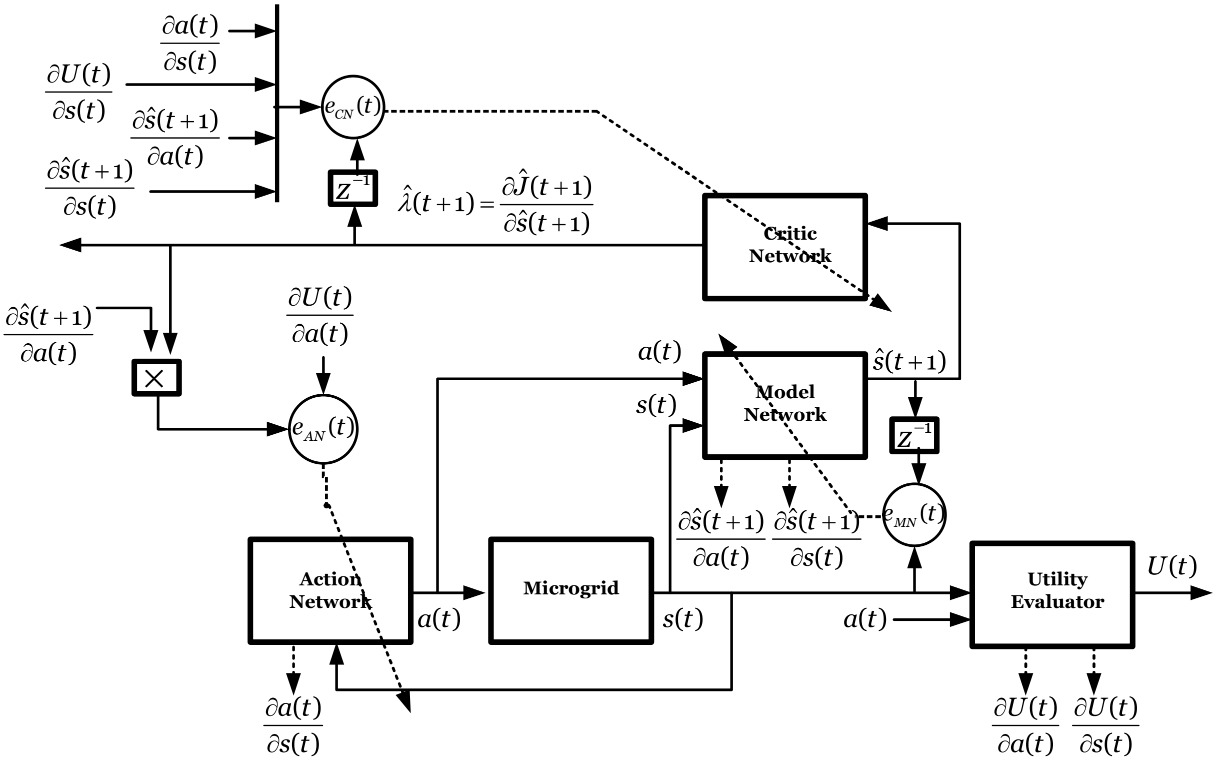

Figure 4.3: Detailed mathematical representation of the ADHDP: critic network, utility evaluator, action network, and model network (Note that all variables $x^m(t)$ are represented in the format of $x(t)$ to improve readability).

of estimated states ($\hat{s}^m(t+1)$) which represents future system responses.

4.1.2 Feed-Forward Critic Network Process

The generation units react to changes in net demand according to the IPS approach, but generation scheduling is not optimal when frequency and voltage controller parameters are constant for each dispatch interval. The main idea in the critic model is an approximation of objective functions, subject to control actions, and current and estimated states. Optimal strategy of the critic network is to minimize:

Table 4.1: Description of inputs and outputs for ADHDP

Network	**Input**	**Output**
Action	$\partial U(t)/\partial a(t)$: utility function to action vector $\hat{\lambda}(t+1)$: estimated derivative of cost-to-go function $\partial \hat{s}^m(t)/\partial a^m(t)$: estimated state to action vector	$a(t)$: action vector $\partial a(t)/\partial s(t)$: action to state vector
Model	$a(t)$: action vector $s(t)$: state vector	$\hat{s}(t+1)$: estimated state vector $\partial \hat{s}(t+1)/\partial a(t)$: estimated state to action vector $\partial \hat{s}(t+1)/\partial s(t)$: estimated state to state vector
Critic	$\hat{s}(t+1)$: estimated state vector $\partial a(t)/\partial s(t)$: action to state vector $\partial \hat{s}(t+1)/\partial a(t)$: estimated state to action vector $\partial \hat{s}(t+1)/\partial s(t)$: estimated state to state vector $\partial U(t)/\partial a(t)$: utility function to action vector	$\hat{\lambda}(t+1)$: estimated derivative of cost-to-go function
Utility	$a(t)$: action vector $s(t)$: state vector	$\partial U(t)/\partial a(t)$: utility function to action vector $\partial U(t)/\partial s(t)$: utility function to state vector

- Multi-objective operational cost-to-go function, $\mathcal{J}_u[a^m(t), s^m(t)]$, including operating cost of generation units, ESS life-time degradation, and MG frequency and voltage;
- MG stability margin cost-to-go function, $\mathcal{J}_s[a^m(t), s^m(t)]$,

subject to technical constraints. To keep MG stability within a desirable margin, stability critic network performs within an inner control loop of the operational critic network. The stability evaluator checks the DVFC stability index (SI) representing stability margin loss and improvement due to any change in effective parameters or loading operating point. Let ψ_0 and $\psi^m(t)$ denote the stability margins for a base and load condition when the j^{th}

controller is changed, at t^{th} sub-interval of m^{th} dispatch time, respectively. We have

$$\psi^m(t) = \arg\max_{\lambda} \mathbb{R}\big(\lambda[a^m(t), s^m(t)]\big), \tag{4.3a}$$

$$\mathrm{SI} = \frac{\psi^m(t)}{\psi_0} \times 100\,\%. \tag{4.3b}$$

Note that the real value of dominant eigenvalue is negative; hence, maximization of (5.33) forces dominant eigenvalue to the left-side of root locus coordination. The operational critic network loop, which acts more slowly than stability control loop, reduces impact of uncertainties on frequency and voltage control by minimizing the ESS life-cycle degradation and operating cost of generation units. The output power of generation units changes voltage $V_b^m(t)$ of the b^{th} bus and frequency $\omega^m(t)$ of MG. Frequency and voltage utility functions are given by

$$\Delta\mathcal{V}^m(t) = \sum_{b\in\mathcal{B}} \|\Delta V_b^m(t)\|^2, \tag{4.4a}$$

$$\Delta\mathcal{F}^m(t) = \|\Delta\omega^m(t)\|^2. \tag{4.4b}$$

Operating cost of the MG is achieved from a quadratic cost function. In the mid-level controller, change in operation cost of i^{th} unit is calculated based on change in output power $(\Delta P_i^m(t))$ around operating power $(P_i^m(t))$; hence, quadratic cost utility function, $\Delta\mathcal{C}^m(t)$, is given by:

$$\begin{aligned}\Delta\mathcal{C}^m(t) &= \sum_{i\in\Lambda_G}\Big(a_i(\Delta P_i^m(t) + P_i^m(t))^2 + b_i(\Delta P_i^m(t) + P_i^m(t)) + c_i + C_i^s y_i^m(t) + C_i^d z_i^m(t)\\ &\qquad - a_i(P_i^m(t))^2 - b_i P_i^m(t) - c_i\Big)\\ &= \sum_{i\in\Lambda_G}\Big((b_i + 2a_iP_i^m(t))\Delta P_i^m(t) + a_i(\Delta P_i^m(t))^2 + C_i^s y_i^m(t) + C_i^d z_i^m(t)\Big),\end{aligned} \tag{4.5}$$

where a_i ($\$/kWs^2$) and b_i ($\$/kWs$) are economic coefficients for the i^{th} SG generator, C_i^s/C_i^d and $y_i^m(t)/z_i^m(t)$ denote start-up/shut-down costs and corresponding binary variables. In conventional UC, fast-acting generation units need to respond to frequency change within a small time interval, which degrades the ESS life-cycle [82]. However, an ESS life-cycle utility function, $\Delta\mathcal{E}^m(t)$, keeps the amount of discharge depth between the minimum and maximum levels for SOC of the j^{th} ESS $(\underline{S_j}, \overline{S_j})$ by controlling $S_j^m(t)$, as follows [80]:

$$\Delta\mathcal{E}^m(t) = \sum_{j\in\mathcal{E}} \left(\exp\left(\frac{S_j^m(t)^2}{\overline{S_j}^2} - 1 \right) + \exp\left(\frac{\underline{S_j}^2}{S_j^m(t)^2} - 1 \right) \right). \tag{4.6}$$

Life-cycle of batteries depends on the value of discharge depth. Minimizing (4.6) increases the level of discharge depth by maintaining SOC between minimum and maximum levels. A weighted-sum method delineates a compromise energy dispatch among solutions achieved from utility functions. This method adjusts the importance of each utility function using scaling weight ($w_x \in [0,1], \forall x \in \{\mathcal{V}, \mathcal{F}, \mathcal{C}, \mathcal{E}\}$), where a higher scaling weight for a specific utility function represents a higher priority. The overall utility function is given by

$$U^m(t) = w_{\mathcal{V}}\Delta\mathcal{V}^m(t) + w_{\mathcal{F}}\Delta\mathcal{F}^m(t) + w_{\mathcal{C}}\Delta\mathcal{C}^m(t) + w_{\mathcal{E}}\Delta\mathcal{E}^m(t). \tag{4.7}$$

Optimal control problem is to generate power dispatch of generation units in t^{th} sub-interval by minimizing the cost-to-go operational function, $\mathcal{J}_u$, in the Bellman's equation of dynamic programming in a step-by-step way [81]. It also keeps MG stability margin within the desired range by maximizing cost-to-go stability function, $\mathcal{J}_s$. These functions are given by

$$\mathcal{J}_u(t) = \sum_{k=0}^{n_T} \gamma^k U^m(t+k), \tag{4.8a}$$

$$\mathcal{J}_s(t) = \sum_{k=0}^{n_T} \gamma^k \psi^m(t+k), \tag{4.8b}$$

where $\gamma \in (0,1]$ is the discount factor in dynamic programming. The technical constraints include the following:

1) Power balance: Different from conventional UC, the generation power and demand should be equal at each dispatch time, retrieved from (3.5);

2) DG units: These are certain constraints associated with DGs, such as an acceptable active and reactive power, and start-up and shut-down binary variables. For simplicity, we assume that the ramp-up power is equal to the ramp-down power (i.e., $R_i^u = R_i^d$), and have

$$u_i^m(t)\underline{x_i} \leq x_i^m(t) + \Delta x_i^m(t) \leq u_i^m(t)\overline{x_i}, \qquad \forall x \in \{P, Q\} \tag{4.9a}$$

$$y_i^m(t) \geq u_i^m(t) - u_i^m(t-1), \tag{4.9b}$$

$$z_i^m(t) \geq u_i^m(t-1) - u_i^m(t), \tag{4.9c}$$

$$|\Delta P_i^m(t)| \leq R_i^u T, \qquad \forall i \in \Lambda_G,\, t \in \{1, 2, .., n_T\} \tag{4.9d}$$

where $u_i^m(t)$ is a binary variable used to determine on/off status of DG;
3) Battery charge/discharge: The j^{th} ESS operates in three different modes, i.e., charging ($u_{c,j}^m(t) = 1, u_{d,j}^m(t) = 0$), discharging ($u_{c,j}^m(t) = 0, u_{d,j}^m(t) = 1$), and idle status ($u_{c,j}^m(t) = u_{d,j}^m(t) = 0$). The following set of constraints models SOC behaviours:

$$S_j^m(t) = S_j^m(t-1) + \Delta P_j^m(t) \cdot \frac{\eta_{c,j} \cdot u_{c,j}^m(t) - \dfrac{u_{d,j}^m(t)}{\eta_{d,j}}}{C_j} .T, \tag{4.10a}$$

$$\underline{S}_j \leq S_j^m(t) \leq \overline{S}_j, \tag{4.10b}$$

$$u_{c,j}^m(t) + u_{d,j}^m(t) \leq 1, \qquad \forall j \in \mathcal{E},\, t \in \{1, 2, .., n_T\} \tag{4.10c}$$

where $\eta_{c,j}$ and $\eta_{d,j}$ represent the efficiency of charging and discharging, and C_j is the ESS capacity.
The DVFC critic network is trained online to approximate the derivatives of estimated cost-to-go function, $\hat{\mathcal{J}}_u[a^m(t), \hat{s}^m(t)]$, with respect to the estimated state variable, $\hat{s}^m(t+1)$, of the model network called $\hat{\lambda}^m(t+1)$, and to minimize the critic network error $E_{CN}^m(t) = \|e_{CN}^m(t)\|^2$. Utility evaluator prepares derivatives of utility, $U(t)$, with respect to action and state variable. These inputs are used for calculating the critic network error. Here, $e_{CN}^m(t)$ is given by

$$\begin{aligned} e_{CN}^m(t) &= \frac{d\Big(\mathcal{J}_u(t) - \gamma \cdot \hat{\mathcal{J}}_u(t) - U^m(t)\Big)}{ds^m(t)} \\ &= \lambda^m(t) - \{\frac{\partial U^m(t)}{\partial s^m(t)} + \frac{\partial U^m(t)}{\partial a^m(t)} \cdot \frac{\partial a^m(t)}{\partial s^m(t)} \\ &\qquad + \gamma \cdot \hat{\lambda}^m(t+1)[\frac{\partial \hat{s}^m(t+1)}{\partial s^m(t)} + \frac{\partial \hat{s}^m(t+1)}{\partial a^m(t)} \cdot \frac{\partial a^m(t)}{\partial s^m(t)}]\}. \end{aligned} \tag{4.11}$$

Table 4.2: Typical convergence time for NNs

	Training Cycle	Model	Action	Critic
Time (s)	10 μ	150-250	<200	∼600

The same convection is applied to the stability critic network. The critic network consists of three layers: 1) an input layer with next step vector of states ($s^m(t)$), 2) a hidden layer with 20 neurons, and 3) an output vector with next step of estimated derivatives of cost-to-go function ($\hat{\lambda}^m(t+1)$) which trains action network.

4.1.3 Action Network Design

The action network determines optimum values for action variables (i.e., $k_i^m(t), \kappa_i^m(t), Z_{v,i}^m(t), K_{\delta,i}^m(t)$) by minimizing cost-to-go functions in critic networks. This network is trained online to approximate the optimal control law by minimizing the action network error (i.e., $E_{AN}^m(t) = \|e_{AN}^m(t)\|^2$), given by

$$\begin{aligned} e_{AN}^m(t) &= \frac{\partial \mathcal{J}_u(t)}{\partial a^m(t)} \\ &= \frac{\partial U^m(t)}{\partial a^m(t)} + \gamma \hat{\lambda}^m(t+1) \frac{\partial \hat{s}^m(t+1)}{\partial a^m(t)}, \end{aligned} \tag{4.12}$$

where partial derivatives are obtained from the model network, critic network, and utility evaluator as shown in Figure 4.3 [56]. Note that computational time of critic network training is much higher than that for the action and model network, but has less power to change the action variables from their desired values. The action network consists of three layers: 1) an input layer with estimated derivatives of cost-to-go function ($\hat{\lambda}^m(t)$), 2) a hidden layer with 20 neurons, and 3) an output vector with action variables ($a^m(t)$).

4.1.4 Design and Initialization of DVFC

Pre-training of three networks accelerates convergence of learning process. Thus, the model network, which approximates MG behaviour over a wide-operation range, is trained by the error of state variables. Table 4.2 lists the typical convergence time for each NN, performed by Intel(R) Core(TM) i7-8650 1.90GHz (4 processors). Note that computational

time for simulation greatly depends on hardware's capability. Pre-training for the critic network is done with results obtained from a mixed integer non-linear programming method in GAMS [83], is solved using an MINLP solver in the case of different generation and load perturbations. Pre-training should be performed for each test case using the cost-to-go function configuration. Online adaptation is performed sequentially for the model, action, and critic networks; when one network is being trained, the other networks are fixed (no weight updates). The feed-forward and backward training of action and critic networks continues until the critic and action errors converge to a specific range, such as $[-10^{-3}, 10^{-3}]$.
Once the ADHDP controller is initialized, it is plugged into the secondary controller and works according to the following procedure:

1. The action network receives the measured MG states, $s^m(t)$, and uses it to generate the action vector, $a^m(t)$, for real MG and model network;
2. The model network uses the action vector, $a^m(t)$, and state vector, $s^m(t)$, to generate next step of estimated state vector, $\hat{s}^m(t+1)$;
3. The critic network uses the action, $a^m(t)$, and estimated state vectors, $\hat{s}^m(t)$, to estimate cost-to-go functions $\mathcal{J}_u(t)$ and $\mathcal{J}_s(t)$;
4. The model network updates its weights according to (4.2) until the stop criterion is satisfied;
5. The critic network updates its weights according to (4.3a)-(4.11) until the stop criterion is satisfied;
6. The action network updates its weights according to (4.12) until the stop criterion is satisfied;
7. Above steps (1)-(6) are repeated in each training cycle until the end of the simulation.

4.2 Numerical Results

The proposed mid-level controller is tested on a modified CIGRE benchmark of medium-voltage network in MATLAB/SIMULINK. The diagram of the test system is shown in Figure 4.4. This European medium-voltage benchmark features total installed capacity of 3.6

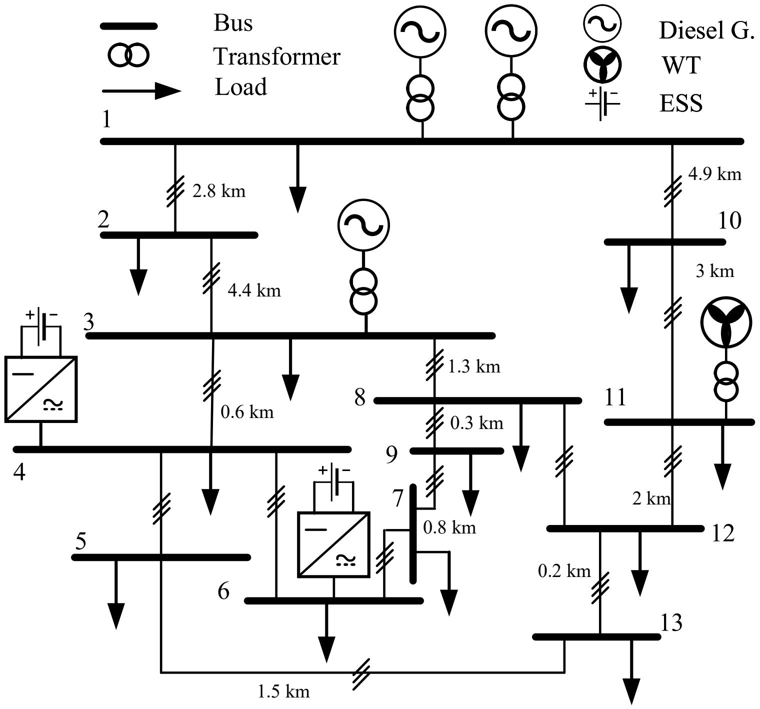

Figure 4.4: MG test case based on modified CIGRE benchmark [31].

MVA, and includes two diesel-based SGs connected to buses #1 and #3, one WT in buses #11, and two ESSs in buses #4 and #6. Different from test case in Figure 3.11, we add another ESS to bus #4 and change the capacity of generators to better analyze of optimal operation of MG. This assumption makes it easier to highlight the optimal performance of DVFC comparing to conventional UC. Generally, the conventional UC for islanded MGs is formulated as mixed integer non-linear programming problem as presented in [84]. The total load in the system is 2 MVA. We assume that load model consists of 100% constant power loads, i.e., $k_p = k_q = 0$. This assumption removes the dependency of power and voltage in load side. Therefore, it reduces the complexity of ADHDP algorithm due to simplicity in power flow equations. Subsequently, this assumption improves training time for three neural networks. Feeders are connected together via 14 coupled π sections. A detailed description of the test system and parameters is provided in [9]. The ESSs in buses #4 and #6 have a maximum power rating of 300 kW and energy rating of 6000 kWh, and are connected through bidirectional voltage source controllers. The acceptable

Table 4.3: Rating power and cost parameters for diesel-based SG [9]

Coefficients	D_1	D_2	D_3
$a_i(\$/kWh^2)$	0.00025	0.00015	0.0005
$b_i(\$/kWh)$	0.2876	0.2571	0.3476
$\overline{P}_i/\underline{P}_i(kW)$	800/60	600/50	800/80
$st_{i_{dg}}/sd_i(\$)$	15	7.35	10
$R_i^{up}(kW/s)$	200	150	150

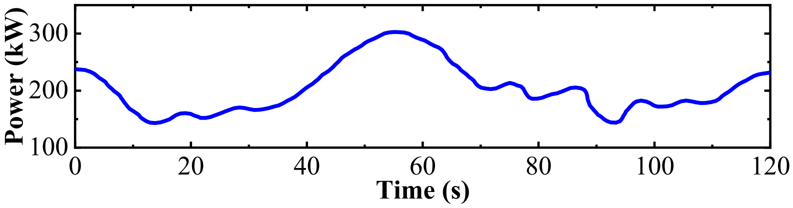

Figure 4.5: The measured wind turbine generation in bus #4 [9].

minimum SOC of ESS is 600 kWh. WT installed in bus #1 is a three blade HW43 with rated power of 600 kW and SG model type. The rated wind speed of the WT is 14.5 m/s [79]. The nominal rating, operating cost coefficients, start-up/down cost, and ramp rate are given in [9].

The SGs connected to buses #1 and #3 are in charge of voltage regulation using the proposed VFCSG; hence, diesel-based SGs and ESSs correspond to a master control of reactive power sharing, while WT acts as the slave control supplying and consuming reactive power. WT generation in a time duration of 120 s is shown in Figure 4.5 [9]. For initial values of VFCSG, we test different values for time-constants τ_1 and τ_2; the best performance is obtained at 0.015 s and 0.75 s, respectively. The wind power fluctuates between 15% and 35% of 800 kVA as depicted in Figure 4.5. Typical value for discount factor is set at 0.75. Mid-level time interval is assumed 0.5 s. The pre-training for the mentioned networks is done on 15000 scenarios. The communication network topology is fully-connected for both frequency and voltage control. Therefore, the communication weight between LC i and j is chosen as $a_{ij} = 1$ and $b_{ij} = 1$ in W_f and W_v, respectively.

4.2.1 Dominant Eigenvalue Traces versus System Parameters

We examine impact of DVFC inputs on MG small-perturbation stability by monitoring the dominant eigenvalues. We increase controller gains independently around their nominal

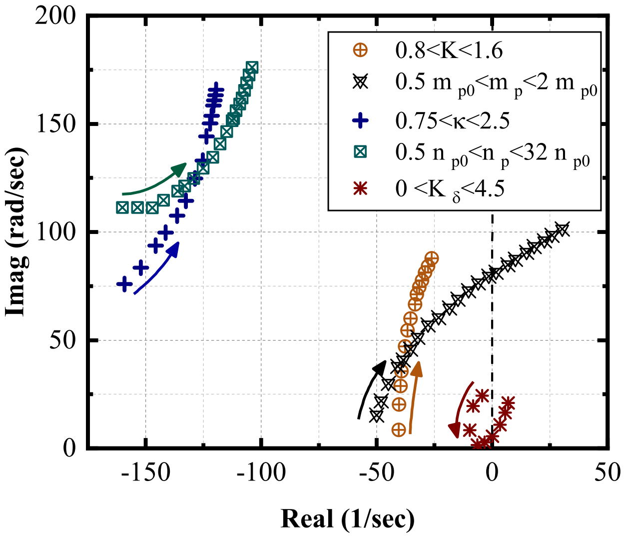

Figure 4.6: Eigenvalue traces of the MG control system for different values of ADHDP controller and VFCSG gains. Gains increase in the direction of arrows.

values at specific intervals. These critical eigenvalue trajectories are represented in Figure 4.6 with respect to changes in $K, \kappa, K_\delta, m_p, n_p$. Eigenvalues for power sharing controller and VFCSG gains correspond to the low-frequency critical mode of MG, and are extremely sensitive to changes in these parameters. Therefore, eigenvalues on the real axis are highly associated with frequency dynamics of the ESSs and VFCSG behaviour of SG, whereas complex conjugate eigenvalues correspond to voltage dynamics. In the DVFC scheme, SI changes from 104% in the case of $0.8K_{i0}$ to 80% in the case of $1.6K_{i0}$, demonstrating better robustness performance than that of conventional droop controllers. Figure 4.6 indicates that, by increasing K_δ, MG damping metric increases until it reaches a certain point where any further increment of K_δ deteriorates overall MG damping. Observe that $K_\delta = 1.5$ results in the best stability margin and MG damping; thus, we choose this value as the VFCSG gain for the time-domain simulation studies. We evaluate the time delay margin for each controller to keep MG stable. The time delays margin for the mid-level and secondary controllers are 0.5 s and 4.2 s, respectively, whereas MG operates in a stable region. Note that this analysis is performed to determine the operational constraints of $K, \kappa, K_\delta, m_p, n_p$ in the proposed DVFC.

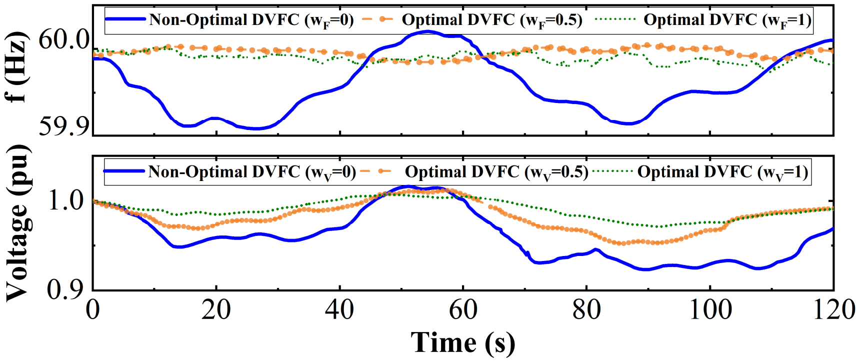

Figure 4.7: (a) Frequency and (b) voltage responses due to the wind power fluctuation in Scenario 2.

4.2.2 DVFC for Frequency and Voltage Regulation (Scenarios 1,2)

In Scenario 1, the corresponding weight $\omega_{\mathcal{F}}$ for frequency regulation is tested from 0 to 1 in order to evaluate effectiveness of the cost-to-go function as a pure frequency response. To emphasize the impact of DVFC on frequency regulation, we consider weights of other utility functions, $w_x, x \in \{\mathcal{V}, \mathcal{C}, \mathcal{E}\}$ equal to zero. Therefore, simulation results compare only impact of non-optimal DVFC ($w_{\mathcal{F}} = 0$) and optimal DVFC with two weights ($w_{\mathcal{F}} = 0.5$ and $w_{\mathcal{F}} = 1$) on frequency regulation. Figure 4.7 depicts frequency response under different scenarios. Observe that $w_{\mathcal{F}} = 1$ yields less frequency deviation from the nominal value, different from the non-optimal DVFC. In Scenario 2 with $0 \leq w_{\mathcal{V}} \leq 1$, same analysis is performed on voltage regulation to minimize voltage bus deviation from its nominal value. Similarly, we analyze the DVFC impact on voltage regulation by setting weights for other utility functions, $w_x, x \in \{\mathcal{F}, \mathcal{C}, \mathcal{E}\}$ to zero. Figure 4.7 represents that voltage deviation is kept within the acceptable operating range of [0.95, 1.05] p.u. (V^{ll}_{base}=208 V). This shows a better performance compared to non-optimal solution in which voltage profile reaches values of less than 0.95 p.u. in presence of wind fluctuations. Finally, observe that DVFC is capable of providing smooth frequency and voltage regulation, as wind power increases up to 35%. Because of having two ESSs and less wind power fluctuations in this test case, the frequency profile in base approach is deviated between 59.9 and 60 HZ which is much less than that in Figure 3.13 (between 59.5 and 60 Hz). Similar analysis is performed on voltage profile in comparison of two mentioned figures.

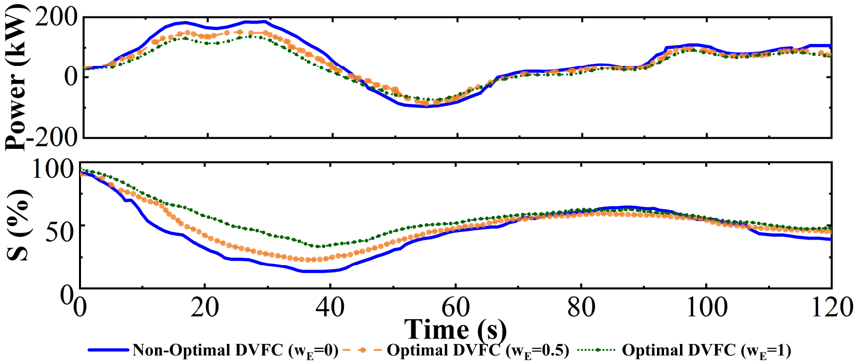

Figure 4.8: (a) Active power (b) SOC of battery in presence of wind fluctuation in Scenario 3.

4.2.3 DVFC versus Battery Penetration (Scenario 3)

Two ESSs are connected to buses #4 and #6, and are being charged and discharged according to power and supply imbalance in MG. It has a regulation capacity of 30 MW/Hz [31], which is a high-frequency droop controller as compared to diesel-based SGs. Note that we highlight effect of DVFC on ESS's life-cycle degradation by considering other utility weights, $w_x, x \in \{\mathcal{F}, \mathcal{V}, \mathcal{C}\}$ to be zero. To achieve a longer ESS life-cycle and to improve the ESS active and reactive power sharing, we use a droop control model based on Figure 3.4. We assume that the ESSs are initially fully charged (approximately 94%), and that minimum SOC for the ESSs is set at 10%. We also assume that the required capacity of the ESSs over a time interval of 120 s is 20 kWh, and wind power fluctuation in Figure 4.5 occurs periodically for 30 times in one hour; thus, the ESSs should be large enough to store 600 kWh. As can be observed in Figure 4.8, the DVFC results in less discharging power than the conventional model, and keeps the SOC of ESSs within a desired range. This causes an improved ESS life-cycle in a long time-horizon. It is assumed that charging and discharging modes of ESSs periodically follow a pattern of Figure 4.8 more than 30 times per hour. According to [82], life-cycle of Li-ion batteries increases up to twice by changing the ESS's depth of discharge level; thus, life-cycle of the ESS for non-optimal DVFC $w_{\mathcal{E}}$=0: 2000, optimal DVFC with $w_{\mathcal{E}}$=0.5: 3500, and optimal DVFC with $w_{\mathcal{E}}$=1: 4200 are achieved.

4.2.4 Minimum Operating Cost with DVFC (Scenario 4)

This scenario is conducted to evaluate the DVFC performance in a more-efficient dispatch solution in the CIGRE test system. In this scenario, only weight of operating cost

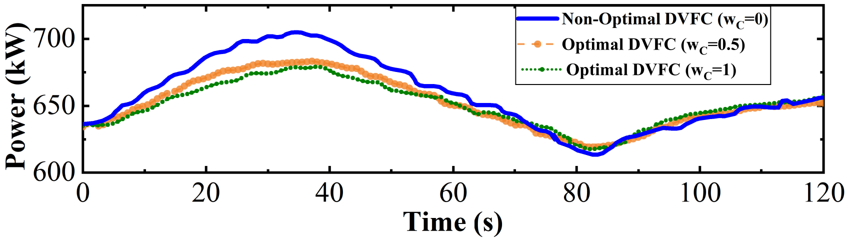

Figure 4.9: Dispatch of diesel-based SG #3 in Scenario 4.

Table 4.4: Energy of diesel generators $D_{1,2,3}$ (MWh) and operating cost for 24hr in Scenario 4

Algorithms	D_1	D_2	D_3	$\Delta\mathcal{C}$ (\$)
Non-optimal DVFC	17.57	15.34	19.20	5,310.9
Optimal DVFC ($w_\mathcal{C} = 0.5$)	17.22	20.11	15.05	5,060.9
Optimal DVFC ($w_\mathcal{C} = 1$)	17.15	22.09	13.39	4,991.3

function is non-zero. This assumption makes it easier to specifically demonstrate impact of DVFC on operating cost of MG. Therefore, only diesel-based SGs are considered as dispatchable generators. Similar to scenarios 1-3, performance of DVFC is compared with that of non-optimal solution ($w_\mathcal{C} = 0$) for a duration of 120 s. Figure 4.9 shows the diesel-based generation power of unit #3. The higher weight for the cost utility function results in less power generation in diesel-based generators as cost-driven units. To validate the effects of operating cost and energy generated by diesel units, we run the simulation for a period of 24 hours with dispatch intervals of 4.2 s. The performance of proposed DVFC is compared with results obtained from a mixed integer nonlinear programming method in GAMS, referred to as conventional UC. The conventional UC used in this simulation result is fully presented in [84]. Note that the conventional UC is only applied on the secondary controller. Observe in Table 4.4 that operating cost of DVFC is less than that of the conventional UC, indicating that the conventional UC overestimates the required energy for expensive diesel-based SGs during the sub-interval. The DVFC reduces operating cost by 6.01%, leading to saving of \$319.6 per day more than the conventional UC.

4.2.5 Optimum Performance of DVFC (Scenario 5)

In this scenario, optimum performance of DVFC is achieved by choosing proper weight for each utility function. We define performance indices (PIs) for frequency and voltage,

Table 4.5: Optimal DVFC versus conventional UC for 24 hr of operation in Scenario 5

Methods	PI_f	PI_v	$\Delta\mathcal{E}$(kWh)	$\Delta\mathcal{C}$(\$)
UC(CDF)	8.40	8.34	1,585.8	4,991.3
UC(EDF)	9.22	7.93	1,281.9	5,219.6
UC(CDF+EDF)	8.72	8.44	1,436.1	5,202.6
Proposed DVFC	4.42	6.11	1,431.3	5,126.4

given by

$$\mathrm{PI}_f = \sum_{m=1}^{n_m} \sum_{t=1}^{n_T} \frac{|\omega^m(t) - \omega_0|}{\omega_0}, \tag{4.13a}$$

$$\mathrm{PI}_v = \sum_{m=1}^{n_m} \sum_{t=1}^{n_T} \frac{\sum_{b \in \mathcal{B}} |V_i^m(t) - V_0|}{V_0}. \tag{4.13b}$$

To validate superiority of the proposed DVFC comparing to the conventional UC, PIs for frequency and voltage, energy generated by ESSs, and operating cost of MG are evaluated. The conventional UC is evaluated by using MINLP with the CPLEX solver for 24 hours of operation. We solve the multi-objective function by using a fuzzy weighted sum algorithm as presented in [85]. The optimal solutions for each normalized utility function are achieved separately, and then are ranked based on a fuzzy Pareto-front selection. The optimum weights for all normalized utility functions are $w_{\mathcal{F}} = 0.12$, $w_{\mathcal{V}} = 0.15$, $w_{\mathcal{E}} = 0.28$, and $w_{\mathcal{C}} = 0.45$ (with $\sum_{i \in \{\mathcal{F},\mathcal{V},\mathcal{E},\mathcal{C}\}} w_i = 1$). Table 4.5 summarizes the differences between DVFC and conventional UC based on four different indices. Conventional UC optimizes different objective functions in each iteration with two objective functions, i.e., cost-driven function (CDF), and energy-driven function (EDF) for ESSs. For evaluation of DVFC performance in 24 hours, four different models of CDF, EDF, both CDF and EDF without frequency and voltage regulation, and the proposed DVFC are compared in Table 4.5. The proposed DVFC improves frequency and voltage PIs by the amount of %40-50 and %60-65 of those in conventional UCs, respectively. The minimum $\Delta\mathcal{E}$, leading to less battery life-cycle degradation, is achieved in the case of individual EDF model ($\Delta\mathcal{E}$=1,281.9 kWh), and same convention is applied for the UC with individual CDF consideration ($\Delta\mathcal{C}$=\$4,991.3). Although, the DVFC demonstrates inefficiency in operation cost and ESS life-cycle with respect to individual CDF and EDF models, it compromises optimization of operating cost

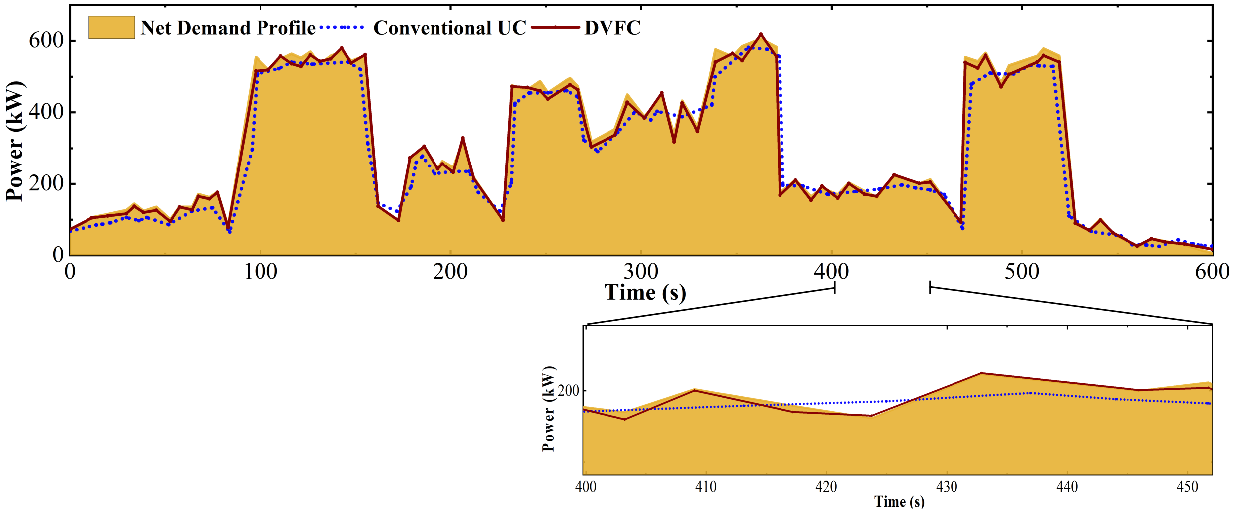

Figure 4.10: (a) Coverage of net demand profile. (b) Total uncovered net demand profile for both conventional UC and the proposed DVFC.

and ESS life-cycle degradation, while keeping frequency and voltage with only minimum deviation from their desired values. Furthermore, DVFC demonstrates better performance in coverage of net demand profile than conventional UC as shown in Figure 4.10. The DVFC reduces uncovered net demand profile to less than 50% of that when using conventional UC (i.e., uncovered energy is reduced to 4.7 kWh from 9.31 kWh).

4.3 Summary

In this chapter, a dynamic voltage and frequency controller is proposed for optimizing operating cost of dispatchable units and ESS life-time in an islanded MG. Numerical results show that the DVFC regulates frequency and voltage of MG as a mid-level controller. This mid-level controller covers time intervals between those of primary and secondary controllers and avoids the stair-pattern generation scheduling in conventional UCs. The DVFC takes advantage of dynamic programming and reinforcement learning to approximate MG operating cost, life-cycle of ESSs, and frequency and voltage regulations. Three NNs are incorporated in DVFC to find the optimal dispatches for generation units. Additionally, the controller does not require a mathematical model of MG to calculate the utility functions such as frequency and voltage regulation. Through several scenarios in a CIGRE test system, it is shown that the DVFC reduces frequency and voltage deviations from their desired values, and minimizes operating cost of generation units. Its optimal control policy extends the life-cycle of ESSs up to twofold. With proper training and parameter configuration of DVFC, islanded MGs can be controlled intelligently to be self-adaptive, stable, and operating cost-efficient.

Chapter 5

Time Delay in Frequency and Voltage Controller

The MGCC ensures stable and optimal operation at the secondary control level. The mid-level controller for the MGCC, proposed in Chapter 4, optimizes droop controller parameters to cover timescale difference between the fast synchronization-enforcing primary controller and slower secondary controller. As mentioned in Chapter 1, communication delay causes LCs to use outdated power dispatches at the secondary control level. Consequently, this outdated reference power deviates frequency and voltage from their nominal values in the primary control level.

As shown in Figure 5.1, packet transmission from one LC to another over one communication link (i, j) takes τ_{ij}^{m} for the transmission time and queuing delay. This delay is used in the primary level between LCs, but operates according to mid-level control approach. The i^{th} dispatchable unit generates power after τ_i^c, a delay existing in frequency and voltage control loops. Finally, operating power information is sent to the MGCC to optimize operation cost and ESS life-cycle, which is received after τ_i^s at the i^{th} dispatchable unit. With these delays, LC and MGCC feedback information takes a longer time to arrive the controllers.

Simultaneous use of m and t, in the secondary and mid-level controllers, makes the formulation representation complex. To focus on delay impact on the mid-level controller, we simplify notation of the mid-level control variables $X^m(t) \to X(t)$ and secondary control parameters $X_0^m \to X_0$.

As an example, Figure 5.2 depicts two generation units with different droop curves that are in charge of meeting the load change requirement. As discussed in Chapter 4, the main objective of mid-level controller is to regulate frequency and voltage to their nominal set

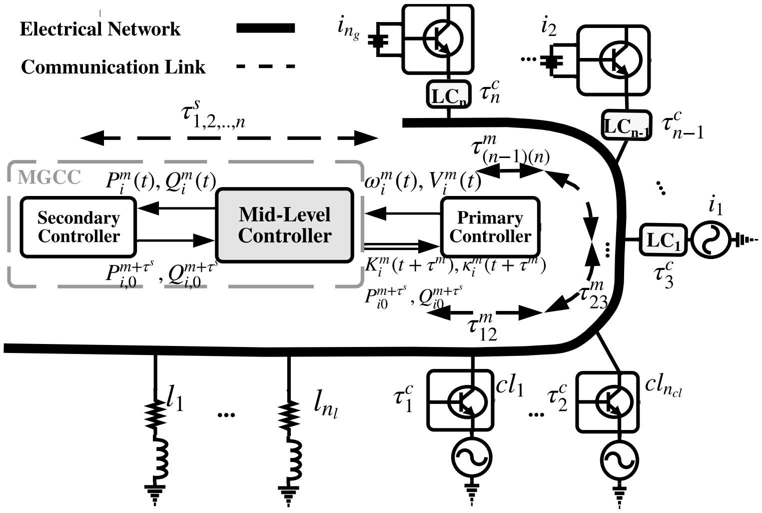

Figure 5.1: A schematic illustration of MG hierarchical control system with delays in communication networks (τ^m, τ^s) and control systems τ^c.

points by increasing their active and reactive power, such that

$$\lim_{t\to\infty} |\omega_i(t) - \omega_n| = 0, \tag{5.1a}$$

$$\lim_{t\to\infty} |V_{di}(t) - V_{dn}| = 0, \qquad i \in \Lambda_G. \tag{5.1b}$$

In the case of negligible time delay, generation units increase their active power ΔP_{DG_1} and ΔP_{DG_2}, and steady-state frequency is restored to ω_n by a shifting process. However, DG$_2$, which receives power information from the mid-level controller with delay τ^m, causes frequency to drop to $\omega(t+\tau^m)$ after τ^m seconds. Although the steady-state frequency for both cases is the same, time delay in DVFC causes significant deviations in frequency and active power sharing among generation units. Time-varying characteristic makes the issue more critical; hence, a time-varying ADHDP model is necessary to handle the time-varying delay at the mid-level control level.

5.1 Small-Perturbation Stability

Performance of the DVFC is analyzed considering time delays in the communication network, while the load or renewable energy power changes continuously. A small-

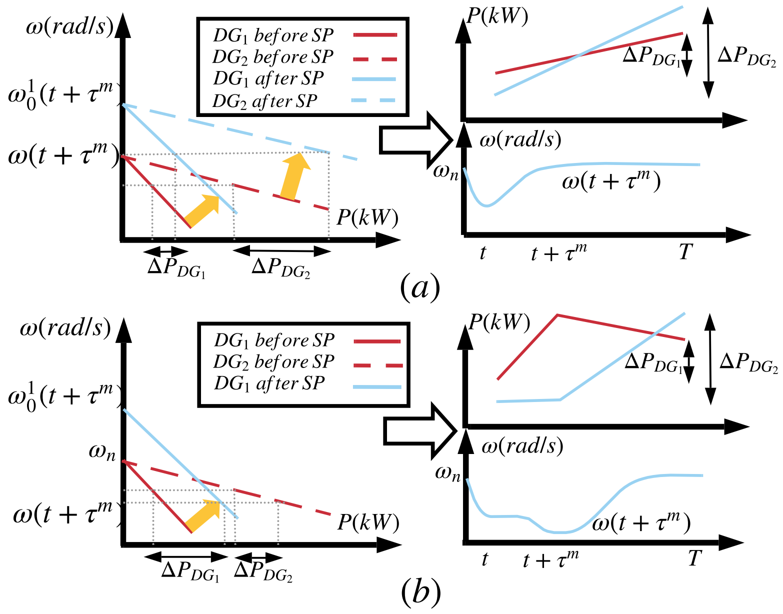

Figure 5.2: Frequency restoration in (a) negligible time delay (b) effective time delay τ^m in the mid-level controller before and after shifting process (SP).

perturbation analysis is carried out using eigenvalue studies around a specific operating point of the islanded MG. This approach provides the delay margin which is the maximum allowable time delay needed to guarantee MG stability. As indicated in Chapter 3, low-frequency dominant eigenvalue is largely sensitive to power sharing controller gains. Therefore, eigenvalue study yields system overall damping. We present the small-signal analysis in two cases of a) constant time delay b) time-varying delay.

5.1.1 Stability Analysis in Constant Time Delay

Consider time delay τ^m in LC-to-LC communication channels. Here, we study constant time delay τ^m in the mid-level controller. In particular, we focus on linear time-invariant (LTI) systems described by a state-space representation

$$\dot{x}(t) = A_0^{(MG)}x(t) + A_d^{(MG)}x(t - \tau^m) + B^{(MG)}D(t)$$
$$y(t) = C^{(MG)}x(t),$$

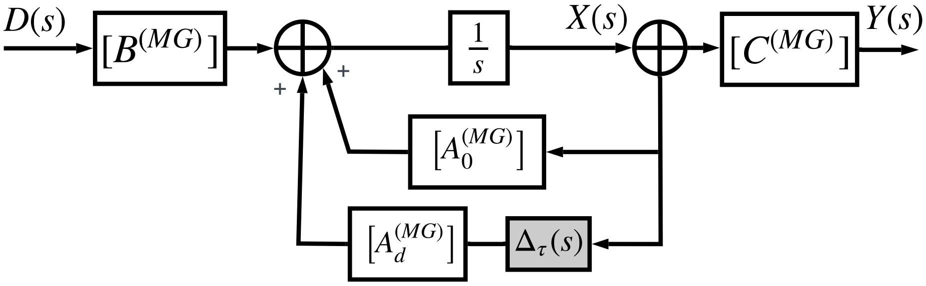

Figure 5.3: Input-output representation of an islanded MG under constant time delay.

$$x(t) = \begin{bmatrix} \Delta x^{(G)}(t) \\ \Delta i_{Ln,DQ}(t) \\ \Delta i_{Ld,DQ}(t) \end{bmatrix}, \tag{5.2}$$

where matrices $A_0^{(MG)}$ and $A_d^{(MG)}$ are derived based on decomposing the MG matrix into matrices non-sensitive and sensitive to time delay. Figure 5.3 recapitulates the effect of constant time delay in representation of control diagram, where $X(s) = \mathcal{L}\{x(t)\}$. The main purpose of presenting this input-output block diagram is to consider the stability problem of MG under time delay. The constant delay is represented by $\Delta_\tau(s) = e^{-\tau^m s}$ because of Laplacian transformation of a delayed function. Communication delays in different network links are assumed to be independent of each other and equal. Additionally, $B^{(MG)}$ is achieved from the load model presented in Appendix A. This matrix is calculated according to the connection of load change $d(t)$ to network model. Note that MG frequency and voltage of each bus are output of state-space model, and $C^{(MG)}$ connects state variable matrix $x(t)$ to output matrix $y(t)$.

Remark 6.1 *Laplacian transformation of a delayed function* $f(t-\tau)$ *is represented by* $\int_0^\infty f(t-\tau)e^{-st}dt = e^{-\tau s}\int_\tau^\infty f(t-\tau)e^{-st}dt = e^{-\tau s}F(s)$, where $F(s)$ is the Laplace transform of $f(t)$.

The characteristic equation of delayed descriptor system is

$$\det(\lambda_\tau I_0 - \Delta(\lambda_\tau, \tau^m)) = 0, \tag{5.3a}$$

$$\Delta(\lambda_\tau, \tau^m) = A_0^{MG} + A_d^{(MG)} e^{-\lambda \tau^m}, \tag{5.3b}$$

where λ_τ is the eigenvalue of MG system control with consideration of constant time delays, and I_0 denotes an identity matrix. With no time delay, $A^{(MG)}$ is equal to $A_0^{MG} + A_d^{(MG)}$ [58].

Theorem 6.1 [86] *The LTI system (5.3a) is stable if and only if*

(i) $A_0^{(MG)}$ *is stable,*

(ii) $A_0^{(MG)} + A_d^{(MG)}$ *is stable, and*

(iii) $\rho\big((j\omega I - A_0^{(MG)})^{-1} A_d^{(MG)}\big) < 1, \qquad \forall\omega > 0$

where $\rho(.)$ denotes the spectral radius of a matrix. Spectral radius of a matrix is the dominant eigenvalue of this matrix.

Remark 6.2 *The state-space model of an islanded MG is asymptotically stable if all generalized roots of its characteristics (5.3a) are in the open left-side plane.*

Remark 6.3 *A delay margin denoted by τ_{λ_m} means that the delayed descriptor system (5.3a) is stable for $\underline{\tau}^m < \tau_{\lambda_m}$, and unstable for $\underline{\tau}^m > \tau_{\lambda_m}$.*

Denote two conjugate eigenvalues on the imaginary axis of root-locus by $\lambda_\tau = \pm j\omega$. The characteristic equation is satisfied:

$$\begin{aligned}\pm j\omega &= eig(A_0^{(MG)} + A_d^{(MG)} e^{-j\omega\tau^m}) \\ &= eig(A_0^{(MG)} + A_d^{(MG)} e^{-j\eta}),\end{aligned} \tag{5.4}$$

where $eig(.)$ denotes the eigenvalues of a matrix. Note that $e^{-j\eta}$ is a periodic function of η with period of 2π; hence the characteristic equation is periodic with the period of 2π. With η changing within one period $[0, 2\pi]$, if there exist eigenvalues on the imaginary axis $\pm j\omega_m$ at η_m, the corresponding time delay margin τ_{λ_m} can be obtained by $\tau_{\lambda_m} = \eta_m/\omega_m$ [59].

Remark 6.4 *The critical eigenvalue is achieved from the dominant conjugate eigenvalue, denoted by $\lambda_c = \alpha_c \pm j\beta_c$, where critical damping of the system is $\xi_c = \dfrac{-\alpha_c}{\sqrt{\alpha_c^2 + \beta_c^2}}$.*

5.1.2 Stability Analysis in Time-Varying Delay

Presence of time-varying delays in MG frequency control loop may degrade its performance and cause instability in small sub-intervals. Different from those islanded MGs with constant-time delays, stability analysis for systems with time-varying delays proves far more difficult. Necessary and sufficient conditions are hardly computable; indeed the time-varying delay results merely fall into a restatement.

Here, we develop stability conditions for a general LTI control system in the form of (5.2). Therefore, we re-write space-state equations in (5.2) for time-varying delay $\tau^m(t)$ in the mid-level controller, given by

$$\dot{x}(t) = A_0^{(MG)} x(t) + A_d^{(MG)} x(t - \tau^m(t)). \tag{5.5}$$

Standard form of state-space equations with delays in each state variable $(x(t - \tau^m(t)))$ is efficient when the control system is small-scale. However, in a complex system control, state-space equations are modeled through a process of ”pulling out delays”, similar to ”pulling out uncertainties” [87], and do not contain any delays in a feed-forward subsystem. The stability problem of time-delay control systems, in general, is formidable from the numerical computation point of view; thus, we can consider an appropriate approximation. Such an approximation is reasonable as long as $\tau^m(t)$ is sufficiently small [86].

This stability problem with a time-varying delay is transformed to the standard form of scaled small gain (SSG) problem through one-term or two-term approximation of $x(t - \tau^m(t))$ [12]. In the robust control paradigm, the SSG theorem presents sufficient conditions for robustly asymptotic stability of approximation methods. The approximation analysis for time-varying delays is based on the lower $\underline{\tau}^m$ and upper $\overline{\tau}^m$ bounds of time-varying delay $\tau^m(t)$, which changes with sub-interval index t. In the one-term approximation method, $x(t - \tau^m(t))$ is approximated by $x(t - \tau_d^m)$, where τ_d^m is equal to $(\underline{\tau}^m + \overline{\tau}^m)/2$ [88]. The one-term approximation suffers from inaccuracy because of substitution of delay averaging for all sub-intervals.

In a two-term approximation, we model time-varying delay $\tau^m(t)$ using its lower bound and upper bound, which is limited by the time delay margin. The time-varying term can be written with a new transform variable $u(t)$, given by

$$\begin{aligned} &x(t - \tau^m(t)) = \frac{1}{2}\big(x(t - \overline{\tau}^m) + x(t - \underline{\tau}^m)\big) + \frac{\Delta\tau^m}{2} u(t), \\ &\Delta\tau^m = \overline{\tau}^m - \underline{\tau}^m, \qquad \underline{\tau}^m \leq \tau^m \leq \overline{\tau}^m. \end{aligned} \tag{5.6}$$

In (5.6), approximation error is derived from averaging descriptor of $x(t)$ from $\underline{\tau}^m$ to $\overline{\tau}^m$

(See Appendix B)

$$\begin{aligned} u(t) &= \frac{1}{2\Delta\tau^m}\int_{\underline{\tau}^m}^{\overline{\tau}^m} k_\psi z(t-\psi)d\psi \\ &= g_u(z(t)), \qquad \forall \tau^m(t) \in [\underline{\tau}^m, \overline{\tau}^m] \end{aligned} \tag{5.7}$$

where

$$k_\psi = \begin{cases} 1 & \psi \le t - \tau^m(t) \\ -1 & \psi > t - \tau^m(t). \end{cases} \tag{5.8}$$

Hence, (5.5) can be written as two transform systems S_z and S_u, given by

$$(S_z): \begin{cases} \dot{x}(t) = A_0^{(MG)}x(t) + A_d^{(MG)}\big(\frac{1}{2}[x(t-\overline{\tau}^m) + x(t-\underline{\tau}^m)] + \frac{\Delta\tau^m}{2}u(t)\big) \\ z(t) = \dot{x}(t) \end{cases} \tag{5.9a}$$

$$(S_u): u(t) = g_u(z(t)), \tag{5.9b}$$

where $z(t)$ is the second transform variable. The operator, $g_u(.)$, maps system domain (S_z) with variable $z(t)$ to (S_u) with index of $u(t)$, which is denoted by $z(t) \overset{g_u}{\to} u(t)$. The reverse mapping is denoted by $u(t) \overset{g_z}{\to} z(t)$. Hence, transformations of two systems are given by

$$(S_u): u(t) = g_u(z(t)), \tag{5.10a}$$

$$(S_z): z(t) = g_z(u(t)). \tag{5.10b}$$

Operator $g_u(.)$ is an integral operator with a time-varying signed function (k_ψ), which is transformed to Laplacian operator $G_u(s)$. In time interval t_i, variable k_ψ is calculated from (5.8), then new transformed variable $u(t_i)$ is achieved from (5.7). The frequency-domain operator, $G_u(s)$, is modeled as multiplicative uncertainty parameter[87] in an input-output (IO) approach shown in Figure 5.4. Multiplicative perturbation is defined as an uncertainty which is multiplied to the MG transfer function in the IO approach. In addition, $\Delta_\tau^a(s)$ is defined as $0.5\big(e^{-\underline{\tau}^m s} + e^{-\overline{\tau}^m s}\big)$. In the robust control paradigm, the SSG theorem presents sufficient conditions for robustly asymptotic stability of interconnected systems S_z and S_u.

Theorem 6.2 [89] *With consideration of (5.10a), assuming that S_z is an LTI stable sys-*

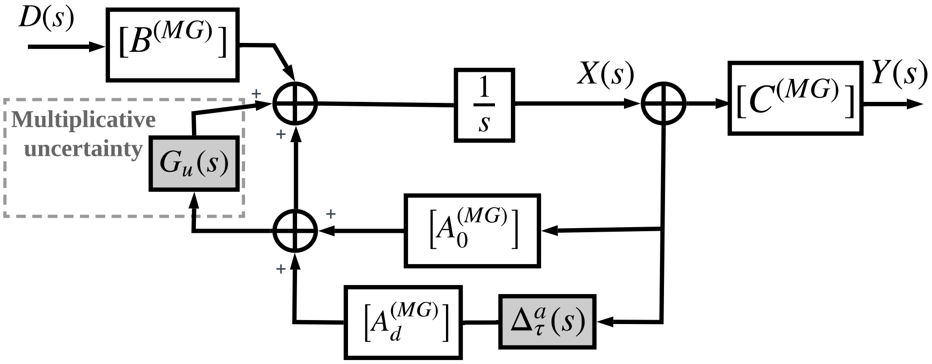

Figure 5.4: Two-term approximation method of time-varying delay in IO diagram.

tem, the closed-loop system formed by S_z *and* S_u *is asymptotically stable if there exists matrix* H *such that* $\|H \circ g_u \circ H\|_\infty \leq 1$ *holds .*

To satisfy the SSG condition $\|H \circ g_u \circ H\|_\infty \leq 1$, it is necessary to find a general invertible matrix H, such that $|HG_u(j\omega)H|$ is smaller than 1 for all frequencies ω. If operator g_u satisfies the SSG condition, the state-space model (5.9a) is stable. Note that the SSG condition is sufficient but not necessary for closed-loop stability [87]. Finally, interconnection of two transform systems can be re-written as

$$(S_z) : \begin{cases} \dot{x}(t) = A_0^{(MG)} x(t) + A_d^{(MG)} \Big(\dfrac{1}{2}[x(t-\underline{\tau}^m) + x(t-\overline{\tau}^m)] + \dfrac{\Delta\tau^m}{2} H^{-1}\hat{u}(t) \Big) \\ \hat{z}(t) = H\dot{y}(t) \end{cases} \tag{5.11a}$$

$$(S_u) : \hat{u}(t) = Hg_u(H^{-1}\hat{z}(t)), \tag{5.11b}$$

where $\hat{u}(t) = Hu(t)$ and $\hat{z}(t) = Hz(t)$ are new variables of two defined sub-systems. This general invertible matrix, H, is achieved in a trial-error way to make sure that the SSG condition is satisfied.

5.2 Large-Perturbation Stability

In this section, we extend the class of Lyapunov-Krasvoskii approach to complete the stability analysis. In comparison with the small-signal model for mid-level power control in Section 5.1, Lyapunov-based stability analysis covers a larger domain of validity and takes

into account the non-linear model of MG [69]. To adjust the DVFC proposed in Chapter 2 to Lyapunov-Krasvoskii stability analysis, we make some assumptions.
First of all, we use an approximation analysis in time-varying delay model which needs the time delay margin τ_{λ_m} obtained from the small-signal model. Therefore, small-perturbation stability is necessary to validate domain of allowable delay in islanded MG operation. Secondly, since the dynamic characteristics of the current and voltage controllers are much faster than those of the power controller, only performance of power controller is considered in the following analysis [62]. Prior to discussing large-signal analysis for MG control system, we start with Lyapunov-Krasvoskii theorem.
Theorem 6.3 [86] *Control system is asymptotically stable if and only if there exists a Lyapunov-Krasvoskii function,* $V(t)$*, that satisfies*

$$V(t) \geq \epsilon, \tag{5.12}$$

and Lyapunov-Krasvoskii derivative condition is given by

$$\dot{V}(t) \leq -\epsilon, \tag{5.13}$$

for some $\epsilon > 0$.
Consider a Lyapunov-Krasovskii function that controls frequency stability in MG, given by

$$V(t) = \sum_{i\in\Lambda_G} \left[(\delta\omega_i(t))^2 + \sum_{k\in\Lambda_G} a_{ik} \int_{t-\tau^m}^{t} \big(\delta\omega_k(\psi)\big)^2 d\psi\right]. \tag{5.14}$$

Note that the existence of such an energy function, which satisfies Lyapunov-Krasovskii functional conditions and derivative condition, is indeed a necessary and sufficient condition for asymptotic stability of the MG.
Proposition 6.1 *Observe that* $\dot{V}(t) \leq 0$ *if and only if,*

$$\begin{aligned} (2k_i+1)(\delta\omega_i(t))^2 + \sum_{k\in\Lambda_G} a_{ik}\big(\delta\omega_i(t) - \delta\omega_k(t-\tau^m)\big)^2 \\ \geq \sum_{k\in\Lambda_G} a_{ik}(\delta\omega_k(t))^2, \qquad \forall\{i,k\} \in \Lambda_G. \end{aligned} \tag{5.15}$$

To derive (5.15), the DVFC discussed in Chapter 4 for the frequency control is formulated as

$$\omega_i(t) = \omega_n - m_{pi}(P_i - P_{i,0}) + k_i\Omega_i(t), \tag{5.16a}$$

$$\dot{\Omega}_i(t) = \big(\omega_n - \omega_i(t)\big) - \sum_{k\in\Lambda_G} a_{ik}\big(\Omega_i(t) - \Omega_k(t-\tau^m)\big). \tag{5.16b}$$

The output frequency of each generation unit synchronizes to reference frequency ω_n. Taking the derivatives of (5.16a) yields

$$\dot{\omega}_i(t) = k_i\dot{\Omega}_i(t). \tag{5.17}$$

This condition is valid in each sub-interval t when the reference power, which is updated by the secondary controller, is constant during these sub-intervals. We define an error function to evaluate the stability by Lyapunov-Krasovskii method [62], given by

$$\delta\omega_i(t) = \omega_i(t) - \omega_n, \tag{5.18a}$$

$$\dot{\delta\omega}_i(t) = \dot{\omega}_i(t). \tag{5.18b}$$

Combining (5.18b) with (5.17) and (5.16b) yields

$$\begin{aligned}\dot{\delta\omega}_i(t) &= \dot{\omega}_i(t)\\ &= -k_i\delta\omega_i(t) - \sum_{k\in\Lambda_G} a_{ik}k_i\big(\Omega_i(t) - \Omega_k(t-\tau^m)\big).\end{aligned} \tag{5.19}$$

Observe from (5.14) that $V(t) \geq 0$, and $V(t) = 0$ if and only if $\delta\omega_i(t) = 0$ for all $\{i,k\} \in \Lambda_G$, and then we have $\omega_i(t) = \omega_n$. Consider that $\Delta P_i = 0$ during time delay in the mid-level control, given as

$$\begin{aligned}\omega_i(t) - \omega_k(t-\tau^m) &= k_i\big(\Omega_i(t) - \Omega_k(t-\tau^m)\big)\\ &= \delta\omega_i(t) - \delta\omega_k(t-\tau^m).\end{aligned} \tag{5.20}$$

Generally, Lyapunov-Kravoskii method requires many simplifying assumptions. Hence, $\Delta P_i \neq 0$ is a challenging and nontrivial issue which adds another level of complexity to the right-side of equation. This assumption needs further study. The time derivative of $V(t)$

in (5.14) is

$$\begin{aligned}\dot{V}(t) &= \sum_{i\in\Lambda_G}\Big[2\delta\omega_i(t)\delta\dot{\omega}_i(t) + \sum_{k\in\Lambda_G} a_{ik}\big((\delta\omega_k(t))^2 - (\delta\omega_k(t-\tau^m))^2\big)\Big]\\ &= \sum_{i\in\Lambda_G}\Big[-2k_i(\delta\omega_i(t))^2 - 2\sum_{k\in\Lambda_G} a_{ik}\big(\delta\omega_i(t) - \delta\omega_k(t-\tau^m)\big)\delta\omega_i(t)\\ &\qquad + \sum_{k\in\Lambda_G} a_{ik}\big((\delta\omega_k(t))^2 - (\delta\omega_k(t-\tau^m))^2\big)\Big]. \qquad (5.21)\end{aligned}$$

It is obvious that $\dot{V}(t) = \sum_{i\in\Lambda_G}\Big[-2k_i(\delta\omega_i(t))^2\Big]$ when $a_{ik} = 0$, and in a connected communication network, we have

$$\begin{aligned}\dot{V}(t) &= \sum_{i\in\Lambda_G}\Big[-(2k_i+1)(\delta\omega_i(t))^2 - \sum_{k\in\Lambda_G} a_{ik}\Big((\delta\omega_i(t))^2 - 2\delta\omega_i(t)\delta\omega_k(t-\tau^m)\\ &\qquad + (\delta\omega_k(t-\tau^m))^2 - (\delta\omega_k(t))^2\Big)\Big]\\ &= \sum_{i\in\Lambda_G}\Big[-(2k_i+1)(\delta\omega_i(t))^2 - \sum_{k\in\Lambda_G} a_{ik}\big(\delta\omega_i(t) - \delta\omega_k(t-\tau^m)\big)^2\\ &\qquad + \sum_{k\in\Lambda_G} a_{ik}(\delta\omega_k(t))^2\Big]. \qquad (5.22)\end{aligned}$$

5.2.1 Lyapunov Sufficient Condition in Constant Time Delay

It is possible to write the Lyapunov-Krasvoskii functional condition and its corresponding derivative condition in the form of linear matrix inequalities (LMIs).

Proposition 6.2 *MG with constant time delay described by (5.15) is asymptotically stable if there exists an $n^2 \times n^2$ matrix W, where W is positive semi-definite, and satisfies*

$$AWA^T\mathbb{1}_{n^2\times 1} \geq 0,$$

$$A = diag(A_h(t)), \quad W = diag(W_h(t)), \quad h \in \Lambda_G,$$

$$A_h(t) = [\delta\omega_1(t), \delta\omega_2(t), ..., \delta\omega_n(t)], W_h(t) = [w^h_{ij}(t)],$$

$$w_{ij}^h(t) = \begin{cases} 2k_i + \sum_{k\in\Lambda_G} a_{ik}, & i = j = h \\ \tau^m k_i(1+\tau^m k_i)a_{ih}, & i = j \neq h \\ -a_{hj}(1+\tau^m k_j), & i = h \neq j \\ -a_{ih}(1+\tau^m k_i), & i \neq j = h \\ 0, & i \neq j \neq h \end{cases}, \tag{5.23}$$

where $\mathbb{1}_{n^2\times 1}$ *is an* $n^2 \times 1$ *matrix where every element is equal to one;* A *is an* $n^2 \times n^2$ *frequency deviation matrix with* $A_h(t) \in \mathbb{R}^n$*.*

Remark 6.5 [90] *An* $n^2 \times n^2$ *symmetric real matrix* $W_h(t)$ *is said to be positive semi-definite or non-negative definite if* $A_h(t)W_h(t)A_h(t)^\intercal \geq 0$ *for all* $A_h(t) \in \mathbb{R}^{n^2}$*. Formally,*

$$W_h(t) \text{ positive semi-definite} \quad \Longleftrightarrow \quad A_h(t)W_h(t)A_h(t)^\intercal \geq 0 \text{ for all } A_h(t) \in \mathbb{R}^{n^2}. \tag{5.24}$$

Note that W is a diagonal matrix with arrays of $W_h(t)$ for $h \in \Lambda_G$; hence W is positive semi-definite. Based on characteristics of positive semi-definite matrices, W is positive semi-definite if and only if all of its eigenvalues are non-negative.

To derive (5.23), according to (5.22), sufficient conditions of $\dot{V}(t) \leq 0$ is achieved by

$$\begin{aligned}(2k_i+1)(\delta\omega_i(t))^2 + \sum_{k\in\Lambda_G} a_{ik}\big(\delta\omega_i(t) - \delta\omega_k(t-\tau^m)\big)^2 \\ \geq \sum_{k\in\Lambda_G} a_{ik}(\delta\omega_k(t))^2, \qquad \forall\{i,k\} \in \Lambda_G.\end{aligned} \tag{5.25}$$

Taking Laplacian transform of $\delta\omega_i(t) - \delta\omega_k(t-\tau^m)$ yields

$$\delta\omega_i(s) - \delta\omega_k(s)e^{-\tau^m s} \approx \delta\omega_i(s) - \delta\omega_k(s)(1-\tau^m s), \tag{5.26a}$$

$$\mathcal{L}^{-1}\{\delta\omega_i(s) - \delta\omega_k(s)(1-\tau^m s)\} = \delta\omega_i(t) - \delta\omega_k(t) + \tau^m\delta\dot{\omega}_k(t). \tag{5.26b}$$

Using (5.19) results in

$$\begin{aligned}\delta\omega_i(t) - \delta\omega_k(t) + \tau^m\delta\dot{\omega}_k(t) = \delta\omega_i(t) - (1+\tau^m k_k)\delta\omega_k(t) \\ - \sum_{j\in\Lambda_G} a_{kj}\big(\Omega_k(t) - \Omega_j(t-\tau^m)\big).\end{aligned} \tag{5.27}$$

At the end of each sub-interval t, averaging distributed terms $\Omega_k(t) - \Omega_j(t-\tau^m) = 0$ and then the sufficient condition, is given by

$$(2k_i+1)(\delta\omega_i(t))^2+\sum_{k\in\Lambda_G}a_{ik}\big(\delta\omega_i(t)-(1+\tau^m k_k)\delta\omega_i(t)\big)^2 \\ \geq \sum_{k\in\Lambda_G}a_{ik}(\delta\omega_k(t))^2, \qquad \forall\{i,k\}\in\Lambda_G. \tag{5.28}$$

The inequality (5.28) satisfies Lyapunov-Krasvoskii condition $\dot{V}(t) < 0$ for the i^{th} unit, which is extended to all units in an LMI format observed in Proposition 6.2. Since both Lyapunov-Krasvoskii functional condition and its derivative condition are satisfied, the MG control system is asymptotically stable.

5.2.2 Lyapunov Sufficient Condition with Time-Varying Delay

A stability criterion is developed based on implicit model transformation. This model transformation uses the two-term approximation approach presented in Theorem 6.2. As is well known, it is usually impossible to describe Lyapunov-Krasvoskii functional conditions with parasitic variables that are time-varying. Here, we derive the necessary and sufficient conditions in the form of LMIs.

Proposition 6.3 *MG with time-varying delay described by (5.15) is asymptotically stable if there exists an $n^2\times n^2$ matrix W, where W is positive semi-definite, and satisfies*

$$\big(AW_1A^T+AW_2U+UU^T\big)\mathbb{1}_{n^2\times 1}\geq 0,$$

$$U=diag(u_h(t)), u_h(t)=\frac{1}{\sqrt{2}}[u_1(t),u_2(t),...,u_n(t)],$$

$$W_1=diag(W_{1,h}(t)), W_{1,h}(t)=[w^h_{1,ij}(t)],$$

$$W_2=diag(W_{2,h}(t)), W_{2,h}(t)=[w^h_{2,ij}(t)],$$

$$A=diag(A_h(t)), A_h(t)=[\delta\omega_1(t),\delta\omega_2(t),...,\delta\omega_n(t)],$$

$$w^h_{2,ij}(t)=\begin{cases}\sum_{k\in\Lambda_G}a_{ik}, & i=j=h\\ -a_{ih}, & i=j\neq h\ ,\\ 0, & o.w\end{cases} \tag{5.29}$$

$$w^h_{1,ij}(t) = \begin{cases} 2k_i + \sum_{k\in\Lambda_G} a_{ik}, & i = j = h \\ \tau^m k_i(1+\tau^m k_i)a_{ih}, & i = j \neq h \\ -a_{hj}(1+\tau^m k_j), & i = h \neq j \\ -a_{ih}(1+\tau^m k_i), & i \neq j = h \\ 0, & i \neq j \neq h \end{cases}.$$

In the aforementioned formulation of the small-signal model, two critical issues closely related to reduction of conservatism are how to pull out the time-varying delay, and to what degree of precision the uncertain delay $\tau^m(t)$ can be estimated. The small-signal model uses a two-term equation to approximately capture the impact of time-varying delay, given by

$$\delta\omega_i(t-\tau^m(t)) = \frac{1}{2}[\delta\omega_i(t-\underline{\tau}^m) + \delta\omega_i(t-\overline{\tau}^m)] + \frac{\Delta\tau^m}{2}u_i(t). \tag{5.30}$$

This approximation is derived from two-term approximation method in (5.6), where $\tau^m(t)$ is bounded by $\underline{\tau}^m$ and $\overline{\tau}^m$. As mentioned in (5.7), approximation error is given by

$$u_i(t) = \frac{1}{\Delta\tau^m}\int_{\underline{\tau}^m}^{\overline{\tau}^m} k_\psi \delta\dot{\omega}_i(t-\psi)d\psi. \tag{5.31}$$

With a reasonable assumption, $\underline{\tau}^m = 0$, according to (5.22), sufficient condition to have $\dot{V}(t) \leq 0$ is achieved by

$$(2k_i+1)(\delta\omega_i(t))^2 + \sum_{k\in\Lambda_G} a_{ik}\big(\delta\omega_i(t) - (1+\frac{1}{2}\overline{\tau}^m k_k\delta\omega_k(t)) - \frac{1}{2}u_i(t)\big)^2$$
$$\geq \sum_{k\in\Lambda_G} a_{ik}(\delta\omega_k(t))^2, \qquad \forall\{i,k\}\in\Lambda_G. \tag{5.32}$$

This inequality satisfies Lyapunov-Krasvoskii condition for the i^{th} unit. To extend it to all units, we need an LMI format proposed in Proposition 6.3. The LMI format of (5.32) is summarized into (5.29).

5.3 Time Delay-based DVFC

The preceding analysis provides an LMI form of necessary and sufficient conditions to achieve MG stability. Although these conditions determine whether an MG operation is stable or not, they cannot guarantee MG stability in a time horizon. We propose a delay-based DVFC to minimize the impact of delay in communication networks on the islanded MG's transient performance as load and renewable energy resources change.

It is necessary to explain why we present two solutions when large-signal analysis covers the small-signal one. As discussed in Chapter 1, small-signal analysis is only valid around operating point by linearizing the model of MG components. Although it does not show how far MG stability margin is from an unstable region, it simplifies the analysis by calculating a time delay margin, as a valuable index. Additionally, large-perturbation analysis depends on energy function definition and corresponded assumptions which cannot extend to different types of controller (e.g., frequency or voltage controller), while small-signal analysis proposed in Section 5.1 models each individual component in the islanded MG, which is suitable for a variety of control designs. Therefore, Sections 5.1 and 5.2 derive LMI formats of MG stability for either small or large signal perturbation models. In the following subsections, two delay-based DVFC solutions are developed for a) small and b) large-signal analysis.

5.3.1 DVFC with Small-Signal Critic Network

As discussed in Chapter 4, an ADHDP model is essentially a juxtaposition of dynamic programming. Note that the dynamic programming approach calculates action variables $(k_i(t), \kappa_i(t), Z_{v,i}(t), K_{\delta,i}(t))$ via optimal Bellman function. Adaptive critic concept utilizes an approximation of the optimal cost-to-go function to accomplish mid-level control design. The operational critic network, $\mathcal{J}_u[a(t), s(t)]$, minimizes MG frequency and voltage, operating cost, and ESS life-time degradation.

This optimal behaviour of DVFC is only valid when a control system maintains MG stability with a desirable margin. The time delay existing in the communication network causes frequency oscillation in the system control; hence, it degrades the transient performance of MG control. A deviation out of the delay margin can force the system control to unstable region. Therefore, an inner loop of operational critic networks in Figure 4.2 is designed to maintain MG stability in a desirable margin, while maintaining frequency and voltage regulation. The stability evaluator monitors stability margin index, which is achieved by any change in action and status variables. Denoting the stability margin by $\psi(t)$ at t^{th} sub-interval time, we have

$$\psi(t) = \arg\max_{\lambda} \mathbb{R}\big(\lambda[a(t), s(t)]\big), \tag{5.33}$$

where λ is the dominant eigenvalue from (5.4) for the constant time delay and (5.11a) for time-varying delay models. The stability critic network, $\mathcal{J}_s[a(t), s(t)]$, maximizes stability margin in a fast control loop comparing to the operational critic network. The cost-to-go functions are given by

$$\mathcal{J}_u(t) = \sum_{k=0}^{n_T} \gamma^k U(t+k), \tag{5.34a}$$

$$\mathcal{J}_s(t) = \sum_{k=0}^{n_T} \gamma^k \psi(t+k), \tag{5.34b}$$

$$U(t) = w_{\mathcal{V}}\Delta\mathcal{V}(t) + w_{\mathcal{F}}\Delta\mathcal{F}(t) + w_{\mathcal{C}}\Delta\mathcal{C}(t) + w_{\mathcal{E}}\Delta\mathcal{E}(t), \tag{5.34c}$$

where utility function of voltage ($\Delta\mathcal{V}(t)$), frequency ($\Delta\mathcal{F}(t)$), MG operating cost ($\Delta\mathcal{C}(t)$), and ESS lifetime degradation ($\Delta\mathcal{E}(t)$) are defined in (5.4)-(5.6) with technical constraints in (5.4)-(5.9).

5.3.2 DVFC under Large-Signal Stability Constraints

As discussed in Subsection 5.3.1, time delay results in frequency oscillation in system control. Frequency oscillation under large perturbations is more severe than that of small disturbance. Therefore, the delay-based DVFC is aimed to damp this oscillation and maintain the stable MG control. Figure 4.2 depicts the stability critic network in subject to large perturbations. Different from the small-signal critic network, ADHDP diagram does not have inner loop because the energy function is defined in operational cost-to-go function, $\mathcal{J}_u[a(t), s(t)]$, as frequency utility function. The delay constraints for constant time delay in (5.23) and time-varying delay in (5.29) are added to other constraints (5.9)-(5.14).

Cost-to-go and utility functions are defined similar to (5.34a); however frequency utility

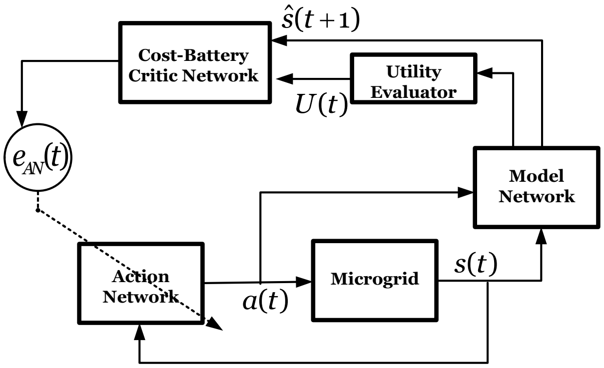

Figure 5.5: Diagram of the ADHDP subject to large perturbations.

function is formulated according to Lyapunov-Krasvoskii function, given by

$$\Delta\mathcal{F}(t) = \sum_{i\in\Lambda_G} \left[(\delta\omega_i(t))^2 + \sum_{k\in\Lambda_G} a_{ik} \int_{t-\overline{\tau}^m}^{t} \left(\delta\omega_k(\psi)\right)^2 d\psi\right]. \tag{5.35}$$

This delay-based DVFC has new functionality compared to the DVFC in Chapter 4:

- The stability LMI formats of (5.23) and (5.29) for operational critic network train the action network to reject action variables which leads to MG instability. These constraints are added to the cost-to-go function as a penalty function. If these constraints are not satisfied, the total cost-to-go function has a high value; hence, derivative of the cost-to-go function to action network is not minimized in action error. This behavior causes the action network to reject corresponded action variables in a control loop;

- The proposed utility function uses integral of MG frequency over time delay horizon; hence, delay-based DVFC mitigates MG oscillation caused by time delay in communication network.

Although action, critic, and model networks perform to minimize the cost-to-go function, same as the DVFC discussed in Chapter 4, a delay constraint checks validity of action variable in each iteration. Action variables which do not meet the LMI conditions in (5.23) and (5.29) are not dispatched. Consideration of energy function in LMI formats of (5.23) and (5.29) adds complexity to control design; however, it is essential to collect

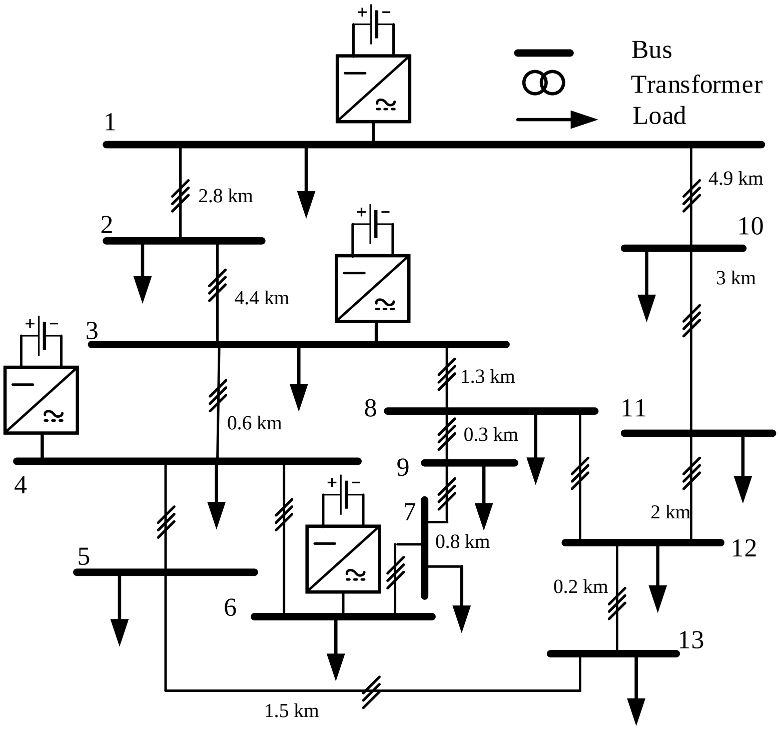

Figure 5.6: MG test case based on modified CIGRE benchmark [31].

frequency behavours during time delay. According to Table 4.2, time response of the ADHDP algorithm is around 10 μs, while training time for each neural network varies from 100 s to 600 s, depending to size of control system.

5.4 Numerical Results

The effectiveness of delay-based DVFC is evaluated in an islanded MG implemented in MATLAB/SimPowerSystems. A diagram of the test system is shown in Figure 5.6. This European medium-voltage benchmark features a total installed capacity of 2.4 MVA and includes four batteries in buses #1, #3, #4, and #6. There are 13 critical loads. Feeders are connected together via 14 coupled π sections. A detailed description of the test system and parameters is provided in Appendix C [9, 91]. Maximum power rating of each ESS is 600 kW. These batteries store rated energy of up to 12000 kWh, and are connected to a network through bidirectional voltage source controllers. Acceptable minimum SOC of each ESS is 1200 kWh.

ESSs share active and reactive power via a fully connected communication network. Therefore, communication weight between LC i and j is chosen as $a_{ij} = 1$ and $b_{ij} = 1$. Nominal voltage V_n and frequency ω_n are set as 1 p.u. and 377 rad/s, respectively. This section is organized into four studies, beginning with a dominant eigenvalue analysis of controller in small perturbation, and examining controller performance under small and large perturbations, in two cases of constant and time-varying delays.

The fully-connected communication topology is illustrated in Figure 5.7 with frequency adjacency matrix W_f. Similarly, voltage adjacency matrix W_v uses a fully-connected communication network. As depicted in Figure 5.6, we exclude diesel-generator SGs because of delay in their system control; hence, inverter-based test cases are considered. Generally, inverter-based DGs have small inertia, and their frequency and voltage responses are fast. Their time response is in the range of 180 μs which is negligible. Therefore, this assumption is useful to highlight impact of communication delays on control system performance. Note that considering delays in both control system of SGs and communication network is out of scope of this thesis. Typically, the primary control time is smaller than 4 s, and the secondary control time is more than 4 s up to several minutes. Thus, these DGs can act fast after receiving mid-level set-points from the MGCC.

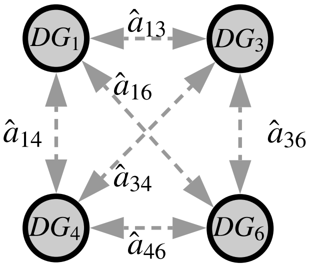

$$a_{ii} = \textstyle\sum_{j\in\Lambda_G} \hat{a}_{ij}$$

$$a_{ij} = -\hat{a}_{ij}$$

$$W_f = \begin{pmatrix} 3 & -1 & -1 & -1 \\ -1 & 3 & -1 & -1 \\ -1 & -1 & 3 & -1 \\ -1 & -1 & -1 & 3 \end{pmatrix}$$

Figure 5.7: Schematic of communication structure of the MG consisting of four inverter-based units.

5.4.1 Constant Delay-based DVFC under Small Perturbation

We study performance of the DVFC controller under various time delays and controller tunings. As in Chapter 4, active and reactive power are accurately shared among ESSs via

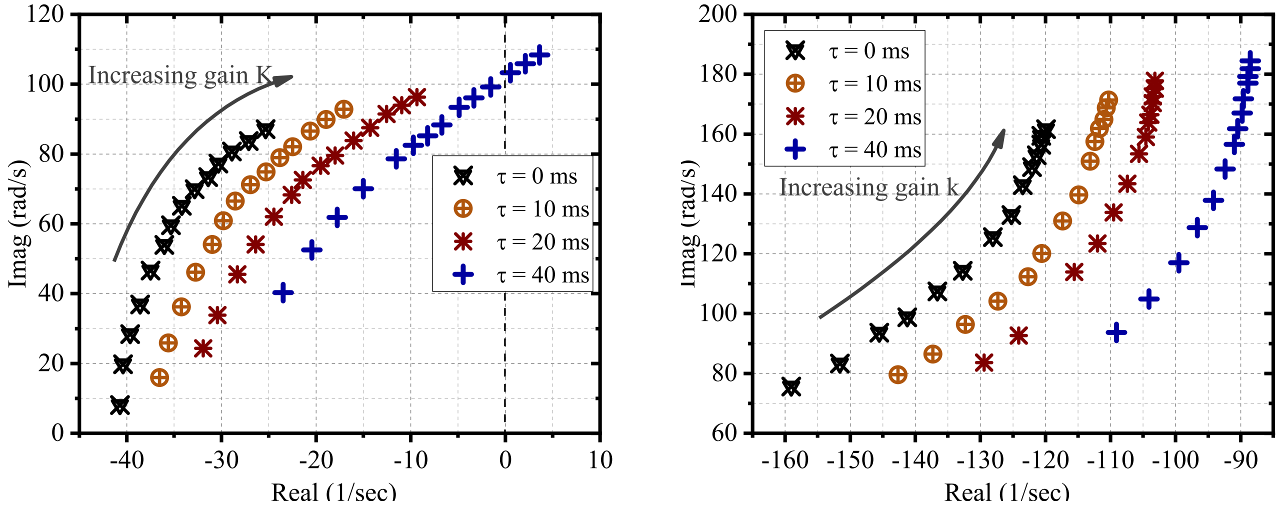

(a) (b)

Figure 5.8: Eigenvalue traces of power and voltage controller with different communication delays. (a) Frequency and (b) voltage gains of DVFC increase in the direction of arrows.

changing two control gains i.e., K and κ. Increasing these gains results in more contribution to power sharing but may cause MG instability. Four inverter-based units have same DVFC frequency and voltage control parameters with $K = 1$ and $\kappa = 1.2$, and Q-V gain, $\beta = 0.75$, for balancing reactive power sharing and voltage regulation. Figure 5.8 (a) shows four streams of eigenvalues for the power controller, where arrows indicate the direction of increasing frequency gains. Dominant eigenvalues in the power controller move slightly towards unstable region as time delay τ^m increases from 0 to 40 ms. Additionally, an increment in time delay causes the low-frequency oscillation because of increasing conjugate part of the dominant eigenvalue. It leads to less damping parameter, ξ_c, as presented in Remark 6.4. Figure 5.8 (a) depicts that increasing frequency gains improves MG stability and low-frequency oscillation.

Figure 5.8 (b) illustrates that increasing the voltage gains enhances MG stability; but dominant eigenvalues in the voltage controller are less sensitive to time delay than that in the power controller. Note that a change in the voltage gain has an impact on the reactive power sharing among generation units, which may cause inaccurate power sharing. Time delay increases the conjugate part of the dominant eigenvalue, which causes the under-damped voltage response. Table 5.1 shows the overall damping achieved from the dominant

Table 5.1: Dominant eigenvalue damping around nominal operation

Controller	$\tau^m = 10ms$	$\tau^m = 20ms$	$\tau^m = 30ms$	$\tau^m = 40ms$
Power	0.51	0.39	0.28	0.11
Voltage	0.71	0.67	0.58	0.49

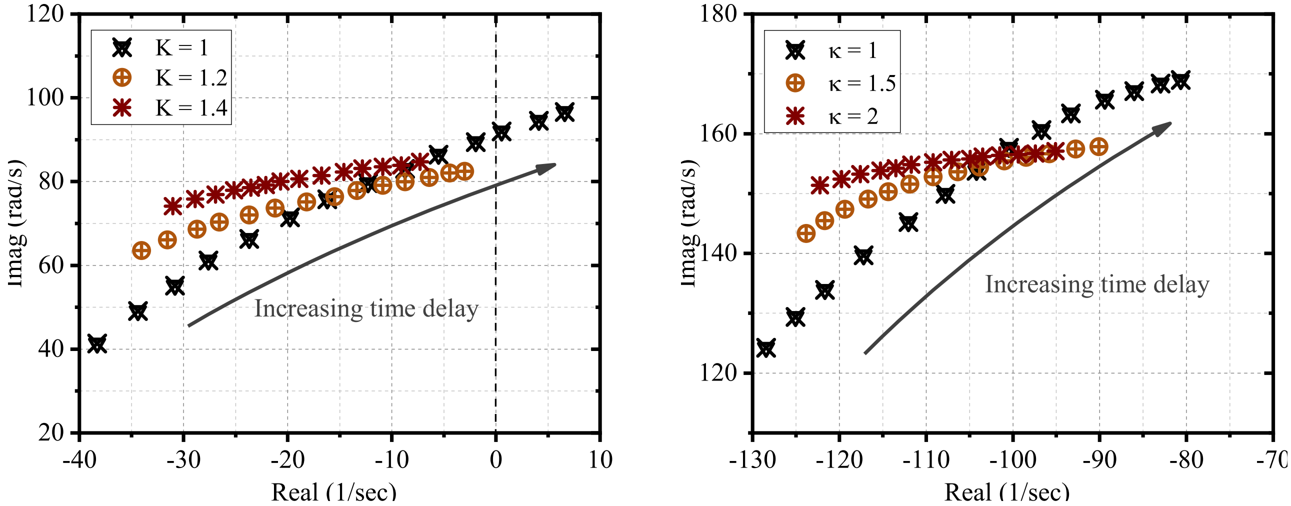

(a) (b)

Figure 5.9: Eigenvalue streams in different constant (a) frequency and (b) voltage DVFC gains. The communication time delay increases from τ^m=0 to τ^m=40 ms in the direction of arrows.

eigenvalue of power and voltage controller. Observe that dominant eigenvalue damping around nominal operation in the power controller is more critical than that of the voltage controller. The increasing time delay up to τ^m=40 ms reduces the dominant eigenvalue damping to 22 % of that in time delay τ^m=10 ms.

Figure 5.9 (a) shows that the increment of frequency gains from K=1 to K=1.4 reduces the eigenvalue sensitivity to time delay changes. According to (5.4), the time delay margin is around 69 ms in the case of K=1. Increasing the frequency gains to K=1.2 and K=1.4 allow the system control to be stable subject to time delays of up to 78 and 81 ms, respectively. Although increment of frequency gain brings the mentioned advantages, it leads to less MG instability as depicted in Figure 5.8.

Figure 5.8 presents dominant eigenvalue traces in subject to different time delays, and Figure 5.9 illustrates these traces according to different frequency and voltage gains. Figure 5.9 (b) shows that increasing voltage gains enhance robustness of dominant eigenvalues subject to time delays (from τ^m=0 to τ^m=40 ms). Although time delay does not have an impact on voltage instability of the proposed system control, increasing voltage gains causes reducing conjugate part of a dominant eigenvalue; hence, low-frequency oscillation generated by time delay is improved.

Time-domain simulation is carried out to show the DVFC performance for T = 2 s. A 50 kW-load at bus #4 is detached at t=0.15 s. First considering a frequency transient response in Figure 5.10, frequency deviation experienced time delay in the primary control level is evaluated in three cases, a) base (conventional droop controller), b) DVFC, c) delay-based DVFC. Time delay is set at τ^m=20 ms. It is noteworthy that communication delay in this chapter is applied on the mid-level controller which uses distributed variables $(\Omega_i(t), e_i(t))$. Therefore, comparison of DVFC with conventional UC is not suitable to show delay impact on system performance. As mentioned in Section 4.1, the proposed DVFC is obtained from IPS model discussed in Chapter 3. IPS model is the similar to non-optimal DVFC with all utility function weights equal to zero (i.e., $w_x = 0, x \in \{\mathcal{F}, \mathcal{V}, \mathcal{C}, \mathcal{E}\}$). Therefore, it is expected that these control techniques demonstrate similar performances in presence of communication delay. Simulation results in Chapter 4 proved that optimal performance of DVFC mitigates frequency and voltage deviation in load change or renewable energy intermittency. However, it does not affect on frequency and voltage oscillation less than mid-level time interval (i.e., 0.5 s). As mentioned in Section 5.1, a new constraint for delay control is added to stability critic network. Thus, this chapter evaluates delay impact on frequency, voltage, and power sharing in case of DVFC with and without control delay. Figure 5.10 depicts that the DVFC eliminates frequency deviation while the base approach cannot restore frequency to the nominal value. Observe that there is no frequency oscillation in the base approach because conventional droop controller does not use the distributed variables $(\Omega_i(t))$. Time delay increases frequency oscillation resulting from load disconnection at bus #4. Figure 5.10 shows that delay-based DVFC improves the dominant eigenvalue damping from 0.39 to 0.52. It is noteworthy to mention that, when time delay increases to τ=30 ms and τ=40 ms, frequency oscillation magnitude increases.

Figure 5.11 illustrates comparison of the DVFC with and without delay control design for DG_1. The base approach is not analyzed because there is no significant oscillation due to time delay effect. The delay-based DVFC consumes 43% energy less than that of DVFC as depicted in Figure 5.11 in the duration of 2 s.

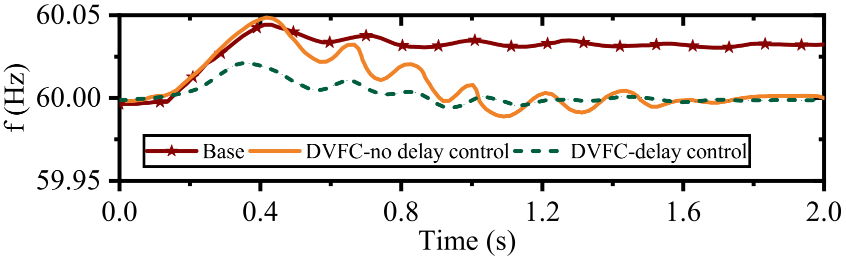

Figure 5.10: MG frequency response in case of the base and DVFC approach with and without delay control subject a load disconnection at bus #4.

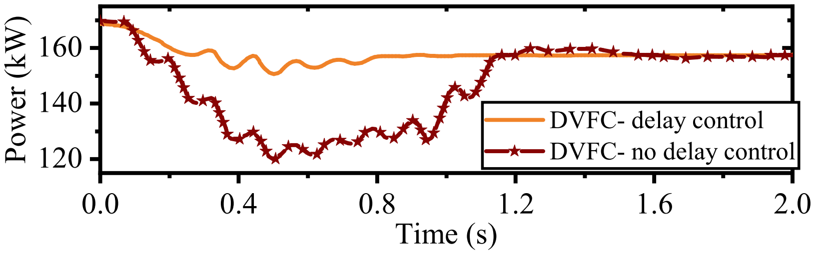

Figure 5.11: Delay impact on active power of DG_1 in a 50 kW-load disconnection at bus #4.

5.4.2 Time-Varying Delay-based DVFC under Small Perturbation

The proposed small-signal DVFC evaluates MG stability for constant time delays. This analysis is a starting point to show a direction for dealing with time delays in the mid-level control of MGs. Practically, time-variance is a characteristic of communication delays. We evaluate the DVFC performance for a time-varying delay in three cases as follows:

- Case 1: $\tau_1^m(t) = 0.02 + 0.02sin(10t)$, $\underline{\tau}^m = 0, \overline{\tau}^m = 40\,ms.$
- Case 2: $\tau_2^m(t) = 0.04 + 0.02sin(10t)$, $\underline{\tau}^m = 20\,ms, \overline{\tau}^m = 60\,ms.$
- Case 3: $\tau_3^m(t) = 0.04 + 0.03sin(10t)$, $\underline{\tau}^m = 10\,ms, \overline{\tau}^m = 70\,ms.$

Constant matrix in (6.11b), H, is achieved from trial and error (e.g., $h_{11} = 0.015, h_{22} = 0.017$). This matrix satisfies the SSG condition under small perturbations up to 250 kVA. Figure 5.12 illustrates dominant eigenvalue of the DVFC with and without delay control.

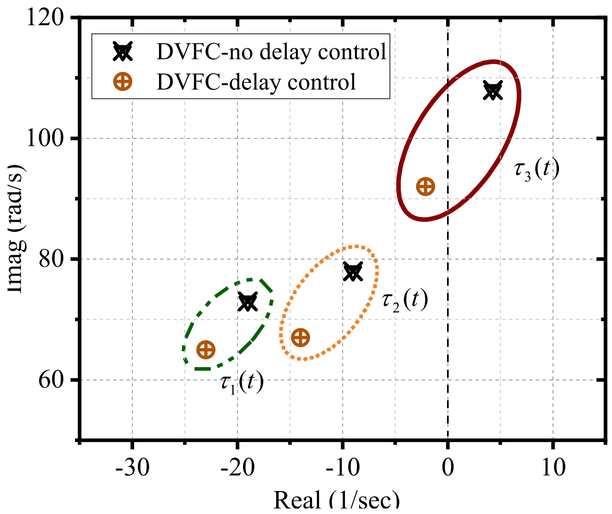

Figure 5.12: Dominant eigenvalues in the DVFC with and without delay control under time-varying delays of three cases.

Increased magnitude of time delay, in Cases 1 and 2, leads to more frequency oscillation and, in severe Case 3, can result in MG instability. Table 5.2 reveals the deterioration of DVFC performance in damping of time-varying delay impact on MG frequency. Comparing Cases 2 and 3 shows that dominant eigenvalues move towards the right-side of root locus coordination as magnitude of time-varying delay increases from 0.02 to 0.03. Delay-based controller stabilizes the frequency controller in case 3 even though frequency oscillation is not desirable (delay-based controller: damping value, ξ_c=0.03).

It is essential to consider time-varying delay in the DVFC control design. As a result,

Table 5.2: Dominant eigenvalue damping around nominal operation under time-varying delay

Controller	Case 1	Case 2	Case 3
DVFC	0.22	0.11	-
Delay-based DVFC	0.34	0.20	0.03

MG frequency maintains stable even in the case of large time delay ($\tau_3(t)$). In addition, damping parameter, ξ_c, is improved from 0.22 to 0.34 in case 1 and from 0.11 to 0.2 in case 2. Time-domain analysis is exactly similar to the one presented for constant delay.

To analyze how the delay-based DVFC reduces frequency and voltage deviation, we defined frequency performance index $\mathrm{PI}_f = (\int_0^2 |\omega(t) - \omega_0| dt)/\omega_0$ and voltage performance index

Table 5.3: Frequency and voltage performance of the delay-based DVFC in time-varying delays

	PI_f			PI_v		
	Case 1	Case 2	Case 3	Case 1	Case 2	Case 3
DVFC	0.00030	0.00042	0.0112	0.009	0.012	0.13
delay-based DVFC	0.00018	0.00028	0.0035	0.006	0.010	0.10

$\text{PI}_v = \sum_{i\in\{1,3,4,6\}}(\int_0^2 |V_i(t) - V_{i0}|dt)/V_{i0}$ to compare the DVFC with and without delay. $\omega_0(t)$ and $V_{i0}(t)$ are frequency and voltage time-domain profile when DVFC performs in a similar but zero-delay case. Table 5.5 shows performance improvement of the delay-based DVFC to other controller. Nevertheless, as communication delay increases, the frequency index, PI_f, obtained from the delay-based DVFC becomes considerably lower than that achieved from the DVFC. A similar observation applies the voltage performance index in Table 5.3.

5.4.3 Constant Delay-based DVFC under Large Perturbation

Although designed gain values of DVFC in small-signal model maintains MG stability, it is valid only around operating points. A large perturbation such as connection of 900-kVA with power factor 0.9 load at t=0.4 s is added to total load in the modified CIGRE test case in Figure 5.6.

We consider three cases of the base approach, DVFC with and without delay control. Figures 5.13 and 5.14 show frequency and output voltage response of MG in presence of this large disturbance. During t=0.4-3.5 s, frequency is restored to the nominal value under action of the DVFC. Steady-state frequency in the DVFC performance is 377 rad/s, while the base approach regulates steady-state frequency at 376.23 rad/s. After connection of loads, both frequency $\omega_i(t)$ and output voltage $V_{di}(t)$ move towards different values less than their nominal values. Output voltage of generation units converges to different constants ranging from 0.95 to 1 p.u., while output frequency of each DG converges to the same value. This is because the frequency is a global phenomenon in MG, but output voltage is local. However, this CIGRE test system is small which leads the voltage of each bus converging to a same value. Voltage profile of four buses in the base approach remains on 0.94 p.u. which is under the allowable range according to IEEE 1547 [3]. Figure 5.15 depicts that output voltage at four buses is restored to the nominal value after 2 s. Figure 5.16 shows that output active and reactive power of four DGs. During t=0.4-4 s,

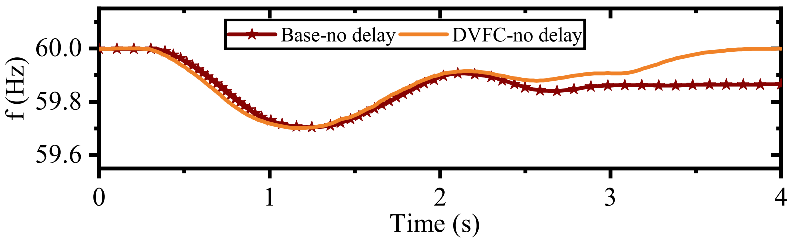

Figure 5.13: MG frequency response before, during, and after a 900-kVA load connection (no delay).

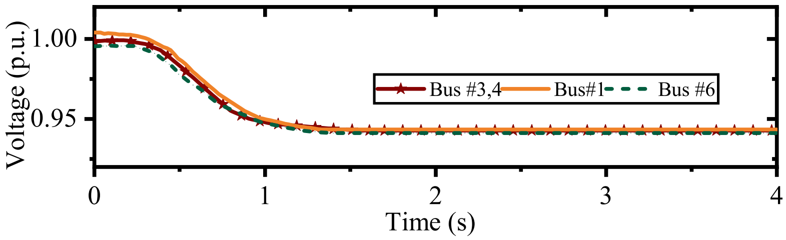

Figure 5.14: Output voltage of generation buses in the base approach in a 900 kVA-load connection.

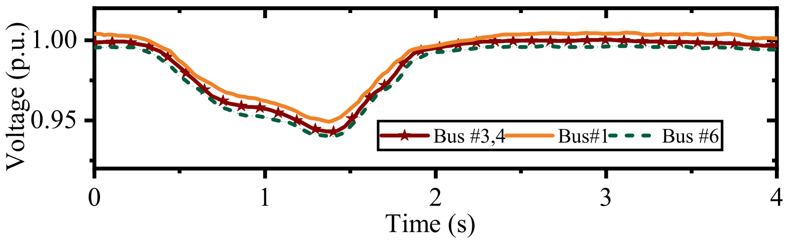

Figure 5.15: Performance of the DVFC in voltage control in the presence of a 900 kVA-load connection.

increased output active and reactive power of total DGs should be equal to added load to ensure demand and supply balance. The base approach shares active and reactive power no matter how much $DG_{4,6}$ are close to their rated power. Two DGs connected to buses #4 and #6 generate 145 kW and two other DGs produce 110 kW, which are less than active

Table 5.4: Participation factor of DGs in active and reactive power sharing (no delay) at t=4 s

	Active Power (%)			Reactive Power (%)		
	DG$_{1,3}$	DG$_{4,6}$	Uncovered Demand	DG$_{1,3}$	DG$_{4,6}$	Uncovered Demand
Base	28.28	37.28	34.44	21.59	33.71	44.77
DVFC	56.81	43.19	0	50.38	49.62	0

power of the increased load. This inadequacy of active power is a reason for frequency deviation of the base approach in Figure 5.16. Figure 5.17 illustrates output active and reactive power using the DVFC with no delay effect. Comparing with the base approach, it is observed that the increased active power for two DGs on buses #1 and #3, which have enough capacity different from two other DGs, are around 221 kW, while DGs at buses #4 and #6 generate 168 kW. Table 5.4 shows participation factor of DG$_{1,3}$ increases from 28% in the base approach to 56% in the DVFC, because these DGs have more operating power capabilities comparing to DG$_{4,6}$. Similar convention is applied to reactive power sharing among these DGs. Figure 5.18 illustrates impact of communication delays on MG frequency. The constant communication delay, τ^m=10 ms, causes low oscillation around ideal frequency response shown in Figure 5.13. From Figure 5.18, we can observe that the delay-based DVFC damps oscillation of frequency response. This analysis can be applied to voltage, active and reactive time-domain simulation in Figures 5.19 and 5.20. The delay-based DVFC damps voltage, active and reactive power profiles similar to those in

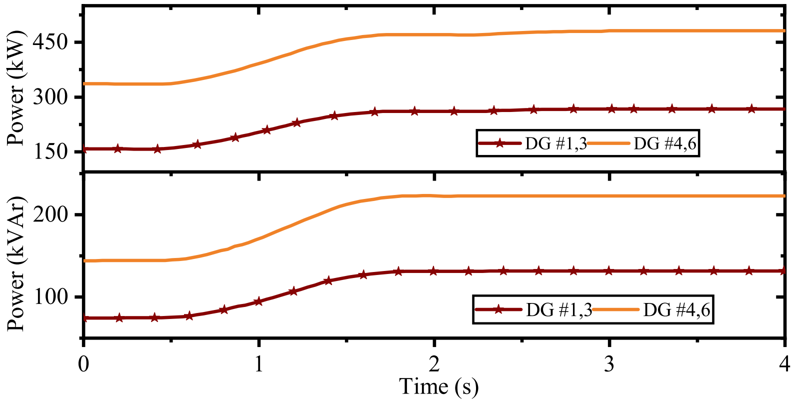

Figure 5.16: Active and reactive power sharing among DGs in the base approach (no delay) in large perturbation.

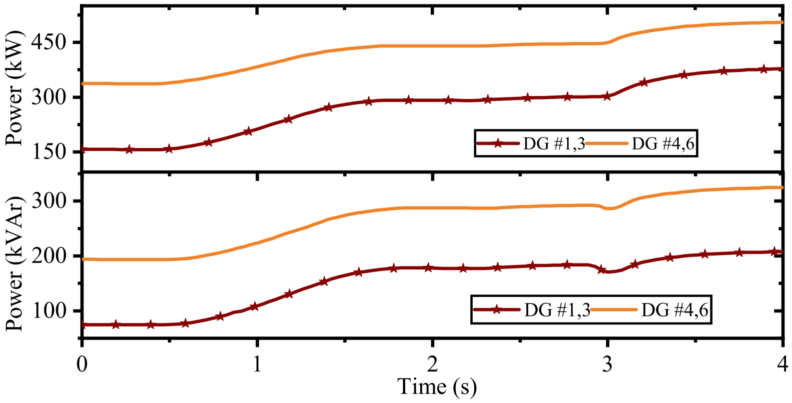

Figure 5.17: Active and reactive power sharing among DGs in the DVFC (no delay).

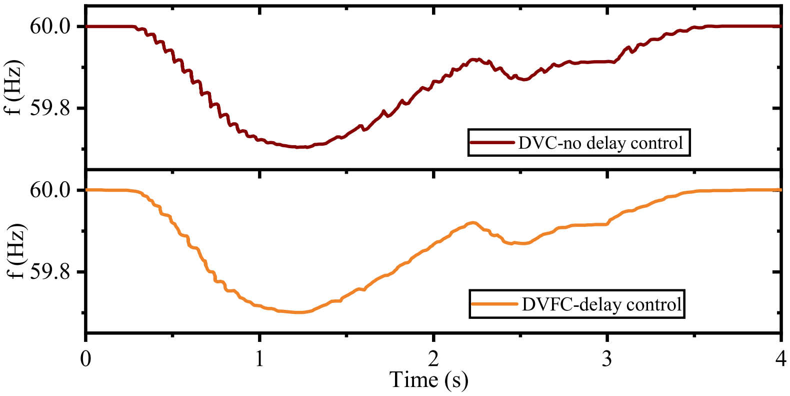

Figure 5.18: Frequency response of the DVFC with and without delay control in τ=10 ms subject to large disturbance at t=0.4 s.

Figures 5.15 and 5.17, respectively. As observed in these figures, MG frequency is more sensitive to communication delay than voltage, active and reactive power of DGs. As a result, we continue the time delay analysis on only frequency in different cases. As time delay increases up to 30 ms in Figure 5.21, MG frequency response has more ripples than that obtained in time delay of 10 ms. To evaluate activation of LMI-form presented in (5.23), we increase time delay to 75 ms which is more than a normal time delay margin (69 ms). From results shown in Figure 5.22, it can be concluded that the DVFC cannot be used because of frequency instability at τ^m=75 ms, while the delay-based DVFC can regulate frequency even with a delay more than t=40 ms. The delay-based DVFC remains

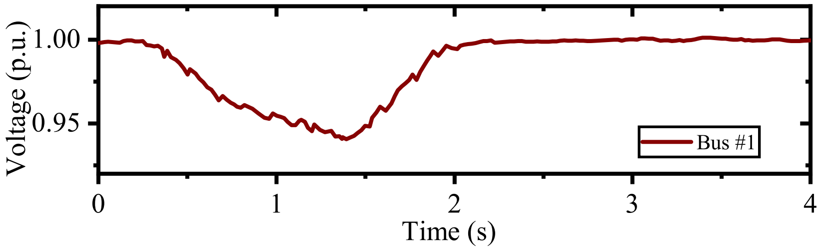

Figure 5.19: The voltage profile at bus #1 for the DVFC without delay control in τ^m=10 ms.

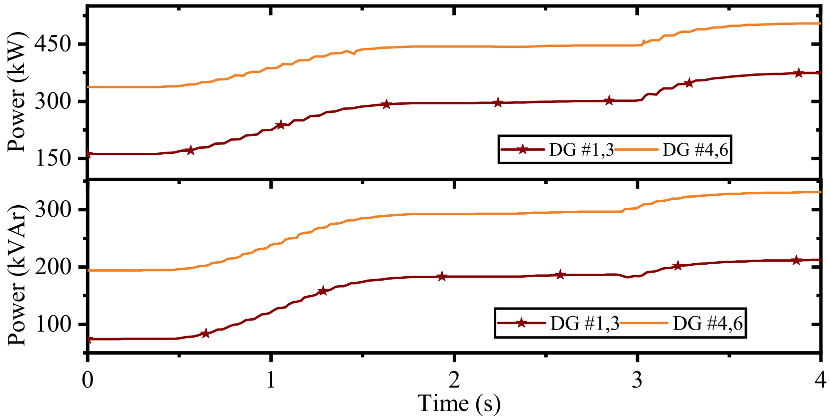

Figure 5.20: Performance of the DVFC without delay control in active and reactive power sharing among four DGs in τ^m=10 ms.

stable with communication delay less than 94 ms, achieved from a trial and error analysis. Table 5.5 shows superiority of the delay-based DVFC to other controllers. Nevertheless, as communication delay increases, frequency performance index, PI_f, obtained from the delay-based DVFC becomes considerably lower than that achieved from the DVFC. This delay-based controller reduces frequency deviation index to around 30% of that of the DVFC. Although a large time delay, τ^m=75 ms, causes frequency instability, the frequency performance index is 0.014 in time horizon of 4 s. A similar convention is applied to the voltage performance index as depicted in Table 5.5. Table 5.6 lists the typical convergence times for each NN, performed by Intel(R) Core(TM) i7-8650 1.90GHz (4 processors). This table depicts that the proposed DVFC with delay control increases computation time for training of action and critic networks due to rejection or acceptance of action variables.

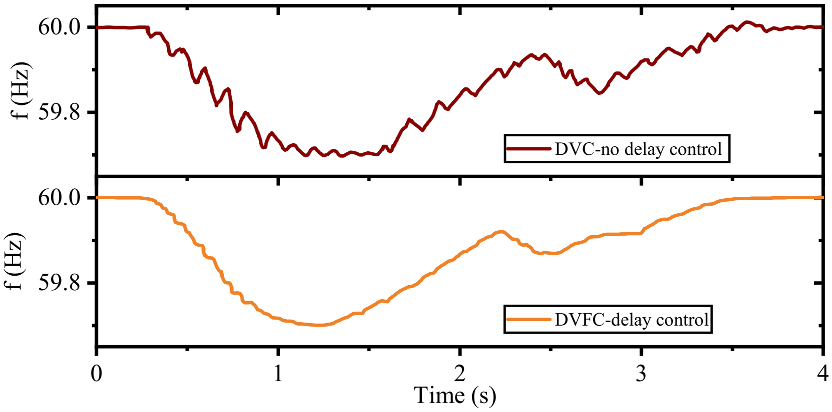

Figure 5.21: Frequency response of the DVFC with and without delay control in τ^m=30 ms.

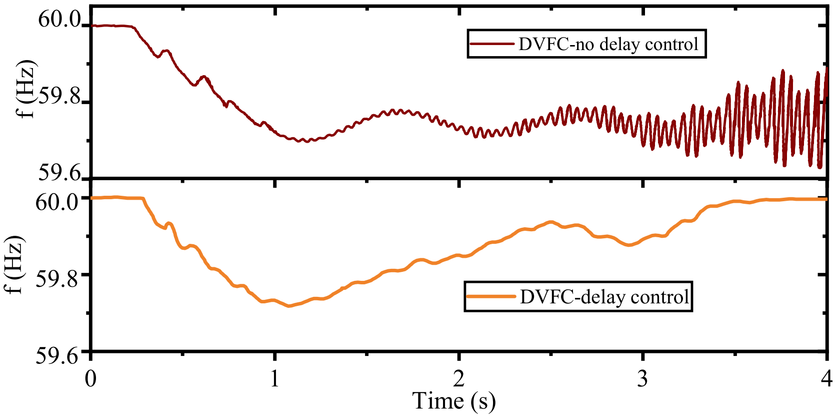

Figure 5.22: Frequency response of the DVFC with and without delay control in τ^m=75 ms.

Table 5.5: Frequency and voltage performance of the delay-based DVFC under different time delays

	PI_f			PI_v		
	$\tau^m = 10ms$	$\tau^m = 30ms$	$\tau^m = 75ms$	$\tau^m = 10ms$	$\tau^m = 30ms$	$\tau^m = 75ms$
DVFC	0.0018	0.0038	0.014	0.04	0.06	0.12
Proposed DVFC	0.0005	0.0013	0.005	0.01	0.05	0.07

Besides, time response of ADHDP controller for both approaches are equal.

Table 5.6: Typical convergence time for NNs in DVFC with and without delay control

	Training Cycle	Model	Action	Critic
DVFC	10 μs	175 s	225 s	650 s
Proposed DVFC	10 μs	180 s	270 s	833 s

5.4.4 Time-Varying Delay-based DVFC under Large Perturbation

In this study, extensive simulations have been carried out to evaluate impact of communication delays on the MG transient performance. Performance of delay-based DVFC under large perturbations is evaluated in two time-varying delays:

- Case 1: $\tau_1^m(t) = 0.02 + 0.02sin(10t)$, $\underline{\tau}^m = 0$, $\overline{\tau}^m = 40\,ms$.
- Case 2: $\tau_2^m(t) = 0.035 + 0.035sin(10t)$, $\underline{\tau}^m = 0$, $\overline{\tau}^m = 70\,ms$.

The time-domain simulation in this study shows very similar oscillating behaviour to those with constant time delays discussed in the previous subsection. As a result, we analyze convergence of diffusive variables for frequency ($\Omega_i(t)$) and voltage ($e_i(t)$) under various time-varying delays.

We assume that only DG$_1$ has access to reference values of the diffusive variable ($\Omega_1(t)$) as a virtual leader. Other DGs need to communicate with their neighbours and converge to a single diffusive value ($\Omega_i(t) = \Omega_j(t), \forall i \neq j$).

Figure 5.23 compares convergence of frequency diffusive control variable for four DGs in the DVFC with and without delay control. As seen in this figure, control performance in the delay-based DVFC is better than that obtained from the DVFC. From this perspective, the same analysis is performed on the voltage control variable for four DGs. As observed in Figure 5.24, voltage control variables in the delay-based DVFC show less oscillating behaviour than that obtained from the DVFC, when the delay fluctuates between 0 and 40 ms. With comparison of Figures 5.23 and 5.24, it is concluded that time delay has less impact on voltage profile than frequency response. Since upper bound values of time-varying delays affect frequency control performance, we are interested in simulating the delay-based DVFC with a larger time-varying delay. Therefore, we continue to increase the magnitude of delay in Case 1 to two times its value. As depicted in Figure 5.25,

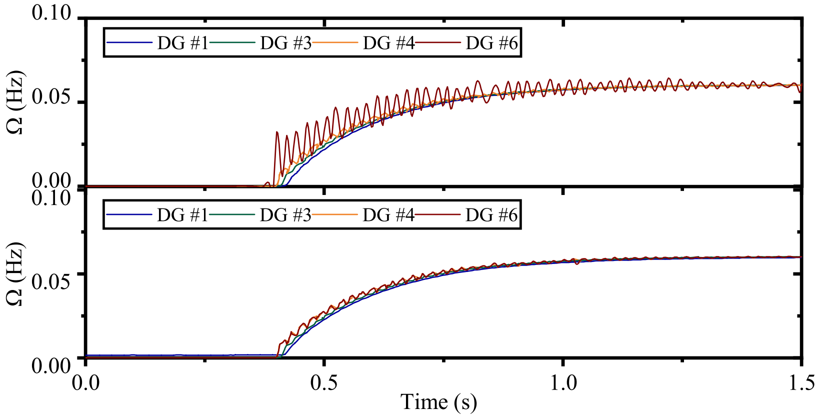

Figure 5.23: Transient response of frequency diffusive variable ($\Omega_i(t)$) under small time-varying delay (Case1) for DVFC with and without delay control.

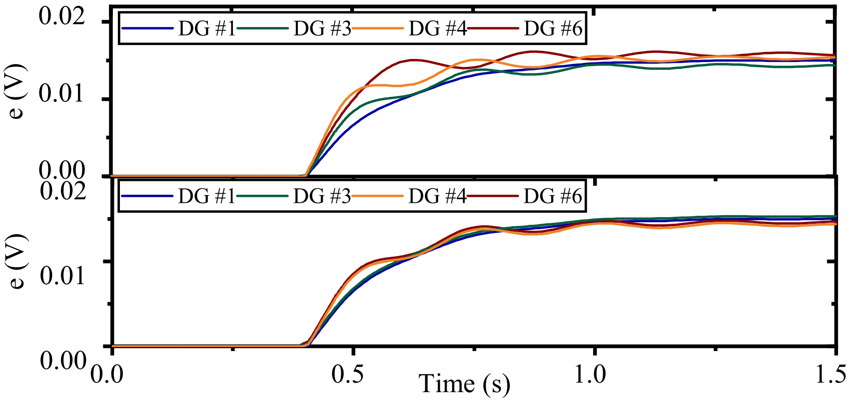

Figure 5.24: Transient response of voltage diffusive variable ($e_i(t)$) under small time-varying delay (Case1) for DVFC with and without delay control.

increasing time-varying delay ruins MG stability. The delay-based DVFC activates LMI format presented in (5.29) to avoid frequency instability, subject to a large time delay. It can be concluded that the delay-based DVFC is robust to large time-varying delay, while the DVFC with no delay control is vulnerable to large variant delays. In addition, comparing Figures 5.23 and 5.25 shows that large time-varying delay can postpone convergence of the frequency control variable. Table 5.7 shows effectiveness of the delay-based DVFC in the frequency and voltage performance indices. As a result, the delay-based DVFC can effectively characterize the actual time-varying delay under large perturbations.

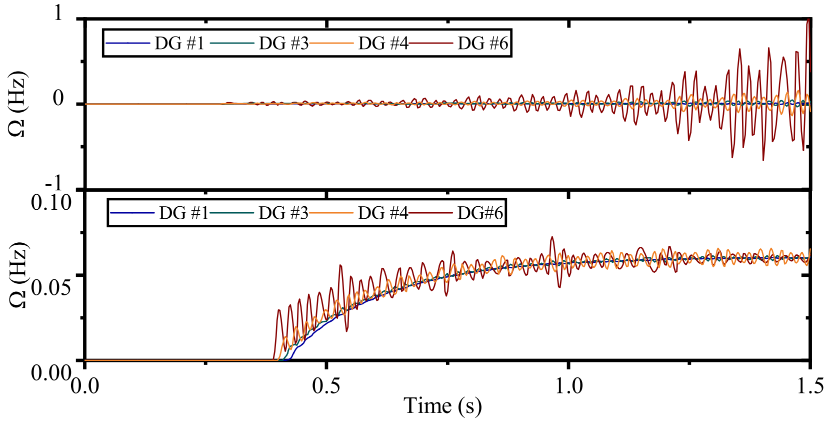

Figure 5.25: Transient response of frequency diffusive variable ($\Omega_i(t)$) under large time-varying delay (Case2) for DVFC with and without delay control.

Table 5.7: Frequency and voltage performance of the delay-based DVFC under different time delays

	PI_f		PI_v	
	Case 1	Case 2	Case 1	Case 2
DVFC	0.0068	0.015	0.07	0.16
delay-based DVFC	0.0032	0.006	0.04	0.10

5.5 Summary

This chapter presents how the communication time delays affect the mid-level frequency and voltage control of an islanded MG proposed in Chapter 4. Practically, constant and time-varying communication delays caused generation units to use outdated dispatch information for power sharing. Two models of constant and time-varying delay-based DVFC are proposed to determine time delay margin in the mid-level controller where time delay below this margin guarantees MG stability. Based on a comprehensive analysis of the DVFC gains, frequency and voltage controllers can be stable even in case of large time delays. Results from CIGRE MG show better damp frequency oscillations with delay-based DVFC. To counteract delay impact on frequency and voltage of MG subject to large perturbations, two LMI-forms of constant and time-varying delays are applied on the mid-level control design. As communication delay increases, large-signal model of DVFC changes feasible gain set of the delay-based DVFC. Numerical results demonstrate a better frequency and voltage regulation of the delay-based DVFC in both constant and time-varying delays compared to the DVFC without delay control. It is concluded that the delay-based DVFC is less sensitive to the communication delay than that of the DVFC presented in Chapter 4.

Chapter 6

Conclusions and Future Work

6.1 Conclusions

This Ph.D research investigates problems in frequency and voltage control of islanded MGs. From the primary control perspective, an intelligent power sharing mechanism is proposed to maintain the frequency and voltage within acceptable ranges. It shares power among generation units not only based on their droop values but also their operating power capabilities. From the secondary control perspective, a hybrid mid-level controller is presented that communicates with a distributed primary controller to share the output power of generation units. It also determines the optimal output power of units between two dispatch intervals for the secondary controller while maintaining frequency and voltage stability. This mid-level controller covers time intervals between those of primary and secondary controllers, and avoids the stair-pattern generation scheduling in conventional UCs. It reduces operating cost of MG and life-cycle degradation of fast-acting generation units. To consider a realistic test case, a comprehensive investigation of communication delay impacts is performed on frequency and voltage response of islanded MGs. Constant and time-varying delays are considered in control design of the proposed mid-level controller. Finally, a delay-based controller is designed to mitigate frequency oscillation of MGs in presence of either small or large perturbations.

In Chapter 1, a literature survey on islanded MGs and challenges in the frequency and voltage control is presented. Control of islanded MGs is categorized in aspect of a) functionality, b) technique and c) architecture. A review of MG architectures, control techniques, stability models, and control levels is presented in this chapter. Frequency and voltage control challenges are mainly categorized as a) primary frequency and voltage control, b) optimal operation and secondary control, and c) impact of time delay on both primary and secondary controls. In addition, frequency and voltage control issues existing in primary and secondary control levels with and without communication delay are described.

In Chapter 2, modelling of an islanded MG with main components is discussed. Three main components are considered: 1) inverter-based generation unit, 2) SG, and 3) voltage-dependent load. Frequency and voltage control diagrams of inverter-based units and SGs with corresponding equations are presented. In the case of inverter-based unit, a virtual impedance is added to the voltage control diagram to regulate output voltage.

In Chapter 3, an intelligent power sharing (IPS) controller is proposed for islanded MGs. Based on realistic analysis and simulation results, the IPS controller provides desirable frequency and voltage regulation, while sharing power proportional to generation units' operating power capabilities and their droop control values. The IPS controller gains can be tuned to achieve either voltage regulation, reactive power sharing, or a compromise between them. A mathematical model of small-perturbation stability is presented along with performance analysis. By properly tuning the changes in IPS parameters, it is demonstrated that the IPS provides zero steady-state errors in MG frequency and voltage, unlike conventional control models. This controller reduces dependency on ESSs by distributing operating power capabilities of generation units over a wide time-horizon.

In Chapter 4, a dynamic voltage and frequency controller is proposed for optimizing the operating cost of dispatchable units and ESS life-time in an islanded MG. Numerical results show that the DVFC can regulate frequency and voltage of MG as a mid-level controller. This mid-level controller covers the time intervals between those of primary and secondary controllers and avoids stair-pattern generation scheduling in conventional UCs. Through studying several scenarios on a CIGRE test system, it is shown that the DVFC reduces frequency and voltage deviations from their desired values, and minimizes operating cost of generation units. Its optimal control policy extends the life-cycle of ESSs up to twofold. With proper training and parameter configuration of the DVFC, islanded MGs can be controlled intelligently to be self-adaptive, stable, and cost-efficient.

In Chapter 5, impacts of communication time delays on mid-level frequency and voltage control, proposed in Chapter 4, are discussed. Two models of constant and time-varying delay-based DVFC are proposed to determine time delay margin in the mid-level controller where time delay below this margin guarantees MG stability. By conducting a comprehensive analysis of DVFC gains, it is concluded that the MG frequency and voltage controllers remain stable even under large time delays. Numerical results illustrate that better frequency and voltage regulation under both constant and time-varying delay scenarios is achieved compared to the DVFC without delay control.

6.2 Contributions

The main contributions of this thesis are listed as follows:

- An IPS approach is developed that allows for dispatching active and reactive power among generation units based on their droop control gains and operating power capabilities. It improves frequency and voltage regulation and enhances life-cycle of fast-acting generation units. In addition, it offers a dynamic compromise between voltage regulation and accurate reactive power sharing among generation units and the controlled impact of coupling between active and reactive power on voltage regulation.
- A small-perturbation stability model is analyzed to determine required conditions for the proposed controller gains. The analysis leads to robust controller performance under rapid load and renewable energy variations while maintaining MG frequency and voltage stability.
- A hybrid mid-level controller is developed that communicates with the proposed primary controller to share output power of generation units. It also determines optimal output power of units between two dispatch intervals for the secondary controller while maintaining frequency and voltage stability. This voltage and frequency controller is tested on the CIGRE test system to evaluate its economic operation and ESS life-cycle efficiency compared to conventional UC.
- The impact of constant and time-varying delay is evaluated on the proposed controller in presence of small and large perturbations. Two mathematical models are developed for small and large-signal analysis of islanded MGs.
- A delay-based controller is developed to mitigate frequency oscillation of the islanded MG in subject to small and large disturbances when delays are either constant or time-varying. The proposed controller reduces delay impacts by increasing time delay margin and MG frequency oscillation resulted from the delay.

6.3 Future Research Topics

Future research topics can be carried out to address the following drawbacks:

- The proposed IPS is tested on only balanced test systems while it should be analyzed under the unbalanced conditions. One phase-disconnection of line or load may cause MG instability which needs to be investigated.
- The cost-to-go function, presented in Chapter 4, uses constant weights for each utility function as a simple weighted sum method. In theory, it is not a multi-objective optimization algorithm. It can be equipped with proper multi-objective algorithms such as genetic or particle swarm optimization techniques.
- The randomness of delay is another characteristic of communication delay. There is probability of having delay in communication links, which should be considered in a robust control design. For this purpose, some studies have proposed different algorithms to handle this issue [92]. Therefore, it is an open area to consider a randomly time-varying delay in a control design formulation and to deeply analyze its impact on controller performance.
- Constant and time-varying delays are considered to be equal for all communication links. Practically, the length and technology types of communication networks between the LC-to-LC affect the corresponding delay. Hence, a comprehensive analysis is necessary for studying the impact of unequal constant and time-varying delays in communication network. Note that, apart from time delays, both the topology structure and adjacency weights of the selected communication networks also affect MG stability.
- The proposed delay-based controller can be extended to a voltage energy function in large signal analysis. When applying Lyapunov-Krasvoskii formulation to the DVFC with communication delays, it is necessary to analyze voltage stability of a large-scale MG subject to large perturbations.
- SGs have an intrinsic time delay in their system control, which can be added to communication delay. Studies should be carried out to develop a robust controller

considering both system control delay and communication latency. Moreover, analysis of communication delay for secondary controller can improve the model presented in this study.

References

[1] W. Su and J. Wang, “Energy management systems in microgrid operations,” *Electricity Journal*, vol. 25, no. 8, pp. 45–60, Oct. 2012.

[2] J. Eto, R. Lasseter, B. Schenkman, J. Stevens, D. Klapp, H. VolkommeRr, E. Linton, H. Hurtado, and J. Roy, “Overview of the CERTS microgrid laboratory test bed,” *2009 CIGRE/IEEE PES Joint Symposium Integration of Wide-Scale Renewable Resources into the Power Delivery System*, pp. 1–1, 2009.

[3] *IEEE Guide for Design, Operation, and Integration of Distributed Resource Island Systems with Electric Power Systems*, IEEE Std. 1547.4, 2011.

[4] M. S. Mahmoud, *Microgrid: Advanced Control Methods and Renewable Energy System Integration.* Elsevier, 2016.

[5] A. Pappachen and A. P. Fathima, “Critical research areas on load frequency control issues in a deregulated power system: A state-of-the-art-of-review,” *Renewable and Sustainable Energy Reviews*, vol. 72, pp. 163–177, May 2017.

[6] M. Farrokhabadi, “Primary and secondary frequency control techniques for isolated microgrids,” *Ph.D. Dissertation*, University of Waterloo, Waterloo, ON, 2017.

[7] M.-H. Khooban, T. Niknam, F. Blaabjerg, P. Davari, and T. Dragicevic, “A robust adaptive load frequency control for micro-grids,” *ISA Transactions*, vol. 65, pp. 220–229, Nov. 2016.

[8] N. Rezaei, A. Ahmadi, A. H. Khazali, and J. M. Guerrero, “Energy and frequency hierarchical management system using information gap decision theory for islanded microgrids,” *IEEE Transactions on Industrial Electronics*, vol. 65, no. 10, pp. 7921–7932, Oct. 2018.

[9] M. Farrokhabadi, C. A. Canizares, and K. Bhattacharya, “Unit commitment for isolated microgrids considering frequency control,” *IEEE Transactions on Smart Grid*, vol. 9, no. 4, pp. 3270–3280, Jul. 2018.

[10] M. M. A. Abdelaziz, M. F. Shaaban, H. E. Farag, and E. F. El-Saadany, “A multistage centralized control scheme for islanded microgrids with PEVs,” *IEEE Transactions on Sustainable Energy*, vol. 5, no. 3, pp. 927–937, Jul. 2014.

[11] J. W. Simpson-Porco, Q. Shafiee, F. Dorfler, J. C. Vasquez, J. M. Guerrero, and F. Bullo, "Secondary frequency and voltage control of islanded microgrids via distributed averaging," *IEEE Transactions on Industrial Electronics*, vol. 62, no. 11, pp. 7025–7038, Nov. 2015.

[12] S. Liu, P. X. Liu, and X. Wang, "Stability analysis and compensation of network-induced delays in communication-based power system control: A survey," *ISA Transactions*, vol. 66, pp. 143–153, Jan. 2017.

[13] M. Emmanuel and R. Rayudu, "Communication technologies for smart grid applications: A survey," *Journal of Network and Computer Applications*, vol. 74, pp. 133–148, Oct. 2016.

[14] G. Lou, W. Gu, Y. Xu, W. Jin, and X. Du, "Stability robustness for secondary voltage control in autonomous microgrids with consideration of communication delays," *IEEE Transactions on Power Systems*, vol. 33, no. 4, pp. 4164–4178, Jul. 2018.

[15] T. Khalili, M. T. Hagh, S. G. Zadeh, and S. Maleki, "Optimal reliable and resilient construction of dynamic self-adequate multi-microgrids under large-scale events," *IET Renewable Power Generation*, vol. 13, no. 10, pp. 1750–1760, Feb. 2019.

[16] L. Meng, E. R. Sanseverino, A. Luna, T. Dragicevic, J. C. Vasquez, and J. M. Guerrero, "Microgrid supervisory controllers and energy management systems: A literature review," *Renewable and Sustainable Energy Reviews*, vol. 60, pp. 1263–1273, Jul. 2016.

[17] e. Olivares, Daniel E, "Trends in microgrid control," *IEEE Transactions on Smart grid*, vol. 5, no. 4, pp. 1905–1919, Jul. 2014.

[18] A. Bidram and A. Davoudi, "Hierarchical structure of microgrids control system," *IEEE Transactions on Smart Grid*, vol. 3, no. 4, pp. 1963–1976, Dec. 2012.

[19] F. Katiraei, R. Iravani, N. Hatziargyriou, and A. Dimeas, "Microgrids management," *IEEE Power and Energy Magazine*, vol. 6, no. 3, Jun. 2008.

[20] J. P. Lopes, C. L. Moreira, and A. G. Madureira, "Defining control strategies for microgrids islanded operation," *IEEE Transactions on Power Systems*, vol. 21, no. 2, pp. 916–924, May 2006.

[21] I. Usunariz, M. Santamaria, K. Mentesidi, and M. Aguado, "A modified control scheme of droop-based converters for power stability analysis in microgrids," *Journal of Solar Energy*, vol. 2015, pp. 1–11, Nov. 2015.

[22] L. I. Minchala-Avila, L. E. Garza-Castanon, A. Vargas-Martinez, and Y. Zhang, "A review of optimal control techniques applied to the energy management and control of microgrids," *Procedia Computer Science*, vol. 52, pp. 780–787, Apr. 2015.

[23] S. Conti, R. Nicolosi, S. Rizzo, and H. Zeineldin, "Optimal dispatching of distributed generators and storage systems for MV islanded microgrids," *IEEE Transactions on Power Delivery*, vol. 27, no. 3, pp. 1243–1251, Jul. 2012.

[24] V. Nasirian, S. Moayedi, A. Davoudi, and F. L. Lewis, "Distributed cooperative control of DC microgrids," *IEEE Transactions on Power Electronics*, vol. 30, no. 4, pp. 2288–2303, Apr. 2015.

[25] L. Olatomiwa, S. Mekhilef, M. Ismail, and M. Moghavvemi, "Energy management strategies in hybrid renewable energy systems: A review," *Renewable and Sustainable Energy Reviews*, vol. 62, pp. 821–835, Sep. 2016.

[26] A. Werth, A. Andre, D. Kawamoto, T. Morita, S. Tajima, D. Yanagidaira, M. Tokoro, and K. Tanaka, "Peer-to-peer control system for DC microgrids," *IEEE Transactions on Smart Grid*, vol. 9, pp. 3667–3675, Dec. 2016.

[27] T. Khalili, A. Jafari, M. Abapour, and B. Mohammadi-Ivatloo, "Optimal battery technology selection and incentive-based demand response program utilization for reliability improvement of an insular microgrid," *Energy*, vol. 169, pp. 92–104, Jul. 2019.

[28] T. Khalili, S. Nojavan, and K. Zare, "Optimal performance of microgrid in the presence of demand response exchange: A stochastic multi-objective model," *Computers and Electrical Engineering*, vol. 74, pp. 429–450, Mar. 2019.

[29] A. Pappachen and A. P. Fathima, "Critical research areas on load frequency control issues in a deregulated power system: A state of art of review," *Renewable and Sustainable Energy Reviews*, vol. 72, pp. 163–177, May 2017.

[30] L. Huang, H. Xin, Z. Wang, L. Zhang, K. Wu, and J. Hu, "Transient stability analysis and control design of droop-controlled voltage source converters considering current limitation," *IEEE Transactions on Smart Grid*, vol. 10, no. 1, pp. 578–591, Jan. 2017.

[31] M. Farrokhabadi, C. A. Canizares, and K. Bhattacharya, "Frequency control in isolated/islanded microgrids through voltage regulation," *IEEE Transactions on Smart Grid*, vol. 8, no. 3, pp. 1185–1194, May 2017.

[32] Y. Khayat, Q. Shafiee, R. Heydari, M. Naderi, T. Dragicevic, J. W. Simpson-Porco, F. Dorfler, M. Fathi, F. Blaabjerg, and J. M. Guerrero, "On the secondary control architectures of AC microgrids: An overview," *IEEE Transactions on Power Electronics*, pp. 1–1, 2019.

[33] A. Maulik and D. Das, "Optimal operation of droop-controlled islanded microgrids," *IEEE Transactions on Sustainable Energy*, vol. 9, no. 3, pp. 1337–1348, Jul. 2018.

[34] M. M. A. Abdelaziz, H. E. Farag, and E. F. El-Saadany, "Optimum reconfiguration of droop-controlled islanded microgrids," *IEEE Transactions on Power Systems*, vol. 31, no. 3, pp. 2144–2153, May 2016.

[35] F. D. Mohammadi, H. K. Vanashi, and A. Feliachi, "State-space modeling, analysis, and distributed secondary frequency control of isolated microgrids," *IEEE Transactions on Energy Conversion*, vol. 33, no. 1, pp. 155–165, Mar. 2018.

[36] S. Roozbehani, M. T. Hagh, and S. G. Zadeh, "Frequency control of islanded wind-powered microgrid based on coordinated robust dynamic droop power sharing," *IET Generation, Transmission, and Distribution*, vol. 13, no. 21, pp. 4968–4977, Nov. 2019.

[37] M. Castilla, A. Camacho, J. Miret, M. Velasco, and P. Marti, "Local secondary control for inverter-based islanded microgrids with accurate active power sharing under high-load conditions," *IEEE Transactions on Industrial Electronics*, vol. 66, no. 4, pp. 2529–2539, Apr. 2019.

[38] B. John, A. Ghosh, and F. Zare, "Load sharing in medium voltage islanded microgrids with advanced angle droop control," *IEEE Transactions on Smart Grid*, vol. 9, no. 6, pp. 6461–6469, Nov. 2018.

[39] Z. Li, Z. Cheng, Y. Xu, Y. Wang, J. Liang, and J. Gao, "Hierarchical control of parallel voltage source inverters in AC microgrids," *Journal of Engineering*, vol. 2019, no. 16, pp. 1149–1152, Mar. 2019.

[40] T. V. Hoang and H. H. Lee, "An adaptive virtual impedance control scheme to eliminate the reactive power sharing errors in an islanding meshed microgrid," *IEEE Journal of Emerging and Selected Topics in Power Electronics*, vol. 6, no. 2, pp. 966–976, Jun. 2018.

[41] H. Mahmood, D. Michaelson, and J. Jiang, "Accurate reactive power sharing in an islanded microgrid using adaptive virtual impedances," *IEEE Transactions on Power Electronics*, vol. 30, no. 3, pp. 1605–1617, Mar. 2015.

[42] H. Zhang, S. Kim, Q. Sun, and J. Zhou, "Distributed adaptive virtual impedance control for accurate reactive power sharing based on consensus control in microgrids," *IEEE Transactions on Smart Grid*, vol. 8, no. 4, pp. 1749–1761, Jul. 2017.

[43] F. Zandi, B. Fani, I. Sadeghkhani, and A. Orakzadeh, "Adaptive complex virtual impedance control scheme for accurate reactive power sharing of inverter interfaced autonomous microgrids," *IET Generation, Transmission and Distribution*, vol. 12, no. 22, pp. 6021–6032, Dec. 2018.

[44] H. Liang and W. Zhuang, "Stochastic modeling and optimization in a microgrid: A survey," *Energies*, vol. 7, no. 4, pp. 2027–2050, Mar. 2014.

[45] L. Olatomiwa, S. Mekhilef, S. Shamshirband, and D. Petković, “Adaptive neuro-fuzzy approach for solar radiation prediction in Nigeria,” *Renewable and Sustainable Energy Reviews*, vol. 51, pp. 1784–1791, Oct. 2015.

[46] L. Barelli, G. Bidini, and F. Bonucci, “A micro-grid operation analysis for cost-effective battery energy storage and RES plants integration,” *Energy*, vol. 113, pp. 831–844, Oct. 2016.

[47] G. Liu, M. Starke, B. Xiao, and K. Tomsovic, “Robust optimisation-based microgrid scheduling with islanding constraints,” *IET Generation, Transmission and Distribution*, vol. 11, no. 7, pp. 1820–1828, Nov. 2017.

[48] G. Morales-Espana, A. Ramos, and J. Garcia-Gonzalez, “An MIP formulation for joint market-clearing of energy and reserves based on ramp scheduling,” *IEEE Transactions on Power Systems*, vol. 29, no. 1, pp. 476–488, Jan. 2014.

[49] A. Khodaei, “Microgrid optimal scheduling with multi-period islanding constraints,” *IEEE Transactions on Power Systems*, vol. 29, no. 3, pp. 1383–1392, May 2014.

[50] S. Upadhyay and M. Sharma, “Selection of a suitable energy management strategy for a hybrid energy system in a remote rural area of India,” *Energy*, vol. 94, pp. 352–366, Jan. 2016.

[51] G. Bruni, S. Cordiner, V. Mulone, V. Rocco, and F. Spagnolo, “A study on the energy management in domestic micro-grids based on model predictive control strategies,” *Energy Conversion and Management*, vol. 102, pp. 50–58, Sep. 2015.

[52] L. Jia and L. Tong, “Dynamic pricing and distributed energy management for demand response,” *IEEE Transactions on Smart Grid*, vol. 7, no. 2, pp. 1128–1136, Aug. 2016.

[53] M. Falahi, S. Lotfifard, M. Ehsani, and K. Butler-Purry, “Dynamic model predictive-based energy management of DG integrated distribution systems,” *IEEE Transactions on Power Delivery*, vol. 28, no. 4, pp. 2217–2227, Oct. 2013.

[54] A. M. Azmy and I. Erlich, “Online optimal management of pemfuel cells using neural networks,” *IEEE Transactions on Power Delivery*, vol. 20, no. 2, pp. 1051–1058, Jun. 2005.

[55] B.-G. Kim, Y. Zhang, M. van der Schaar, and J.-W. Lee, “Dynamic pricing for smart grid with reinforcement learning,” *Computer Communications Workshops (INFOCOM WKSHPS)*, pp. 640–645, 2014.

[56] G. K. Venayagamoorthy, R. K. Sharma, P. K. Gautam, and A. Ahmadi, “Dynamic energy management system for a smart microgrid,” *IEEE Transactions on Neural Networks and Learning Systems*, vol. 27, no. 8, pp. 1643–1656, Aug. 2016.

[57] V. P. Singh, N. Kishor, and P. Samuel, “Load frequency control with communication topology changes in smart grid,” *IEEE Transactions on Industrial Informatics*, vol. 12, no. 5, pp. 1943–1952, Oct. 2016.

[58] H. Liang, B. J. Choi, W. Zhuang, and X. Shen, “Stability enhancement of decentralized inverter control through wireless communications in microgrids,” *IEEE Transactions on Smart Grid*, vol. 4, no. 1, pp. 321–331, Mar. 2013.

[59] S. Liu, X. Wang, and P. X. Liu, “Impact of communication delays on secondary frequency control in an islanded microgrid,” *IEEE Transactions on Industrial Electronics*, vol. 62, no. 4, pp. 2021–2031, Apr. 2015.

[60] E. A. A. Coelho, D. Wu, J. M. Guerrero, J. C. Vasquez, T. Dragievi, V. Stefanovi, and P. Popovski, “Small-signal analysis of the microgrid secondary control considering a communication time delay,” *IEEE Transactions on Industrial Electronics*, vol. 63, no. 10, pp. 6257–6269, Oct. 2016.

[61] Q. Shafiee, C. Stefanovic, T. Dragicevic, P. Popovski, J. C. Vasquez, and J. M. Guerrero, “Robust networked control scheme for distributed secondary control of islanded microgrids,” *IEEE Transactions on Industrial Electronics*, vol. 61, no. 10, pp. 5363–5374, Oct. 2014.

[62] G. Chen and Z. Guo, “Distributed secondary and optimal active power sharing control for islanded microgrids with communication delays,” *IEEE Transactions on Smart Grid*, vol. 10, no. 2, pp. 2002–2014, Mar. 2019.

[63] A. J. S. J. Veronica, N. S. Kumar, and F. Gonzalez-Longatt, “Robust PI controller design for frequency stabilisation in a hybrid microgrid system considering parameter uncertainties and communication time delay,” *IET Generation, Transmission, and Distribution*, vol. 13, no. 14, pp. 3048–3056, Jul. 2019.

[64] G. Lou, W. Gu, J. Wang, W. Sheng, and L. Sun, “Optimal design for distributed secondary voltage control in islanded microgrids: Communication topology and controller,” *IEEE Transactions on Power Systems*, vol. 34, no. 2, pp. 968–981, Mar. 2019.

[65] H. Yan, X. Zhou, H. Zhang, F. Yang, and Z.-G. Wu, “A novel sliding mode estimation for microgrid control with communication time delays,” *IEEE Transactions on Smart Grid*, vol. 10, no. 2, pp. 1509–1520, Mar. 2019.

[66] C. Ahumada, R. Cardenas, D. Saez, and J. M. Guerrero, “Secondary control strategies for frequency restoration in islanded microgrids with consideration of communication delays,” *IEEE Transactions on Smart Grid*, vol. 7, no. 3, pp. 1430–1441, May 2016.

[67] P. Kundur, J. Paserba, V. Ajjarapu, G. Andersson, A. Bose, C. Canizares, N. Hatziargyriou, D. Hill, A. Stankovic, and C. Taylor, “Definition and classification of power system stability

ieee/cigre joint task force on stability terms and definitions," *IEEE Transactions on Power Systems*, vol. 19, no. 3, pp. 1387–1401, Aug. 2004.

[68] M. Farrokhabadi, C. A. Caizares, J. W. Simpson-Porco, E. Nasr, L. Fan, P. A. Mendoza-Araya, R. Tonkoski, U. Tamrakar, N. Hatziargyriou, and D. Lagos, "Microgrid stability definitions, analysis, and examples," *IEEE Transactions on Power Systems*, vol. 35, no. 1, pp. 13–29, Jan. 2020.

[69] M. Kabalan, P. Singh, and D. Niebur, "Large signal Lyapunov-based stability studies in microgrids: A review," *IEEE Transactions on Smart Grid*, vol. 8, no. 5, pp. 2287–2295, Sep. 2017.

[70] M. M. A. Abdelaziz, "New analysis and operational control algorithms for islanded microgrid systems," *Ph.D. Dissertation*, University of Waterloo, Waterloo, ON, 2014.

[71] S.-H. Hu, T.-L. Lee, C.-Y. Kuo, and J. Guerrero, "A riding-through technique for seamless transition between islanded and grid-connected modes of droop-controlled inverters," *Energies*, vol. 9, no. 9, p. 732, Sep. 2016.

[72] R. Moslemi and J. Mohammadpour, "Accurate reactive power control of autonomous microgrids using an adaptive virtual inductance loop," *Electric Power Systems Research*, vol. 129, pp. 142–149, Dec. 2015.

[73] L. B. Prasad, H. O. Gupta, and B. Tyagi, "Application of policy iteration technique based adaptive optimal control design for automatic voltage regulator of power system," *International Journal of Electrical Power and Energy Systems*, vol. 63, pp. 940–949, May 2014.

[74] P. Kundur, N. J. Balu, and M. G. Lauby, *Power System Stability and Control.* McGraw-hill New York, 1994.

[75] F. Mumtaz, M. H. Syed, M. A. Hosani, and H. H. Zeineldin, "A novel approach to solve power flow for islanded microgrids using modified Newton Raphson with droop control of DG," *IEEE Transactions on Sustainable Energy*, vol. 7, no. 2, pp. 493–503, Apr. 2016.

[76] N. Pogaku, M. Prodanovic, and T. C. Green, "Modeling, analysis and testing of autonomous operation of an inverter-based microgrid," *IEEE Transactions on Power Electronics*, vol. 22, no. 2, pp. 613–625, Mar. 2007.

[77] X. Tang, W. Deng, and Z. Qi, "Investigation of the dynamic stability of microgrid," *IEEE Transactions on Power Systems*, vol. 29, no. 2, pp. 698–706, Mar. 2014.

[78] P. C. Krause, *Analysis of Electric Machinery.* McGraw-Hill, 1986.

[79] "Hw43 600 kw (hewind)," *Wind Power, Tech. Rep. 2020 [Online]. Available: https://www.thewindpower.net/scripts /fpdf181/turbine.php?id=719.*

[80] J. Han, S. Khushalani-Solanki, J. Solanki, and J. Liang, "Adaptive critic design-based dynamic stochastic optimal control design for a microgrid with multiple renewable resources," *IEEE transactions on smart grid*, vol. 6, no. 6, pp. 2694–2703, Nov. 2015.

[81] J. Si, A. G. Barto, W. B. Powell, and D. Wunsch, *Handbook of learning and approximate dynamic programming.* John Wiley and Sons, 2004, vol. 2.

[82] B. Xu, A. Oudalov, A. Ulbig, G. Andersson, and D. S. Kirschen, "Modeling of lithium-ion battery degradation for cell life assessment," *IEEE Transactions on Smart Grid*, vol. 9, no. 2, pp. 1131–1140, Mar. 2018.

[83] R. E. Rosenthal, *GAMS- A User's Guide.* GAMS Development Corporation, 2016.

[84] Y. Yang, J. Wang, X. Guan, and Q. Zhai, "Subhourly unit commitment with feasible energy delivery constraints," *Applied Energy*, vol. 96, pp. 245–252, Aug. 2012.

[85] M. Parvizimosaed, F. Farmani, H. Monsef, and A. Rahimi-Kian, "A multi-stage smart energy management system under multiple uncertainties: A data mining approach," *Renewable Energy*, vol. 102, pp. 178–189, Mar. 2017.

[86] J. C. Keqin Gu and V. L. Kharitonov, *Stability of Time-Delay Systems.* Springer Science, 2003.

[87] R. Herzog and J. Keller, "Advanced control: An overview on robust control," *Master of Science Engineering*, vol. 6, pp. 14–20, Sep. 2009.

[88] R. Sipahi, T. Vyhldal, S.-I. Niculescu, and P. Pepe, *Time Delay Systems: Methods, Applications and New Trends.* Springer Science, 2012.

[89] L. Zhao, H. Gao, and H. R. Karimi, "Robust stability and stabilization of uncertain T-S fuzzy systems with time-varying delay: An input-output approach," *IEEE Transactions on Fuzzy Systems*, vol. 21, no. 5, pp. 883–897, Oct. 2013.

[90] M. Hazewinkel, *Positive-definite form.* Encyclopedia of Mathematics, Springer Science, 1994.

[91] J. Lai, H. Zhou, X. Lu, X. Yu, and W. Hu, "Droop-based distributed cooperative control for microgrids with time-varying delays," *IEEE Transactions on Smart Grid*, vol. 7, no. 4, pp. 1775–1789, Jul. 2016.

[92] S. Ci, J. Qian, D. Wu, and A. Keyhani, "Impact of wireless communication delay on load sharing among distributed generation systems through smart microgrids," *IEEE Wireless Communications*, vol. 19, no. 3, pp. 24–29, Jun. 2012.

Appendix A

Small-Signal Stability Analysis

In order to provide a better understanding of small-signal model, we consider following space-state model

$$\begin{aligned}\Delta \dot{x} &= A^{(g)}\Delta x + B^{(g)}\Delta u_x \\ \Delta y &= C^{(g)}\Delta x + C_y^{(g)}\Delta u_y, \qquad g \in \{p, v, c, lcl, INV, SG, Ld, Ln\}\end{aligned} \tag{A.1}$$

where $[\Delta u_x]$ and $[\Delta u_y]$ are input vectors, $[\Delta y]$ is output vector, and $[\Delta x]$ is state vector of components in power, voltage, and current controllers, LCL filter, and inverter, load, and line sub-modules. The complete formulation of small-signal model of each component in the MG is presented as follow:

A.1 Individual Voltage Source Inverter

A voltage source inverter is commonly used to interface units to a MG network. The power processing section of a three-leg voltage source inverter consists of power/voltage/current controllers, LCL filter, coupling inductance, and output on common reference coordinate. To describe state-space model of inverter, we define following d and q axis components of voltages and currents:

$$x_{s,dq} = [x_{s,d} \quad x_{s,q}]^T, \quad x \in \{v, i\}, \quad s \in \{o, l\}. \tag{A.2}$$

To connect an inverter to MG, output variables $x_{s,dq}$ need to be converted to the common reference coordinate (DQ). Axis set (DQ) is common reference frame rotating at frequency ω_{com}, while (dq_i) and (dq_j) are reference frame of the i^{th} and j^{th} inverters at ω_i and ω_j, respectively [58]. The following equation represents transformation from $dq-$coordinate to DQ axis for signals of

x_s and angle of inverter δ.

$$\begin{aligned} x_{s,DQ} &= T_{dq} x_{s,dq} + T_\delta \delta, \\ T_{dq} &= \begin{bmatrix} cos(\delta_i) & -sin(\delta_i) \\ sin(\delta_i) & cos(\delta_i) \end{bmatrix}, \\ T_\delta &= \begin{bmatrix} -x_{s,d} sin(\delta_i) - x_{s,q} cos(\delta_i) \\ x_{s,d} cos(\delta_i) - x_{s,q} sin(\delta_i) \end{bmatrix}. \end{aligned} \tag{A.3}$$

Similarly, the reverse transformation is given by

$$\begin{aligned} x_{s,dq} &= T_{dq}^{-1} x_{s,DQ} + T_{\delta^{-1}} \delta, \\ T_{dq}^{-1} &= \begin{bmatrix} cos(\delta_i) & sin(\delta_i) \\ -sin(\delta_i) & cos(\delta_i) \end{bmatrix}, \\ T_{\delta^{-1}} &= \begin{bmatrix} -x_{s,D} sin(\delta_i) + x_{s,Q} cos(\delta_i) \\ -x_{s,D} cos(\delta_i) - x_{s,Q} sin(\delta_i) \end{bmatrix}. \end{aligned} \tag{A.4}$$

A.1.1 Power Controller

Instantaneous active and reactive power components p and q are calculated from output voltage and current ($v_{o,dq}$ and $i_{o,dq}$) of inverter by

$$p = v_{o,d} i_{o,d} + v_{o,q} i_{o,q}, \tag{A.5a}$$

$$q = v_{o,d} i_{o,q} - v_{o,q} i_{o,d}. \tag{A.5b}$$

Instantaneous power components are passed through low-pass filters with a cut-off frequency ω_c to obtain their corresponding active and reactive powers P and Q (illustrated in the Laplace form):

$$P = \frac{\omega_c}{s + \omega_c} p, \tag{A.6a}$$

$$Q = \frac{\omega_c}{s + \omega_c} q. \tag{A.6b}$$

Active and reactive power sharing among inverters are obtained from the IPS scheme. System frequency ω is achieved from droop gain m_p and diffusive term Ω, and corresponding angle is calculated from an integral over frequency. In the IPS model, the diffusive term for all inverters must converge to the same value via connected LCs. For this purpose, the diffusive term value for all inverters is assumed to be equal ($\Omega = \Omega_i = \Omega_j$). Furthermore, angle of inverter voltage, θ, changes in the response to active power flow with gain of droop value m_p,

$$\omega = \omega_0 - m_p(P - P_e(\theta)) + k\Omega, \tag{A.7a}$$

$$\dot{\Omega} = -(\omega - \omega_0), \tag{A.7b}$$

$$\dot{\theta} = \omega, \tag{A.7c}$$

$$\theta = \omega_0 - \int m_p P dt. \tag{A.7d}$$

To share reactive power, Q, among multiple distributed generators, voltage magnitude $v^*_{o,d}$ is maintained via voltage droop n_q and a diffusive term e as (A.8a)

$$v^*_{o,d} = V_{0,d} - n_q(Q - Q_e(\theta)) + \kappa e, \tag{A.8a}$$

$$\dot{e} = -\beta(V_{0,d} - v_{o,d}), \tag{A.8b}$$

$$S_v = \int (V_{0,d} - v_{o,d}))dt. \tag{A.8c}$$

where S_v is a slack variable to represent an integral over voltage magnitude. As discussed before, to establish the complete model on a common reference frame, the reference of each inverter is considered as the common frame. We define a difference between an individual inverter reference frame and the common reference frame, $\Delta\theta_{com}$, by

$$\Delta\theta_{com} = \int (\Delta\omega - \Delta\omega_{com})dt. \tag{A.9}$$

Based on (A.7a and A.8a), rhe power controller model for an inverter is written as

$$\begin{bmatrix} \Delta\dot{\theta} \\ \Delta\dot{P} \\ \Delta\dot{Q} \\ \Delta\dot{S}_v \end{bmatrix} = A^{(p)} \begin{bmatrix} \Delta\theta \\ \Delta P \\ \Delta Q \\ \Delta S_v \end{bmatrix} + B^{(p)} \begin{bmatrix} \Delta i_{l,dq} \\ \Delta v_{o,dq} \\ \Delta i_{o,dq} \end{bmatrix} + B^{(p)}_{\omega_{com}} \Delta\omega_{com}$$

$$\begin{bmatrix} \Delta\omega \\ \Delta v^*_{o,dq} \end{bmatrix} = \begin{bmatrix} C^{(p)}_{\delta} \\ C^{(p)}_{PQ} \end{bmatrix} \begin{bmatrix} \Delta\theta \\ \Delta P \\ \Delta Q \\ \Delta S_v \end{bmatrix}, \tag{A.10}$$

$$A^{(p)} = \begin{bmatrix} k & -m_p & 0 & 0 \\ 0 & -\omega_c & 0 & 0 \\ 0 & 0 & -\omega_c & 0 \\ 0 & 0 & 0 & 0 \end{bmatrix}, \tag{A.11a}$$

$$B^{(p)} = \begin{bmatrix} 0 & 0 & 0 & 0 & 0 & 0 \\ 0 & 0 & \omega_c I_{o,d} & -\omega_c I_{o,q} & \omega_c V_{o,d} & \omega_c V_{o,q} \\ 0 & 0 & \omega_c I_{o,q} & -\omega_c I_{o,d} & \omega_c V_{o,q} & \omega_c V_{o,d} \\ 0 & 0 & 1 & 0 & 0 & 0 \end{bmatrix}, \tag{A.11b}$$

$$C_{\delta}^{(p)} = \begin{bmatrix} 0 & -m_p & 0 & 0 \end{bmatrix}, \tag{A.11c}$$

$$C_{PQ}^{(p)} = \begin{bmatrix} 0 & 0 & -n_q & -\kappa\beta \\ 0 & 0 & 0 & 0 \end{bmatrix}, \tag{A.11d}$$

$$B_{\omega_{com}}^{(p)} = \begin{bmatrix} -1 & 0 & 0 & 0 \end{bmatrix}^T. \tag{A.11e}$$

A.1.2 Voltage Controller

Output voltage of inverter is achieved from output of a PI controller which controls the current magnitude $i_{l,dq}$ (as current flowing the coupling inductance)

$$\frac{d\phi_d}{dt} = v_{o,d}^* - v_{o,d}, \tag{A.12a}$$

$$\frac{d\phi_q}{dt} = v_{o,q}^* - v_{o,q}. \tag{A.12b}$$

Algebraic equations for the voltage controller are defined as

$$i_{l,d}^* = F i_{o,d} - \omega C_f v_{o,q} + K_{pv}(v_{o,d}^* - v_{o,d}) + K_{iv}\phi_d, \tag{A.13a}$$

$$i_{l,q}^* = F i_{o,q} + \omega C_f v_{o,d} + K_{pv}(v_{o,q}^* - v_{o,q}) + K_{iv}\phi_q. \tag{A.13b}$$

Reference and feedback inputs are injected to the voltage controller to calculate reference variable of current controller:

$$\Delta\dot{\phi}_{dq} = [0]\Delta\phi_{dq} + B_{v_{o,dq}}^{(v)}\Delta v_{o,dq}^* + B^{(v)} \begin{bmatrix} \Delta i_{l,dq} \\ \Delta v_{o,dq} \\ \Delta i_{o,dq} \end{bmatrix}, \tag{A.14a}$$

$$\Delta i_{l,dq}^* = C_{\phi}^{(v)}\Delta\phi_{dq} + C_{v_{o,dq}}^{(v)}\Delta v_{o,dq}^* + C^{(v)} \begin{bmatrix} \Delta i_{l,dq} \\ \Delta v_{o,dq} \\ \Delta i_{o,dq} \end{bmatrix}, \tag{A.14b}$$

where all matrices in voltage controller are defined as follow

$$B^{(v)}_{v_{o,dq}} = \begin{bmatrix} 1 & 0 \\ 0 & 1 \end{bmatrix}, \tag{A.15a}$$

$$B^{(v)} = \begin{bmatrix} 0 & 0 & -1 & 0 & 0 & 0 \\ 0 & 0 & 0 & -1 & 0 & 0 \end{bmatrix}, \tag{A.15b}$$

$$C^{(v)}_{\phi} = \begin{bmatrix} K_{iv} & 0 \\ 0 & K_{iv} \end{bmatrix}, \tag{A.15c}$$

$$C^{(v)}_{v_{o,dq}} = \begin{bmatrix} K_{pv} & 0 \\ 0 & K_{pv} \end{bmatrix}, \tag{A.15d}$$

$$C^{(v)} = \begin{bmatrix} 0 & 0 & -K_{pv} & -\omega C_f & F & 0 \\ 0 & 0 & \omega C_f & -K_{pv} & 0 & F \end{bmatrix}. \tag{A.15e}$$

A.1.3 Current Controller

In order to calculate the reference voltage of inverter, we define state variables γ_{dq} as follow

$$\frac{d\gamma_d}{dt} = i^*_{l,d} - i_{l,d}, \tag{A.16a}$$

$$\frac{d\gamma_q}{dt} = i^*_{l,q} - i_{l,q}. \tag{A.16b}$$

Virtual impedance, $r_v + j\omega L_v$, is added to the current controller to regulate output voltage. Algebraic equation for the current controller is defined as follow

$$v^*_{i,d} = -r_v i_{l,d} + \omega L_v i_{l,q} - \omega L_f i_{l,q} + K_{pc}(i^*_{l,d} - i_{l,d}) + K_{ic}\gamma_d, \tag{A.17a}$$

$$v^*_{i,q} = -r_v i_{l,q} - \omega L_v i_{l,d} + \omega L_f i_{l,d} + K_{pc}(i^*_{l,q} - v_{o,q}) + K_{ic}\gamma_q. \tag{A.17b}$$

Small-signal state-space form of current controller is given by

$$\Delta\dot{\gamma}_{dq} = [0]\Delta\gamma_{dq} + B^{(c)}_{i_{l,dq}}\Delta i^*_{l,dq} + B^{(c)} \begin{bmatrix} \Delta i_{l,dq} \\ \Delta v_{o,dq} \\ \Delta i_{o,dq} \end{bmatrix}, \tag{A.18a}$$

$$\Delta v^*_{i,dq} = C^{(c)}_{\gamma}\Delta\gamma_{dq} + C^{(c)}_{i_{l,dq}}\Delta i^*_{l,dq} + C^{(c)} \begin{bmatrix} \Delta i_{l,dq} \\ \Delta v_{o,dq} \\ \Delta i_{o,dq} \end{bmatrix}, \tag{A.18b}$$

where all matrices in the current controller are defined as follow

$$B^{(c)}_{i_{l,dq}} = \begin{bmatrix} 1 & 0 \\ 0 & 1 \end{bmatrix}, \tag{A.19a}$$

$$B^{(c)} = \begin{bmatrix} -1 & 0 & 0 & 0 & 0 & 0 \\ 0 & -1 & 0 & 0 & 0 & 0 \end{bmatrix}, \tag{A.19b}$$

$$C^{(c)}_{\gamma} = \begin{bmatrix} K_{ic} & 0 \\ 0 & K_{ic} \end{bmatrix}, \tag{A.19c}$$

$$C^{(c)}_{i_{l,dq}} = \begin{bmatrix} K_{pc} & 0 \\ 0 & K_{pc} \end{bmatrix}, \tag{A.19d}$$

$$C^{(c)} = \begin{bmatrix} -r_v - K_{pc} & \omega(L_v - L_f) & 0 & 0 & 0 & 0 \\ \omega(L_f - L_v) & -r_v - K_{pc} & 0 & 0 & 0 & 0 \end{bmatrix}. \tag{A.19e}$$

A.1.4 Output LCL Filter and Coupling Inductance

Small-signal model of LCL filter and coupling inductance is represented by

$$\begin{aligned}
\frac{di_{l,d}}{dt} &= \frac{-r_f}{L_f} i_{l,d} + \omega i_{l,q} + \frac{1}{L_f}(v_{i,d} - v_{o,d}),\\
\frac{di_{l,q}}{dt} &= \frac{-r_f}{L_f} i_{l,q} - \omega i_{l,d} + \frac{1}{L_f}(v_{i,q} - v_{o,q}),\\
\frac{dv_{o,d}}{dt} &= \omega v_{o,q} + \frac{1}{C_f}(i_{l,d} - i_{l,d}),\\
\frac{dv_{o,q}}{dt} &= -\omega v_{o,d} + \frac{1}{C_f}(i_{l,q} - i_{l,q}),\\
\frac{di_{o,d}}{dt} &= \frac{-r_c}{L_c} i_{o,d} + \omega i_{o,q} + \frac{1}{L_c}(v_{o,d} - v_{b,d}),\\
\frac{di_{o,q}}{dt} &= \frac{-r_c}{L_c} i_{o,q} - \omega i_{o,d} + \frac{1}{L_c}(v_{o,q} - v_{b,q}).
\end{aligned} \tag{A.20}$$

The following equations represent the state-space form of LC filter and coupling inductance.

$$\begin{bmatrix} \Delta\dot{i}_{l,dq} \\ \Delta\dot{v}_{o,dq} \\ \Delta\dot{i}_{o,dq} \end{bmatrix} = A^{(lcl)} \begin{bmatrix} \Delta i_{l,dq} \\ \Delta v_{o,dq} \\ \Delta i_{o,dq} \end{bmatrix} + B^{(lcl)}_{v_{i,dq}} \Delta v_{i,dq} + B^{(lcl)}_{v_{b,dq}} \Delta v_{b,dq} + B^{(lcl)}_{\omega} \Delta\omega, \tag{A.21a}$$

$$A^{(lcl)} = \begin{bmatrix} \frac{-r_f}{L_f} & -\omega & -\frac{1}{L_f} & 0 & 0 & 0 \\ -\omega & \frac{-r_f}{L_f} & 0 & -\frac{1}{L_f} & 0 & 0 \\ \frac{1}{C_f} & 0 & 0 & \omega & -\frac{1}{C_f} & 0 \\ 0 & \frac{1}{C_f} & -\omega & 0 & 0 & -\frac{1}{C_f} \\ 0 & 0 & \frac{1}{L_c} & 0 & \frac{-r_{L_c}}{L_c} & \omega \\ 0 & 0 & 0 & \frac{1}{L_c} & -\omega & \frac{-r_{L_c}}{L_c} \end{bmatrix}, \tag{A.21b}$$

$$B^{(lcl)}_{v_{i,dq}} = B^{(lcl)}_{v_{b,dq}} = \begin{bmatrix} \frac{1}{L_f} & 0 & 0 & 0 & 0 & 0 \\ 0 & \frac{1}{L_f} & 0 & 0 & 0 & 0 \end{bmatrix}^T, \tag{A.21c}$$

$$B^{(lcl)}_{\omega} = \begin{bmatrix} I_{l,q} & -I_{l,d} & V_{o,q} & -V_{o,d} & I_{o,q} & -I_{l,d} \end{bmatrix}^T. \tag{A.21d}$$

A complete small-signal model of an inverter can be achieved by combining state-space models of power controller, voltage and current controllers, and output LCL filter. There are totally 14 states, and 3 inputs, two outputs in each inverter model (except inverter which its renference is common reference frame) [58]:

$$\begin{aligned} \Delta\dot{x}^{(inv_i)} &= A^{(inv_i)}\Delta x^{(inv_i)} + B^{(inv_i)}\Delta v^{(inv_i)}_{b,DQ} + B^{(inv_i)}_{\omega_{com}}\Delta\omega_{com} \\ \begin{bmatrix} \Delta\omega^{(inv_i)} \\ \Delta i^{(inv_i)}_{o,DQ} \end{bmatrix} &= \begin{bmatrix} C^{(inv_i)}_{\omega} \\ C^{(inv_i)}_{i_{o,DQ}} \end{bmatrix} \Delta x^{(inv_i)}, \end{aligned} \tag{A.22}$$

and state variables and matrices are defined as follow

$$\begin{aligned} \Delta x^{(inv_i)} = [&\Delta\theta^{(inv_i)}, \Delta P^{(inv_i)}, \Delta Q^{(inv_i)}, \Delta S^{(inv_i)}_{v}, \Delta\phi^{(inv_i)}_{dq}, \\ &\Delta\gamma^{(inv_i)}_{dq}, \Delta i^{(inv_i)}_{l,dq}, \Delta v^{(inv_i)}_{o,dq}, \Delta i^{(inv_i)}_{o,dq}], \end{aligned} \tag{A.23a}$$

$$A^{(inv_i)} = \begin{bmatrix} A^{(inv_i)}_{(1)} & A^{(inv_i)}_{(2)} & A^{(inv_i)}_{(3)} & A^{(inv_i)}_{(4)} \end{bmatrix}, \tag{A.23b}$$

$$A^{(inv_i)}_{(1)} = \begin{bmatrix} A^{(p),(inv_i)} \\ \\ B^{(v),(inv_i)}_{v_{o,dq}} C^{(p),(inv_i)}_{PQ} \\ \\ B^{(c),(inv_i)}_{i_{l,dq}} C^{(v),(inv_i)}_{v_{o,dq}} C^{(p),(inv_i)}_{PQ} \\ \\ \begin{array}{c} B^{(lcl),(inv_i)}_{v_{i,dq}} C^{(c),(inv_i)}_{i_{l,dq}} C^{(v),(inv_i)}_{v_{o,dq}} C^{(p),(inv_i)}_{PQ} \\ +B^{(lcl),(inv_i)}_{v_{b,dq}} \begin{bmatrix} T_{\delta^{-1}} & 0 & 0 \end{bmatrix} + B^{(lcl),(inv_i)}_{\omega_{com}} C^{(p),(inv_i)}_{\delta} \end{array} \end{bmatrix}, \tag{A.23c}$$

$$A^{(inv_i)}_{(2)} = \begin{bmatrix} 0 \\ \\ 0 \\ \\ B^{(c),(inv_i)}_{i_{l,dq}} C^{(v),(inv_i)}_{\phi} \\ \\ B^{(lcl),(inv_i)}_{v_{i,dq}} C^{(c),(inv_i)}_{i_{l,dq}} C^{(v),(inv_i)}_{\phi} \end{bmatrix}, \tag{A.23c}$$

$$A^{(inv_i)}_{(3)} = \begin{bmatrix} 0 \\ 0 \\ 0 \\ B^{(lcl),(inv_i)}_{v_{i,dq}} C^{(c),(inv_i)}_{\gamma} \end{bmatrix}, \tag{A.23d}$$

$$A^{(inv_i)}_{(4)} = \begin{bmatrix} B^{(p),(inv_i)} \\ \\ B^{(v),(inv_i)} \\ \\ B^{(c),(inv_i)}_{i_{l,dq}} C^{(v),(inv_i)} + B^{(c),(inv_i)}, \\ \\ A^{(lcl),(inv_i)} + B^{(lcl),(inv_i)}_{v_{i,dq}} (C^{(c),(inv_i)}_{i_{l,dq}} C^{(v),(inv_i)} + C^{(c),(inv_i)}) \end{bmatrix}, \tag{A.23e}$$

$$B^{(inv_i)} = \begin{bmatrix} 0 \\ 0 \\ 0 \\ B^{(lcl),(inv_i)}_{v_{b,dq}} [T^{-1}_{dq}] \end{bmatrix}, \tag{A.23f}$$

$$B^{(inv_i)}_{\omega_{com}} = \begin{bmatrix} B^{(p),(inv_i)}_{\omega_{com}} \\ 0 \\ 0 \\ 0 \end{bmatrix}, \tag{A.23g}$$

$$C^{(inv_i)}_{\omega} = \begin{cases} \begin{bmatrix} C^{(p),(inv_i)}_{\delta} & 0 & 0 & 0 \end{bmatrix}, & i = 1 \\ \begin{bmatrix} 0 & 0 & 0 & 0 \end{bmatrix}, & i \neq 1 \end{cases}, \tag{A.23h}$$

$$C_{i_{o,DQ}}^{(inv_i)} = \begin{bmatrix} T_\delta & 0 & 0 & T_{dq} \end{bmatrix}. \tag{A.23k}$$

A.2 Combined Model of Voltage Source Inverters

In an islanded MG, there can be several inverter connected together via AC link called power common coupling. The combined small-signal model of all inverters is obtained by

$$\begin{aligned} \Delta\dot{x}^{(INV)} &= A^{(INV)}\Delta x^{(INV)} + B^{(INV)}\Delta v_{b,DQ} \\ \Delta i_{o,DQ} &= C^{(INV)}\Delta x^{(INV)}, \\ \Delta x^{(INV)} &= \left[\Delta x^{(inv_1)}, \Delta x^{(inv_2)}, ..., \Delta x^{(inv_{n_G})}\right], \end{aligned} \tag{A.24}$$

where the matrices are defined as follow

$$A^{(INV)} = \begin{bmatrix} A^{(inv_1)} + B_{\omega_{com}}^{(inv_1)} C_\omega^{(inv_1)} & 0 & ... & 0 \\ 0 & A^{(inv_2)} & ... & 0 \\ . & . & . & . \\ 0 & 0 & .... & A^{(inv_{n_G})} \end{bmatrix}, \tag{A.25a}$$

$$B^{(INV)} = \begin{bmatrix} B^{(inv_1)} & 0 & ... & 0 \\ 0 & B^{(inv_2)} & ... & 0 \\ . & . & . & . \\ 0 & 0 & ... & B^{(inv_{n_G})} \end{bmatrix}, \tag{A.25b}$$

$$C^{(INV)} = \begin{bmatrix} C^{(inv_1)} & 0 & ... & 0 \\ 0 & C^{(inv_2)} & ... & 0 \\ . & . & . & . \\ 0 & 0 & ... & C^{(inv_{n_G})} \end{bmatrix}, \tag{A.25c}$$

$$\Delta v_{b,DQ} = \left[\Delta v_{b,DQ}^{(inv_1)}, \Delta v_{b,DQ}^{(inv_2)}, ..., \Delta v_{b,DQ}^{(inv_{n_G})}\right]. \tag{A.25d}$$

A.3 Synchronous Generator

The typical DG which uses SG as interface are diesel generator, combined heat and power, and microturbine. The stator of SG is connected to MG directly. SG model is composed of stator and rotor windings, exciter, governor, turbine, and AVR. In particular, this formulation is useful for linearized or small-displacement formulation for operating point stability issues by neglecting stator electric transients. The electrical characteristics of the rotor have often been approximated by three lumped parameter circuits, one field winding and two damper windings (See Figure 7.3-1 in [78]). The q- and d-axis transient reactances are defined as

$$X_q' = X_q + \frac{X_{m,q}X_{k1r,q}'}{X_{k1r,q}' + X_{m,q}}, \tag{A.26a}$$

$$X_d' = X_d + \frac{X_{m,d}X_{f,d}'}{X_{f,d}' + X_{m,d}}. \tag{A.26b}$$

The q- and d-axis sub-transient reactances are achieved from (7.4-8) in [78]. It is noteworthy to say that the simplify model of SG is described as follow

$$\begin{aligned}
&\Delta\dot{x}^{(SG)} = A^{(SG)}\Delta x^{(SG)} + B^{(SG)}\Delta v_{b,DQ}\\
&\Delta i_{o,DQ} = C^{(SG)}\Delta x^{(SG)},\\
&\Delta x^{(SG)} = \left[\Delta x^{(sg_1)},\, \Delta x^{(sg_2)},\, ..., \Delta x^{(sg_{n_{SG}})}\right],
\end{aligned} \tag{A.27}$$

where the matrices are defined as follow

$$A^{(SG)} = \begin{bmatrix} A^{(sg_1)} & 0 & ... & 0 \\ 0 & A^{(sg_2)} & ... & 0 \\ . & . & . & . \\ 0 & 0 & .... & A^{(sg_{n_{SG}})} \end{bmatrix}, \tag{A.28a}$$

$$B^{(SG)} = \begin{bmatrix} B^{(sg_1)} & 0 & ... & 0 \\ 0 & B^{(sg_2)} & ... & 0 \\ . & . & . & . \\ 0 & 0 & ... & B^{(sg_{n_{SG}})} \end{bmatrix}, \tag{A.28b}$$

$$C^{(SG)} = \begin{bmatrix} C^{(sg_1)} & 0 & ... & 0 \\ 0 & C^{(sg_2)} & ... & 0 \\ . & . & . & . \\ 0 & 0 & ... & C^{(sg_{n_{SG}})} \end{bmatrix}, \tag{A.28c}$$

$$\Delta v_{b,DQ} = \left[\Delta v_{b,DQ}^{(sg_1)},\, \Delta v_{b,DQ}^{(sg_2)},\, ..., \Delta v_{b,DQ}^{(sg_{n_{SG}})}\right], \tag{A.28d}$$

$$\begin{aligned}
&\Delta\dot{x}^{(sg_i)} = A^{(sg_i)}\Delta x^{(sg_i)} + B^{(sg_i)}\begin{bmatrix}\Delta v_{b,DQ}^{(sg_i)}\\ \Delta u\end{bmatrix} + B_{\omega_{com}}^{(sg_i)}\Delta\omega_{com}\\
&\begin{bmatrix}\Delta\omega^{(sg_i)}\\ \Delta i_{o,DQ}^{(sg_i)}\end{bmatrix} = \begin{bmatrix}C_{\omega}^{(sg_i)}\\ C_{i_{o,DQ}}^{(sg_i)}\end{bmatrix}\Delta x^{(sg_i)},
\end{aligned} \tag{A.28e}$$

$$\Delta x^{(sg_i)} = [\Delta\theta^{(sg_i)},\, \Delta P^{(sg_i)},\, \Delta P_v^{(sg_i)},\, \Delta P_m^{(sg_i)},\, \Delta v_{o,dq}^{(sg_i)},\, \Delta i_{o,dq}^{sg_i)},$$

$$\Delta i^{(sg_i)}_{k1r,q},\ \Delta i^{(sg_i)}_{k2r,q},\ \Delta i^{(sg_i)}_{f,d},\ \Delta i^{(sg_i)}_{kr,d}]. \tag{A.28f}$$

These matrices are achieved as follows:

$$E = \frac{1}{\omega}\begin{bmatrix} -X_d & 0 & 0 & 0 & X_{m,d} & X_{m,d} \\ 0 & -X_q & -X_{m,q} & X_{m,q} & 0 & 0 \\ 0 & -X_{m,q} & X'_{k1r,q} & X_{m,q} & 0 & 0 \\ 0 & -X_{m,q} & X_{m,q} & X'_{k2r,q} & 0 & 0 \\ -\dfrac{X^2_{m,d}}{r'_{f,d}} & 0 & 0 & 0 & \dfrac{X_{m,d}X'_{f,d}}{r'_{f,d}} & \dfrac{X^2_{m,d}}{r'_{f,d}} \\ -X_{m,d} & 0 & 0 & 0 & X_{m,d} & X'_{kr,d} \end{bmatrix}, \tag{A.29a}$$

$$F = -\begin{bmatrix} -r_s & -X_q & -X_{m,q} & -X_{m,q} & 0 & 0 \\ X_d & -r_s & 0 & 0 & X_{m,d} & X_{m,d} \\ 0 & 0 & r'_{k1r,q} & 0 & 0 & 0 \\ 0 & 0 & 0 & r'_{k2r,q} & 0 & 0 \\ 0 & 0 & 0 & 0 & X_{m,d} & 0 \\ 0 & 0 & 0 & 0 & 0 & r'_{kr,d} \end{bmatrix}, \tag{A.29b}$$

$$Y = \begin{bmatrix} K & -\dfrac{m_p}{2H_s} & 0 & \dfrac{m_p}{2H_s} & 0 & 0 & 0 & 0 & 0 & 0 \\ 0 & \omega_c & 0 & 0 & \omega_c V_{o,d} & \omega_c V_{o,q} & 0 & 0 & 0 & 0 \\ 0 & \dfrac{1}{T_g} & -\dfrac{1}{T_g} & 0 & 0 & 0 & 0 & 0 & 0 & 0 \\ 0 & 0 & \dfrac{1}{T_t} & -\dfrac{1}{T_t} & 0 & 0 & 0 & 0 & 0 & 0 \end{bmatrix}, \tag{A.29c}$$

$$W = \begin{bmatrix} 0 & 0 & 0 & 0 & 0 & 0 & 0 & 0 & 0 & 0 \\ 0 & 0 & 0 & 0 & \omega_c I_{o,d} & -\omega_c I_{o,q} & 0 & 0 & 0 & 0 \\ 0 & 0 & 0 & 0 & 0 & 0 & 0 & 0 & 0 & 0 \\ 0 & 0 & 0 & 0 & 0 & 0 & 0 & 0 & 0 & 0 \end{bmatrix}, \tag{A.29d}$$

$$A^{(sg_i)} = \begin{bmatrix} & Y \\ 0 & [E]^{-1}F \end{bmatrix}, \qquad B^{(sg_i)} = \begin{bmatrix} & W \\ 0 & [E]^{-1} \end{bmatrix}, \tag{A.29e}$$

$$C^{(sg_i)}_{\omega} = \begin{cases} \begin{bmatrix} 0 & -m_p & 0 & ... & 0 \end{bmatrix}, & i = 1 \\ \begin{bmatrix} 0 & 0 & 0 & 0 & .... & \end{bmatrix}, & i \neq 1 \end{cases}, \tag{A.29f}$$

$$C^{(sg_i)}_{i_{o,DQ}} = \begin{bmatrix} T_\delta & 0 & 0 & T_{dq} \end{bmatrix}, \tag{A.29g}$$

$$B_{\omega_{com}}^{(sg_i)} = \begin{bmatrix} -1 \\ 0 \\ 0 \\ 0 \end{bmatrix}. \tag{A.29h}$$

A.4 MG Network

Consider n_G generator connected together via n_{Ln} line to provide n_{Ld} loads. The state equation of line current of i^{th} line connected to bus j and k is

$$\frac{di_{Ln_{(j,k)},D}}{dt} = \frac{-r_{Ln_{(j,k)}}}{L_{Ln_{(j,k)}}} i_{Ln_{(j,k)},D} + \omega i_{Ln_{(j,k)},Q} + \frac{1}{L_{Ln_{(j,k)}}}(v_{b,D}^{(inv_j)} - v_{b,D}^{(inv_k)}), \tag{A.30a}$$

$$\frac{di_{Ln_{(j,k)},Q}}{dt} = \frac{-r_{Ln_{(j,k)}}}{L_{Ln_{(j,k)}}} i_{Ln_{(j,k)},Q} - \omega i_{Ln_{(j,k)},D} + \frac{1}{L_{Ln_{(j,k)}}}(v_{b,Q}^{(inv_j)} - v_{b,Q}^{(inv_k)}). \tag{A.30b}$$

Therefore, the small-signal model of i^{th} line is given by

$$\Delta \dot{i}_{Ln_{i,DQ}} = A^{(Ln_i)} \Delta i_{Ln_{i,DQ}} + B_{v_{b,DQ}}^{(Ln_i)} \begin{bmatrix} v_{b,DQ}^{j} \\ v_{b,DQ}^{k} \end{bmatrix} + B_{\omega}^{(Ln_i)} \Delta\omega. \tag{A.31}$$

In order to design connected MG network matrices, we arrange them based on $i = \{1, 2, ..., n_{Ln}\}$ which

$$A^{(Ln_i)} = \begin{bmatrix} \frac{-r_{Ln_i}}{L_{Ln_i}} & \omega \\ -\omega & \frac{-r_{Ln_i}}{L_{Ln_i}} \end{bmatrix}, \tag{A.32a}$$

$$B_{\omega}^{(Ln_i)} = \begin{bmatrix} I_{Ln_i,Q} \\ -I_{Ln_i,D} \end{bmatrix}, \tag{A.32b}$$

$$B_{v_{b,DQ}}^{(Ln_i)} = \begin{bmatrix} ... & \frac{1}{L_{Ln_i}} & 0 & ... & \frac{-1}{L_{Ln_i}} & 0 & ... \\ ... & 0 & \frac{1}{L_{Ln_i}} & ... & 0 & \frac{-1}{L_{Ln_i}} & ... \end{bmatrix}. \tag{A.32c}$$

Small-signal model of MG network for all lines is represented by

$$\Delta\dot{i}_{Ln,DQ} = A^{(Ln)}\Delta i_{Ln,DQ} + B^{(Ln)}_{v_{b,DQ}}\Delta v_{b,DQ} + B^{(Ln)}_{\omega}\Delta\omega, \tag{A.33a}$$

$$A^{(Ln)} = \begin{bmatrix} A^{(Ln_1)} & 0 & ... & 0 \\ 0 & A^{(Ln_2)} & ... & 0 \\ . & . & . & . \\ 0 & 0 & 0 & A^{(line_{n_{line}})} \end{bmatrix}, \tag{A.33b}$$

$$B^{(Ln)}_{v_{b,DQ}} = \begin{bmatrix} B^{(Ln_1)}_{v_{b,DQ}} & B^{(Ln_2)}_{v_{b,DQ}} & ... & B^{(Ln_{n_{Ln}})}_{v_{b,DQ}} \end{bmatrix}^T, \tag{A.33c}$$

$$B^{(Ln)}_{\omega} = \begin{bmatrix} B^{(Ln_1)}_{\omega} & B^{(Ln_2)}_{\omega} & ... & B^{(Ln_{n_{line}})}_{\omega} \end{bmatrix}^T. \tag{A.33d}$$

A.5 Load Model

The Islanded MG is connected to different types of loads, i.e., passive and active loads. Passive loads are classified to resistive load (R-type), impedance load (RL-type), and constant power load (PQ-type) [76]. The active loads are only defined as inverter interfaced load. Complete small-signal model of loads is obtained by

$$\frac{di_{Ld_i,D}}{dt} = \frac{-r_{Ld_i}}{L_{Ld_i}} i_{Ld_i,D} + \omega i_{Ld_i,Q} + \frac{1}{L_{Ldi}} v^{(inv_i)}_{b,D}, \tag{A.34a}$$

$$\frac{di_{Ld_i,Q}}{dt} = \frac{-r_{Ld_i}}{L_{Ld_i}} i_{Ld_i,Q} - \omega i_{Ld_i,D} + \frac{1}{L_{Ldi}} v^{(inv_i)}_{b,Q}. \tag{A.34b}$$

Small-signal model of loads is represented by

$$\Delta\dot{i}_{Ld,DQ} = A^{(Ld)}\Delta i_{Ld,DQ} + B^{(Ld)}_{v_{b,DQ}}\Delta v_{b,DQ} + B^{(Ld)}_{\omega}\Delta\omega, \tag{A.35a}$$

$$A^{(Ld)} = \begin{bmatrix} A^{(Ld_1)} & 0 & ... & 0 \\ 0 & A^{(Ld_2)} & ... & 0 \\ . & . & . & . \\ 0 & 0 & 0 & A^{(Ld_{n_{Ld}})} \end{bmatrix}, \tag{A.35b}$$

$$B^{(Ld)}_{v_{b,DQ}} = \left[B^{(Ld_1)}_{v_{b,DQ}}, B^{(Ld_2)}_{v_{b,DQ}}, ..., B^{(Ld_{n_{Ld}})}_{v_{b,DQ}} \right]^T, \tag{A.35c}$$

$$B^{(Ld)}_{\omega} = \left[B^{(Ld_1)}_{\omega}, B^{(Ld_2)}_{\omega}, ..., B^{(Ld_{n_{Ld}})}_{\omega} \right]^T, \tag{A.35d}$$

$$A^{(Ld_i)} = \begin{bmatrix} \frac{-r_{Ld_i}}{L_{Ld_i}} & \omega \\ -\omega & \frac{-r_{Ld_i}}{L_{Ld_i}} \end{bmatrix}, \tag{A.35e}$$

$$B_{\omega}^{(Ld_i)} = \begin{bmatrix} I_{Ld_i,Q} \\ -I_{Ld_i,D} \end{bmatrix}, \tag{A.35f}$$

$$B_{v_{b,DQ}}^{(Ld_i)} = \begin{bmatrix} ... & \frac{1}{L_{Ld_i}} & 0 & ... & \frac{-1}{L_{Ld_i}} & 0 & ... \\ ... & 0 & \frac{1}{L_{Ld_i}} & ... & 0 & \frac{-1}{L_{Ld_i}} & ... \end{bmatrix}. \tag{A.35g}$$

Appendix B

Derivation of (5.7)

The approximation error is derived from averaging the descriptor of $x(t)$ from $\underline{\tau}^m$ to $\overline{\tau}^m$

$$\begin{aligned} u(t) &= \frac{1}{2\Delta\tau^m}\int_{\underline{\tau}^m}^{\overline{\tau}^m} k_\psi z(t-\psi)d\psi \\ &= g_u(z(t)), \qquad \forall \tau^m(t) \in [\underline{\tau}^m, \overline{\tau}^m] \end{aligned} \tag{B.1}$$

where

$$k_\psi = \begin{cases} 1 & \psi \leq t - \tau^m(t) \\ -1 & \psi > t - \tau^m(t) \end{cases}. \tag{B.2}$$

To obtain the above equation, the approximation error is given by

$$\begin{aligned} u(t) &= \frac{1}{\Delta\tau^m}\big[x(t-\tau^m(t)) - \frac{1}{2}\big(x(t-\overline{\tau}^m) + x(t-\underline{\tau}^m)\big)\big] \\ &= \frac{1}{2\Delta\tau^m}\big[\big(x(t-\tau^m(t)) - x(t-\overline{\tau}^m)\big) + \big(x(t-\tau^m(t)) - x(t-\underline{\tau}^m)\big)\big] \\ &= \frac{1}{2\Delta\tau^m}\big[\int_{-\overline{\tau}^m}^{-\tau^m(t)} \dot{x}(t+\psi)d\psi + \int_{-\underline{\tau}^m}^{-\tau^m(t)} \dot{x}(t+\psi)d\psi\big] \\ &= \frac{1}{2\Delta\tau^m}\big[-\int_{-\tau^m(t)}^{-\overline{\tau}^m} \dot{x}(t+\psi)d\psi + \int_{-\underline{\tau}^m}^{-\tau^m(t)} \dot{x}(t+\psi)d\psi\big] \\ &= \frac{1}{2\Delta\tau^m}\big[\int_{\tau^m(t)}^{\overline{\tau}^m} \dot{x}(t-\psi)d\psi - \int_{\underline{\tau}^m}^{\tau^m(t)} \dot{x}(t-\psi)d\psi\big] \\ &= \frac{1}{2\Delta\tau^m}\int_{\underline{\tau}^m}^{\overline{\tau}^m} k_\psi \dot{x}(t-\psi)d\psi = \frac{1}{2\Delta\tau^m}\int_{\underline{\tau}^m}^{\overline{\tau}^m} k_\psi z(t-\psi)d\psi. \end{aligned} \tag{B.3}$$

Appendix C

System Parameters

Table C.1: Line parameters in the CIGRE test case [6]

Bus from	Bus to	$r(\Omega/km)$	$X(\Omega/km)$	$B(\mu S/km)$	$l(km)$
1	2	0.173	0.423	3.83	2.8
2	3	0.173	0.423	3.83	4.4
3	4	0.173	0.423	3.83	0.61
4	5	0.173	0.423	3.83	0.56
4	6	0.173	0.423	3.83	1.54
6	7	0.173	0.423	3.83	0.24
7	9	0.173	0.423	3.83	1.67
8	9	0.173	0.423	3.83	0.32
9	10	0.173	0.423	3.83	0.77
8	12	0.173	0.423	3.83	2
11	12	0.173	0.423	3.83	2
12	13	0.173	0.423	3.83	0.2
13	5	0.173	0.423	3.83	1.5
3	8	0.173	0.423	3.83	1.3

Table C.2: Loads parameters in CIGRE test case [6]

Bus	Active Power (kW)	Power Factor
1	68	0.9
2	170	0.95
3	85	0.9
4	136	0.9
5	68	0.95
6	51	0.95
7	68	0.95
8	153	0.9
9	119	0.95
10	170	0.9
11	187	0.95
12	82	0.9
13	62	0.95

Table C.3: System parameters and DGs characteristics in CIGRE test case in Chapter 6 [91]

Parameter	**Value**
DG$_{1,3}$	
C_f	50 μF
L_f	1.35mH
m_p	4×10^{-5} rad/W.s
$\hat{m}_p$	1.5×10^{-3} rad/W
n_p	4×10^{-5} V.s/VAr
$\hat{n}_p$	15×10^{-6} V.s/VAr
DG$_{4,6}$	
C_f	50 μF
L_f	1.5mH
m_p	8×10^{-5} rad/W.s
$\hat{m}_p$	3×10^{-3} rad/W
n_p	8×10^{-5} V.s/VAr
$\hat{n}_p$	75×10^{-6} V.s/VAr

Table C.4: System parameters and DGs characteristics in CIGRE test case in Chapter 4 and 5 [76, 31]

Description	**Parameter**	**Value**
Electrical Setup		
Nominal frequency	$\omega_0/2\pi$	$60\,Hz$
Nominal voltage	V_0	$208\,V_{l-l}$
Inverter-based Generator Parameters		
Filter capacitance	C_f	$50\,\mu F$
Filter inductance	L_f	$1.35\,mH$
Switching frequency	f_{sw}	$8\,kHz$
Frequency droop gain	m_p	8×10^{-3} rad/W.s
Voltage droop gain	n_p	8×10^{-3} V.s/VAr
Proportional gain of voltage controller	K_{pv}	0.05
Integral gain of voltage controller	K_{iv}	390
Proportional gain of current controller	K_{pi}	10.5
Integral gain of current controller	K_{ii}	16000
Synchronous Generator Parameters		
Frequency droop gain	m_{p1}, m_{p_2}, m_{p3}	$4 \times 10^{-2}, 4 \times 10^{-2}, 2 \times 10^{-2}$
Voltage droop gain	n_{p1}, n_{p_2}, n_{p3}	$8 \times 10^{-2}, 8 \times 10^{-2}, 6 \times 10^{-2}$
Engine rotor inertia	H_s	$3.117\,$s
Reactance of stator	X_d, X_q	$1.014, 0.77$ p.u.
Governor and turbine time constant	T_g, T_t	$0.141, 0.141$s
Amplifier/exciter/field/sensor time constants	T_A, T_E, T_G, T_S	$1, 0.8, 1, 1$s
Amplifier/exciter/field/sensor gains	K_A, K_E, K_G, K_S	$1.1, 1, 0.03, 1$